Centrum Fizyki Teoretycznej Polskiej Akademii Nauk
Center for Theoretical Physics Polish Academy of Sciences

Mikołaj Grzędzielski

Models of accretion disks thermal oscillations in application to systems with black holes

(Modele termicznych oscylacji dysków akrecyjnych w zastosowaniu do układów z czarnymi dziurami)

PhD dissertation
written under the supervision of
prof.
Agnieszka Janiuk

Warszawa 2017

Contents

List of Figures

List of Tables

Abstract

In compact objects huge amount of mass is concentrated in a small volume. Those objects are reservoirs of the gravitational energy, which can be transformed into radiation under proper physical conditions. The stellar and galaxy evolution determines the formation of objects known as white dwarfs, neutron stars and black holes. In those objects, the surrounding matter may efficiently accrete onto the compact object.

The behaviour of that matter is driven by non-linear processes, determined by the equations of hydrodynamics, and the ouer boundary conditions. It implies different complicated patterns of the temporal variability. The inflowing plasma frequently has large angular momentum, and forms a disk around the compact object. In this case the outward transfer of angular momentum is needed to allow accretion. Disks formed around neutron starts and stelar mass black holes are very hot, emitting strong X-ray radiation. Disks around supermassive black holes in active galaxies are cooler. The dynamics of inflowing matter leads in some cases to unstable behaviour. The thermal-viscous instability, accompanied with global stabilizing mechanism like advection of heat, may result in limit-cycle oscillations. The observed oscillation patterns cover many different timescales, depending on the source parameters, predominantly on the mass.

General theory of the accretion disks was presented in 1973 by Shakura and Sunyaev. Their α disk theoryconveniently parametrizing the viscous torque still remains dominant effective large-scale theory of the accretion disks. The true underlying mechanism was identified later on as the magnetorotational instability but numerical computations of 3-D models are time consuming and cannot cover the time evolution of a geometrically thin, extended accretion disk over many viscous timescales, combined with proper description of the disk heating and cooling. The aim of this thesis is to study variable X-ray sources at different black hole mass scales and verify the existence of the radiation pressure instability, which drives the thermo-viscous oscillations in black hole accretion disks.

In this thesis I confront the α-disk model with some recent observational results (2011 IGR J17091-3624 heartbeat state and 2009-2014 HLX-1 lightcurve). I also verify the hypothesis about the stabilizing role of the Iron Opacity Bump in active galaxies. Finally I discuss physical scenarios within the framework of this model. I present the general model and apply it to some observations. The resulting lightcurve properties (period and amplitude) are confronted with accretion scenario parameters. These estimations help in determination of the black hole mass and Eddington ratio, being an alternative method in comparison to spectral modeling. It is used to determine the black hole mass of HLX-1 and can be applied to other X-ray sources with periodic thermal variability. The model is extended by the effective prescription for the wind ejection. Disk model in active galaxies is supplemented by the atomic opacities. I show that both these effects can have influence on the variability patterns and disk instability.

The thesis is organized as follows: In the Introduction the basic physical foundations of black holes and accretion physics are presented. In Chapter 2, I derive the equations for the accretion disks structure and dynamics. In Chapter 3, I focus on the example of microquasar IGR J17091-3624, and anticorrelation between the wind outflow and time variability. In Chapter 4 I present the general model of modified viscosity in accretion disks and method for estimation of masses and other parameters of the sources from the X-ray lightcurves. In Chapter 5, I apply the results from 4 to the newly discovered source HLX-1 and measure its mass and accretion rate. In Chapter 6, I propose the extension of the model from Chapter 4,

including the effects coming from the atomic processes inside the plasma, which can moderate the variability of the disk around the supermassive black holes.

Results presented in this thesis were previously published in following papers:

- February 2015, Astronomy & Astrophysics 574, 92
  Publication title: Interplay between heartbeat oscillations and wind outflow in microquasar IGR J17091-3624
  Authors: Janiuk, A.; Grzędzielski, M.; Capitanio, F.; Bianchi, S.
- December 2016, Astrophysical Journal 833, 20
  Publication title: *The Universal Heartbeat* Oscillations in Black Hole Systems Across the Mass-scale
  Authors: Wu, Q.; Czerny, B.; Grzędzielski, M.; Janiuk, A.; Gu, Wei-Min; Dong, Ai-jun; Cao, Xiao-Feng; You, Bei; Yan, Zhen; Sun, Mou-Yuan
- July 2017, Astronomy & Astrophysics 603, 110
  Publication title: *Modified viscosity in accretion disks. Application to Galactic black hole binaries, intermediate mass black holes, and active galactic nuclei*
  Authors: Grzędzielski, Mikołaj; Janiuk, Agnieszka; Czerny, Bożena; Wu, Qingwen
- August 2017, Astrophysical Journal 845, 20
  Publication title: *Local Stability and Global Instability in Iron-opaque Disks*
  Authors: Grzędzielski, Mikołaj; Janiuk, Agnieszka; Czerny, Bożena

List of abbreviations:

- AGN - Active Galactic Nuclei
- BH - Black Hole
- BHXB - Black Hole X-ray Binary
- EOS - Equation of State
- GR - General Relativity
- HLX - HyperLuminous X-ray source
- IMBH - Intermediate Mass Black Hole
- MHD - MagnetoHydroDynamics
- NS - Neutron Star
- PDE - Partial Differential Equation
- ULX - UltraLuminous X-ray Source
- WD - White Dwarf

Chapter 1

Introduction

This thesis deals with the thermal phenomena in accretion disks, especially in the case of black hole accretion. Black holes are present in the universe among all mass-scales, being the sources of strong gravitational field. The gravitational field accelerates the surrounding matter, creating the reservoirs of energy for the high energy radiation, e.g. in the X-ray band. These proceses are reflected both in time variability and spectra.

1.1. Physical foundations of the accretion disk theory

Photon-matter interactions determine the characteristic luminosity scale for an accretion scenario. The characteristic limit is called *Eddington Luminosity* and is proportional to the mass. Let's start with the analysis of the interaction between the matter and the electromagnetic radiation. The physics of this precess is described by Maxwell electrodynamics. Basic formulae from the electrodynamics are taken from Jackson, J.D., *Classical Electrodynamics*, Wiley & Sons inc., 1999 textbook, and the formulae connected with the theory of gravity, black holes and compact objects in this Chapter are taken from Frank, J., King,S., Raine D. *Accretion Power in Astrophysics.* Since the thesis is dedicated to thermal phenomena, which can be well described with only minor contribution from both Special and General relativity, I use the classical language of the vector fields, instead of full differential geometry scenario which should be applied along with relativistic effects known for higher energies. The electromagnetic phenomena are described by the Maxwell equations, describing both electric **E** and magnetic induction fields **B** evolution and their reciprocal interaction with the equations:

$$\nabla \cdot \mathbf{E} = 4\pi\rho \tag{1.1}$$

$$\nabla \cdot \mathbf{B} = 0 \tag{1.2}$$

$$\nabla \times \mathbf{B} = \mathbf{j} + \frac{1}{c}\frac{\partial \mathbf{E}}{\partial t} \tag{1.3}$$

$$\nabla \times \mathbf{E} = \frac{1}{c}\frac{\partial \mathbf{B}}{\partial t}. \tag{1.4}$$

Let's start our approach from the generalization of the Coulomb's law involving the moving particles, and regarding the finiteness of the speed of light c. We start from solution of the Maxwell equations, with the formula for the time-dependent potential from the electric charge q, taken from Jackson, J.D., *Classical Electrodynamics*, Wiley & Sons inc., 1999 textbook.

$$\Phi(\mathbf{r},t) = \int d^3r' \int dt' \frac{\rho(x',t)}{|\mathbf{r}-\mathbf{r}'|}\delta(|\mathbf{r}-\mathbf{r}'| - \mathbf{c}(\mathbf{t}-\mathbf{t}')). \tag{1.5}$$

Here δ is a Dirac delta, the functional with following property: $\int dx' f(x')\delta(x'-x) = f(x)$. Computing the electric field from the potential $\mathbf{E} = \nabla\Phi$, and taking into account the case of single particle (electric monopole):

$$\mathbf{E} = \int_{-\infty}^{t} dt' \frac{q}{|\mathbf{r}-\mathbf{r}'|^2}\frac{\mathbf{r}-\mathbf{r}'}{|\mathbf{r}-\mathbf{r}'|}\delta(|\mathbf{r}-\mathbf{r}'| - \mathbf{c}(\mathbf{t}-\mathbf{t}')). \tag{1.6}$$

The field described in Eq. (1.6) for the case of particle moving with constant velocity reduces to the Coulomb law in the frame comoving with the particle, where r is the vector from the charge to the observer. Let us consider the accelerating or decelerating particle with acceleration a. Due to the finiteness of the speed of light, r refers to the expected position under the assumption of a constant velocity of the charge. Let us assume that

1. accelerating period is short and lasts Δt
2. the particle starts to accelerate with constant acceleration $\mathbf{a}$ and starts to accelerate at $t = 0$
3. $|\mathbf{r}| = r$
4. time t after the beginning of acceleration is equal to $t = R/c$

Direction of the acceleration follows the shape of field lines, being straight in the frame of particle. In Eq. (1.6) $\mathbf{E} = \frac{q}{4\pi\epsilon_0 r^2}\frac{\mathbf{r}}{r}$, refers to 'old' position of the particle. For $|\mathbf{r}| = R - c\Delta t$ the field refers to 'new' position of the charge. In the zone $R - c\delta T < |\mathbf{r}| < R$ the transversal component of the electric field (E_t) appears. This component is given by the radial one (1.6) and the change of apparent position of charge divided by the width of this 'apparent acceleration' zone. Thus:

$$E_t = E_r \times a\Delta t \frac{R}{c}\sin\alpha \times \frac{1}{c\Delta t} = E_r \frac{aRsin\alpha}{c^2}. \tag{1.7}$$

Combining Eq. (1.6) with Eq. (1.7) leads to the Larmor formula for transverse component of the electric field of the accelerating charged particle

$$E_t = \frac{qa\sin\theta}{c^2 r}. \tag{1.8}$$

Since $E_t \approx 1/r$ and $E_r \approx 1/r^2$ the transverse component will be responsible for the long-distance radiation of energy. The particle remains under the influence of incident EM radiation

$$E_i = E_0 \sin\Omega t. \tag{1.9}$$

Thus the particle acceleration $a = \frac{qE_i}{m} = \frac{qE_0\cos\Omega t}{m}$. Thomson cross section is defined as a rate between the total radiated power and incident flux of energy. The total radiated power can be obtained from the Larmor formula ($\sigma = \frac{P_{\text{rad}}}{I}$), integrating over the sphere with radius r.

$$P_{\text{rad}} = \int\int d\phi d\theta \sin\theta r^2 \frac{1}{8\pi} c E_t^2(r,\phi,\theta) = \frac{1}{8\pi}E_i^2 \frac{8\pi}{3}\frac{q^4}{m^2c^4}. \tag{1.10}$$

The incident flux is the field energy density times c

$$I = \frac{1}{8\pi} c E_0^2. \tag{1.11}$$

Thus

$$\sigma = \frac{8\pi}{3}\frac{q^4}{m^2c^4} = 6.6 \times 10^{-29} m^2 \times (m/m_e)^{-2} \times (q/e)^4, \tag{1.12}$$

where $m_e = 9.11 \times 10^{-28}$g is electron mass and e is the elementary charge.

1.1.1. The Eddington limit

The physical constants, like gravitational constant G, light velocity c or proton mass m$_p$, giving the strength of fundamental interactions are reflected in the limiting values of the luminosity of astrophysical sources. The combination of gravity and light-matter interaction results in the universal relationship between central object mass and a maximum value of the luminosity for a stable source of radiation. This characteristic luminosity is called Eddington luminosity ($L_{\rm Edd}$). The introduction of that quantity can be found in Frank, J., King,S., Raine D. *Accretion Power in Astrophysics* textbook and is presented in below. We assume that matter consists of protons and electrons. The electrons scatter the radiation several million times more effectively than the protons (Eq. (1.12)). On the other hand, the proton mass is 3 orders of magnitude larger than electron mass, so the protons are more strongly attracted by the central mass. Let us consider the central massive object with mass M, at the distance d, emitting the radiation with luminosity L. The central massive object acts on protons with attractive force:

$$F_{\rm g} = \frac{GMm_p}{d^2}. \tag{1.13}$$

The radiation acts on the pair with repulsive force:

$$F_{\rm rad} = \frac{L}{4\pi d^2}\frac{1}{c}\sigma. \tag{1.14}$$

From Eqs. (1.13) and (1.14) the maximum value of L for a given value of M can be determined. This luminosity is called Eddington Luminosity ($L_{\rm Edd}$):

$$L_{\rm Edd} = \frac{4\pi GMm_pc}{\sigma} = 1.27 \times 10^{38} {\rm ergs}^{-1} \frac{M}{M_\odot}. \tag{1.15}$$

Since the Eddington luminosity scales with the mass, the broad universality of the processes connected with accretion of matter onto a massive object can be expected. It will be discussed more generally in the Chapter 4 for the case of accretion disk model described in Chapter 2. Especially in case of black holes, all of them are parameterized only by their mass and spin (*Price's theorem*, see e.g. *Accretion power in Astrophysics*).

1.1.2. The accretion efficiency and dimensionless accretion rate

Accretion is a process of gradual setlement of the surrounding material onto the central body. During the process of accretion, part of the gravitational potential energy of inflowing matter is converted into radiation energy. The radiation usually covers some parts of the electromagnetic spectrum, although in special cases the energy can be released via the particle flux, known as a wind or jet. The accretion efficiency η is the rate of emitted luminosity (L) to the total mass-energy flux consumed by the central object per unit of time ($\dot{M}$): .

$$\eta = \frac{L}{\dot{M}c^2}. \tag{1.16}$$

For a given accretion scenario η is a constant value. The scenario is defined predominantly by boundary condition. Let us assume the matter falling down radially onto a compact object with radius $R_{\rm star}$. Kinetic energy of the particle is dissipated when the particle hits the stellar surface. For this scenario, the accretion efficiency is equal to:

$$\eta = \frac{GM_{\rm star}m/R_{\rm star}}{mc^2} = \frac{R_{\rm Schw}}{2R_{\rm star}}, \tag{1.17}$$

where Schwarzschild radii $R_{\rm Schw}$ is defined as follows, depening the black hole mass and physical constants G and c:

$$R_{\rm Schw} = \frac{2GM}{c^2}. \tag{1.18}$$

In case of a known accretion efficiency, the dimensionless accretion rate $\dot{m}$ can be defined, with the use of the Eddington luminosity defined in Eq. (1.15):

$$\dot{m} = \frac{\dot{M}c^2}{\eta L_{Edd}}. \tag{1.19}$$

1.1.3. Accretion in comparison to other powerful phenomena in high energy astrophysics

For most of the accretion scenarios $\dot{m} < 1$ since this scenario likely satisfy the stability criterion. However, we have to keep in mind that the condition was derived under the assumption of spherical symmetry. For $\dot{m} = 1$ and typical efficiency $\eta = 1/16$ (in case of the non-rotating black hole), the characteristic timescale governing the evolution of the central object is the Salpeter timescale $t = \frac{M}{\dot{M}} = 2.8 \times 10^7$yrs, which is orders of magnitude longer than characteristic timescales in unstable accretion disks.

In rapidly evolving sources, like Gamma Ray Bursts, dimensionless accretion rate $\dot{m}$ can be even orders of magnitude larger than 1. Gamma Ray Bursts are short events of rapid and transient emission of the γ radiation. They are extremely powerful phenomena with luminosity up to 10^{54} erg s^{-1} (Abdo et al., 2009). Short bursts are coming from the neutron stars coalescence (Eichler et al., 1989). Recent detection of a short gamma ray burst and a gravitational wave from the same source confirmed this hypothesis (LIGO Scientific collaboration , 2017) . For long bursts, the explanation is hypernova model (collapsar), basing on the collapse of the massive stars (Paczyński, 1998). The GRBs are more powerful than supernovae with power up to 10^{54} erg s^{-1} (Dong et al., 2016). The enormous power of the GRBs enables observing them even at the cosmological distances.

In case of stable accretion disks, their luminosity is at about $10^{36} - 10^{46}$ erg/s (see Chapter 4 of this thesis). The accretion disks are less powerful than Gamma Ray Bursts, although they are several orders of magnitude brighter than main sequence stars, (e.g. luminosity of the Sun is $L_{\odot} = 2 \times 10^{33}$). The unique combination of strong gravitational field, critical thermal equilibrium and rotation can result in long-lasting activity of accretion disks, up to millions of years, in comparison to seconds in case of GRBs. This results in great abundance of visible accretion disk sources.

1.1.4. An example - accretion onto a white dwarf and neutron star

Equation (1.17) indicates that the efficiency of accretion process increases with a decrease of the compactness of the object. The oldest known class of the compact objects are the white dwarfs, being a final stage of the evolution of main-sequence stars. White dwarfs consist of the degenerated relativistic electron gas. Subramanyan Chandrasekhar

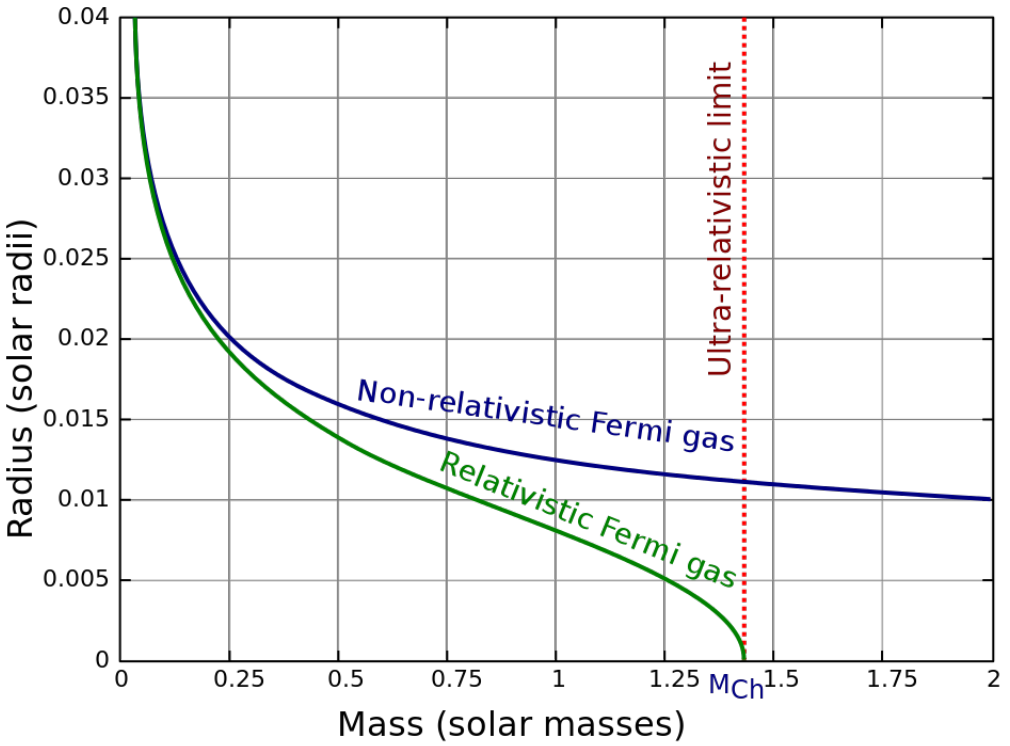

Figure 1.1: The white dwarf dimensions (After*Frank, J., King, A., Raine, D. Accretion Power in Astrophysics*).

determined the maximum mass of the white dwarf at the level of 1.44 $M_{\odot}$. This value is known as the Chandrasekhar limit. The dependence between size and mass of the white dwarfs is shown in Fig. (1.1).

The white dwarfs in compact binary systems, known as Cataclysmic Variables, attract the matter from the companion, which forms the surrounding disk. Due to the viscous processes, described more precisely in Chapter 2, the disk reaches temperature $10^4 - 10^5$ K, for which the Hydrogen ionization process appears. The transitions between neutral and ionized hydrogen complicate the matter-radiation interaction. Cooling becomes a non-monotonic function of the temperature, leading to the so called *ionization instability*. The details of the process depend on the abundance of elements. The ionization instability was the first well-reported example of the thermal instability in accretion disks (Meyer & Meyer-Hofmeister, 1981). That instability leads to the limit-cycle oscillations on timescales of month or years. The dwarf novae with their limit-cycle oscillations, being the sources radiating mostly in the optical domain, were known since 19th Century (U Geminorum).

Temperature known for the dwarf novae disks is several orders of magnitude lower than temperature of the innermost areas of Black Hole X-ray binaries accretion disks. The typical white dwarf with mass of $1M_{\odot}$, which consists of the relativistic Fermi gas, has a radius about 6×10^8cm (6000 km). Comparing to the Schwarzschild radius 3×10^5cm (3 km) it gives an efficiency $\eta = 0.001$. In comparison, the nuclear fusion reaction of burning Hydrogen to Helium, has its efficiency at the level of $\eta = 0.007$. The neutron stars are much more compact objects, which consist of extremely degenerated nuclear

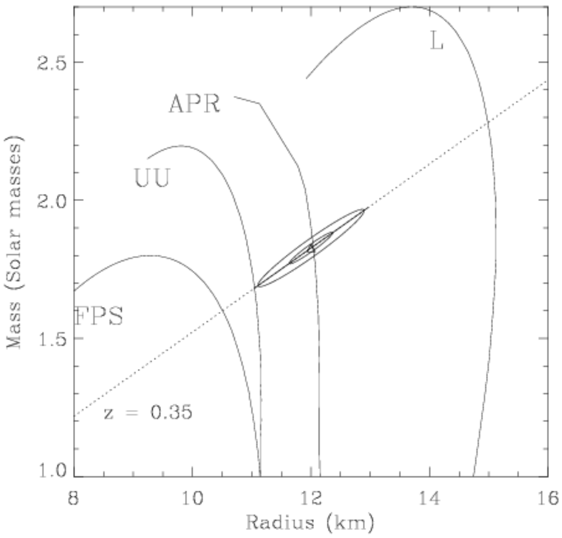

Figure 1.2: The neutron star dimensions. Different curves represent different equations of state.
(After*Frank, J., King, A., Raine, D., Accretion Power in Astrophysics*).

matter. The typical radius of the neutron star $R = 10$ km makes the accretion process very effective at the level of $\eta \approx 0.1$.

1.1.5. Black hole accretion - the General Relativistic limits

To describe the strong gravitational field around the compact stars or black holes, General Relativity is needed. General Relativity describes it in a much more detailed way. In this Subsection I present the most important GR results, being the constraints on the motion of matter. In the Newtonian gravity approach, the effective potential around a massive body M, depending on the radial position of the minor body $r(t)$, is defined in a following way:

$$V_{\rm eff} = E - 1/2(\frac{dr}{dt})^2, \tag{1.20}$$

where constant E is the total energy (both kinetic and potential). Denoting angular momentum per unit mass of a minor body as h, Eq. (1.20) gains a form:

$$V_{\rm eff} = \frac{h^2}{2r^2} - \frac{GM}{r}. \tag{1.21}$$

Schwarzschild black hole

In the case of compact object, among the length-scales comparable to Schwarzschild radii when $GM/r \approx c^2$, more detailed prescription is needed, derived exactly from the General Relativity. Moreover, the absolute time t in Eq. (1.20) is replaced by the proper time s. In particular, for a spherical body of mass M in vacuum (*Schwarzschild black hole*) it turns out that:

$$\frac{1}{c^2}(\frac{dr}{ds})^2 + V_{\rm eff}^2 = E^2. \tag{1.22}$$

The proper time depends on the radial position and total energy, and it is given by the formula:

$$\frac{dt}{ds} = (1 - \frac{2GM}{rc^2})^{-1} \tag{1.23}$$

and the effective potential is given by:

$$V^2_{S,\mathrm{eff}} = (1 - \frac{2GM}{rc^2})(1 + \frac{h^2}{c^2r^2}). \tag{1.24}$$

In Fig. (1.3) the formulae Eq.(1.21, 1.22, 1.24) are presented.The non-dimensional units $G = \frac{1}{2}$, $c = 1$ and $M = 1$ are used. One of the approximations of Schwarzschild effective potential from Eq. (1.24) is the Paczyński-Wiita potential:

$$V_{PW,\mathrm{eff}} = -\frac{GM}{r - \frac{2GM}{c^2}} + \frac{h^2}{2r^2}. \tag{1.25}$$

From the Eq. (1.24) and positiveness of the second derivative of the second potential $(\frac{d^2V_{\mathrm{eff}}}{dr^2}) > 0)$ the limitation for the stability of circular orbit around black hole at $r = 3$ can be derived. Exactly the same value is obtained from Schwarzschild solution and from Paczyński-Wiita potential. There is no innermosta stable orbit in Newtonian potential. This innermost stable orbit determines the radiative efficiency of an accretion disk.

Kerr black hole

If the black hole itself possesses angular momentum the details of this discussion, like the effective potential or Innermost Stable Circular Orbit value are somewhat altered quantitatively but not qualitatively. A rotating black hole (the Kerr solution) is characterized by a mass M and angular momentum per unit mass H. Black holes are usually expressed in terms of parameters with the dimensions of lengths: $m = \frac{GM}{c^2}$ and $a = \frac{H}{c}$. To show the universality, we can define also non-dimensional black hole spin parameter $a^* = \frac{a}{m}$, ranging from -1 to 1 for all the physical cases. For the Kerr black hole the horizon occurs at $r = m + \sqrt{m^2 - a^2}$. Here the effective potential for motion in the equatorial plane can be defined as the minimum value of the energy per unit mass for which motion is possible at each radius r, and is given by:

$$V_{\mathrm{kerr}} = \frac{A^{1/2}(B + C)^{1/2} + D}{C} \tag{1.26}$$

Where $A = r^2 - 2mr + a^2$, $B = r^2h^2$, $C = ((r^2 + a^2) + 2a^2m)r$ and $D = ahm$ respectively. Location of the innermost stable circular orbit for the Kerr black hole is given by formula (Fig. 1.5):

$$r_{\mathrm{ISCO}} = m[3 + A_2 \pm \sqrt{(3 - A_1)(3 + A_1 + 2A_2)}] \tag{1.27}$$

where $A_1 = 1 + (1 - \frac{a^2}{m^2})^{1/3}((1 + \frac{a}{m})^{1/3} + (1 - \frac{a}{m})^{1/3})$ and $A_2 = \sqrt{3\frac{a^2}{m^2} + A_1^2}$. Here in $\pm$ the $+$ sign refers to particles orbiting in the same direction as rotation of the hole, while the $-$ sign occurs for counter-rotating particles (the case of retrograde spin). This is presented in Fig. (1.5).

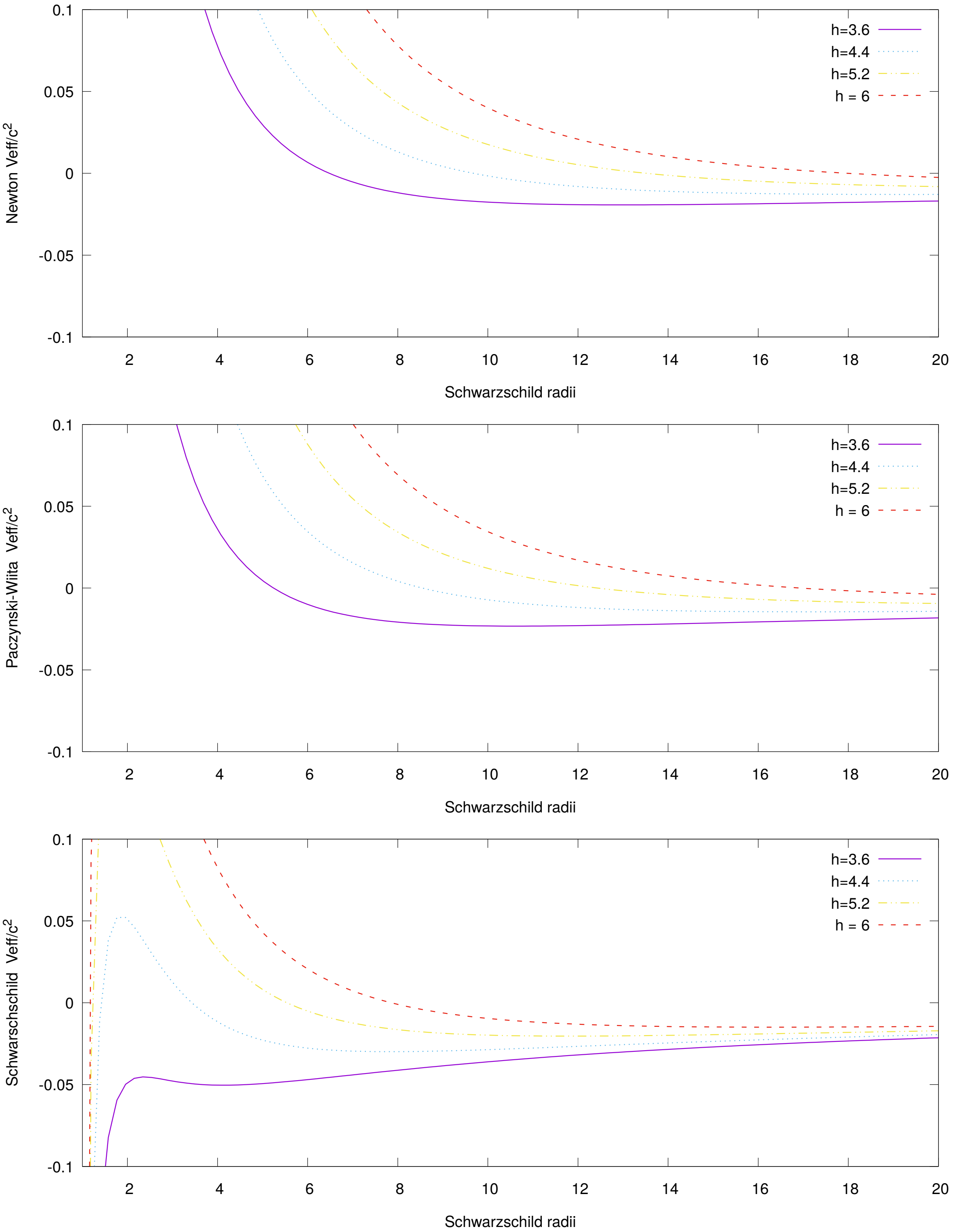

Figure 1.3: Potentials for the non-rotating black holes. The angular momentum per particle unit mass is expressed in $\frac{GM}{c}$ units.
Upper panel: Newton effective potential (Eq.1.21)
Middle panel: Schwarzschild effective potential (Eq. 1.24)
Bottom panel: Paczyński-Wiita effective potential (Eq. 1.25)

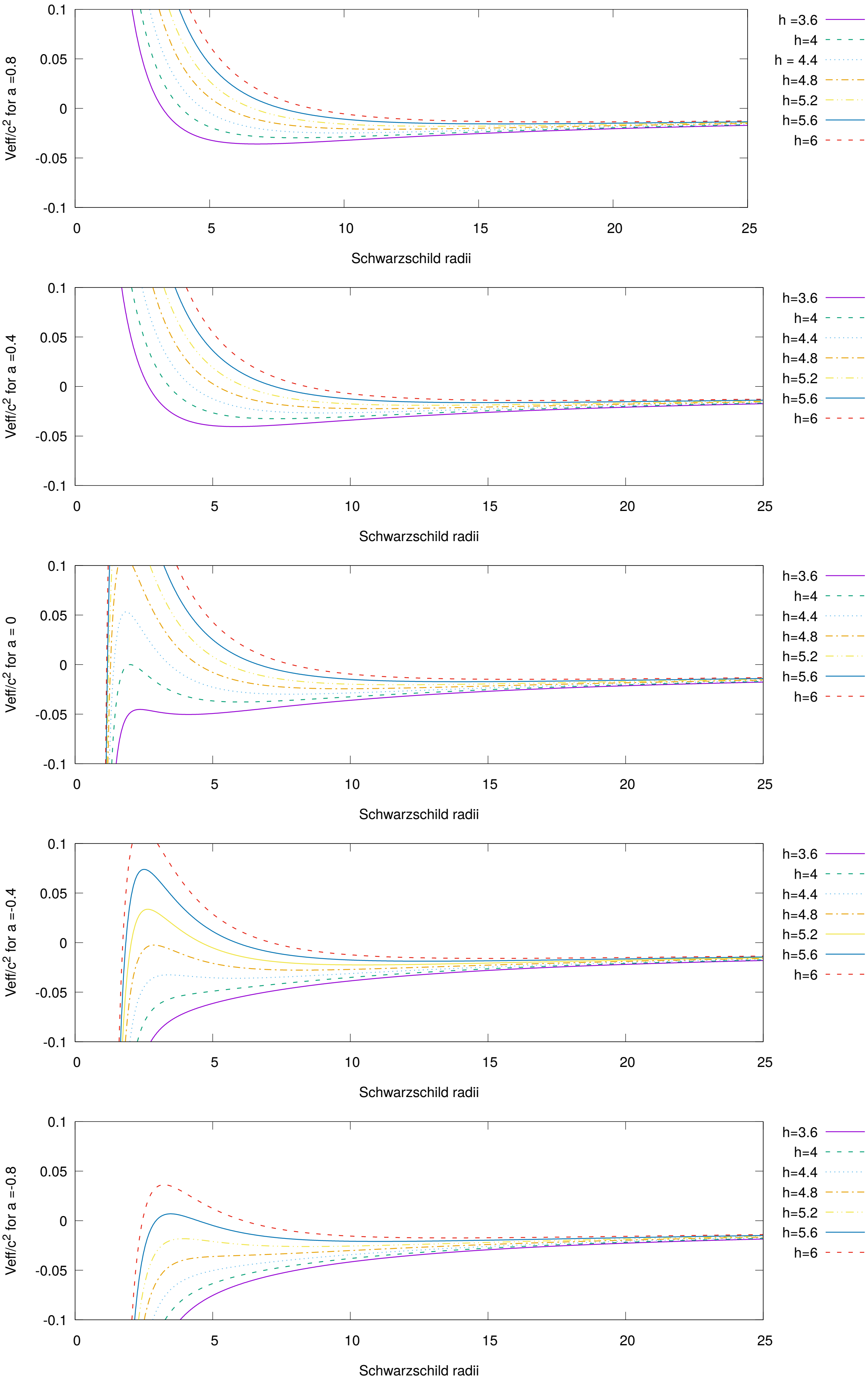

Figure 1.4: The effective potential for Kerr metric. The first and second panels are for prograde black holes, third for non-rotating, fourth and fifth for retrograde black hole. The angular momentum per particle unit mass is expressed in $\frac{GM}{c}$ units.

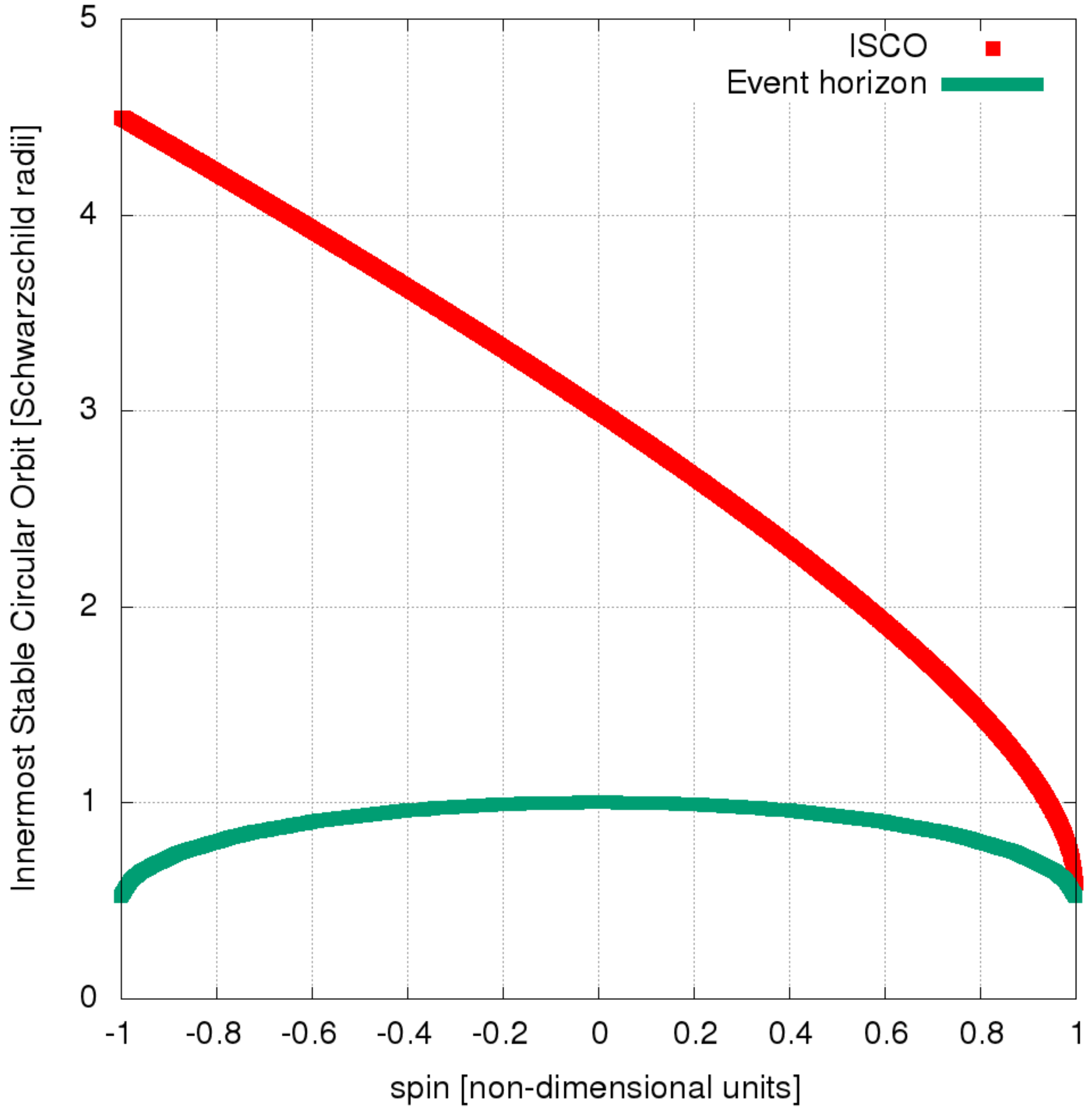

Figure 1.5: The innermost stable circular orbit in the rotating Black Hole equatorial plane in Schwarzschild radii for different spin parameter a^*.

1.2. Observational appearance of the black hole accretion disks

1.2.1. Black holes, accretion disks and X-ray sources

A black hole, being a final product of the massive star evolution, can be several times more massive than the Sun, while a black hole in the galaxy nucleus is millions or even billions times more massive than Sun. Another class of black holes are the Intermediate ones, described in this thesis in Chapter 5. Some of the black hole binaries in our Galaxy are called *microquasars*, because of the properties similar to quasars (ejection of the the collimated jets, observed in the radio band, see Mirabel et al., 1991), although they are less luminous ($L \approx 10^{37} - 10^{38}$ erg s^{-1}). According to observational data, some of these objects exhibit the periodic time variability, and their luminosity changes many times during a single observation.

1.2.2. X-ray astronomy

With the launch of the Uhuru satellite, which happened 47 years ago, the new age in the history of astronomy began. The development of space research allowed for performing observations in X-rays, which are invisible from the Earth surface because of the huge optical thickness of the Earth atmosphere, caused by the Thomson scattering (see Chapter 1). During the last decades, the systematic progress in the technologies of X-ray observations led to discoveries of many new objects. One of the most studied sources is microquasar GRS 1915+105, located some 12 kiloparsecs from the Earth. This source is ejecting very fast blobs of plasma, which move with apparently superluminal motion. The most prominent results for X-ray lightcurves of this microquasar were obtained using the X-ray satellite RXTE (Belloni et al., 2000).

The RXTE satellite [1], operating in years 1995-2012, consisting of the set of 5 proportional counters is characterized by the very good time resolution, up to 125 microseconds, which allows for precise study in the time domain, e.g. on the *Standard 1* data types. The examples of X-ray observations from the *SWIFT* satellite are presented in this thesis in Chapters 3 and 5. The *SWIFT* satellite is a new generation device, operating since 2004. *SWIFT* contains three telescopes - UVOT for the observations in optical and UV band, XRT for X-ray band and BAT for γ ray band, dedicated to the bursts. The XRT device is Wolter Type I X-ray telescope, a different construction which allows imaging in contradiction to the proportional counter arrays. In this thesis I will focus on the X-ray observations from RXTE PCA and SWIFT XRT, which will be used to present the variability patterns of the accretion disks X-ray sources.

X-ray part of the electromagnetic spectrum is the topic of our observational interest. Following the Longair, M., *High Energy Astrophysics*, Cambridge University Press, 2011 textbook, we can define the X-ray band as covering the part of electromagnetic spectrum from 10 pm (200 keV) up to 10 nm (0.2 keV), more energetic than UV radiation, but less energetic than γ radiation. X-ray radiation is the ionizing radiation, nevertheless in comparison to UV they have less complex interactions with the atoms, except for highly ionized heavy elements. Some examples of the typical BH accretion disk spectra are presented in Fig. (1.8). In contradiction to γ rays, X-rays do not lead to the creation

---

[1] $https://heasarc.gsfc.nasa.gov/docs/xte/XTE.html$

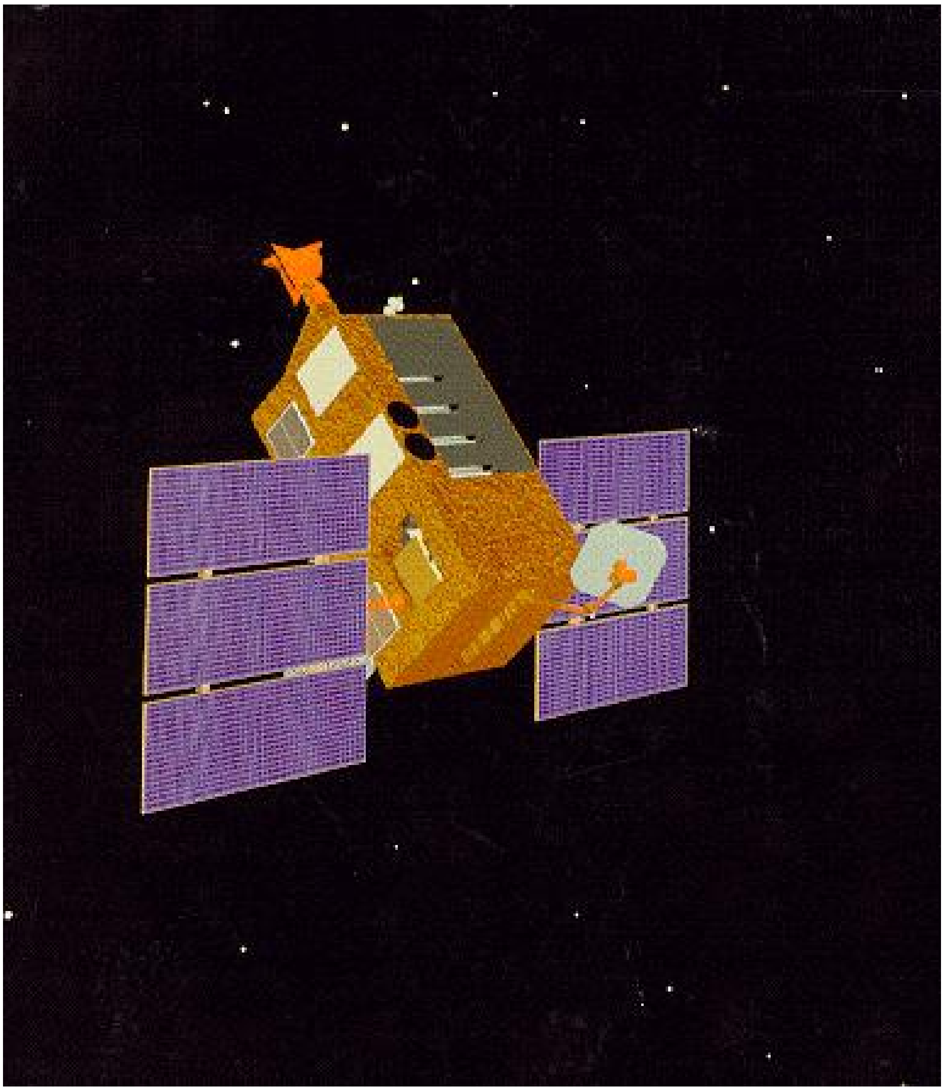

Figure 1.6: Rossi X-Ray Time Explorer - the X-ray satellite working in years 1995-2012, characterized by the very good time resolution (up to 125μs.) $(https://en.wikipedia.org/wiki/Rossi\_X-ray\_Timing\_Explorer/media/File:Rxte.jpg)$

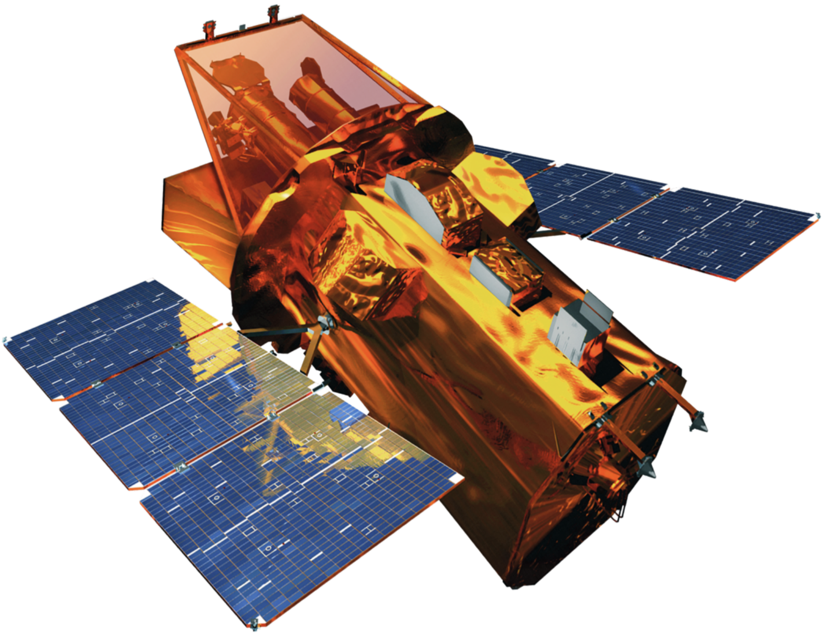

Figure 1.7: SWIFT- the X-ray satellite working since 2004 ($https : //pl.wikipedia.org/wiki/Swift\_(satelita)/media/File : Nasa\_swift\_satellite.jpg$)

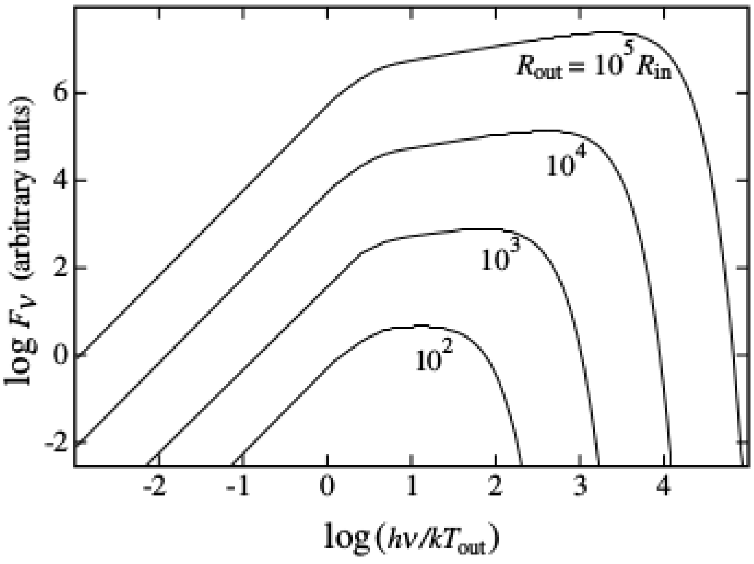

Figure 1.8: Typical spectrum of the accretion disk *J.Frank, A.King, D.Raine, Áccretion power in Astrophysics*

of elementary particles and nuclear processes. The peak temperatures of the blackbody spectra for those energies correspond to $10^6 - 10^9$K. Thus the temperatures at the order of few millions K are expected. In the standard sub-Eddington accretion disk, around the stellar-mass black hole, the temperature reaches the values on the order of $T \approx 10^6 - 10^7$K.

1.2.3. X-ray data

The sources emit flux of photons, each one with given energy $E_\nu = h\nu$. The total flux of photons coming from a given source depends on time and energy $I(E,t)$. After integration of the flux over the broad range of energy, like $0.3 - 10$ keV, the lightcurve is defined as $L_X(t) = \int_{E_{min}}^{E_{max}} dEI(E,t)$. If we set a narrow energy channel (e.g. several eV) and integrate it over the long time T (e.g. 16 seconds), we get the spectrum $I(E) = \int_0^T I(E,t)dt$. The lightcurves are used for researching the dynamics of the source [2]. The spectra provides us information about the averaged state of the sources and can be studied in many different ways. The continuum provides us the information about the temperature of sources and another ongoing processes e.g. Comptonization. This process is characteristic for presence of corona. The emission from corona is non-thermal and forms the power-law tail. The states of sources can be divided into the *Soft* and *Hard* (see e.g. Pahari et al. (2014)). In Fig. (1.11) we show the comparison of *Soft* and *Hard* states for the Cyg X-1 source. The soft states are dominated by the thermal almost black body radiation from accretion disks (up to few keV), with a tail due to non-thermal electrons, extending above 1 MeV, and hard states, dominated by Comptonized radiation from mostly thermal electrons from the corona. The spectral lines are characterised by photon energy and line intensity. The photon energy provides information about the atomic transition (like absorption by the H-like iron)[3] or its shift (redshift or blueshift) being a track of the observed motion of the matter (e.g. the accretion disk wind). The line intensity can provide us information about the absorbing or emitting matter [4].

1.2.4. Classification the X-ray binaries

X-ray binaries are the binary systems, which consist of the compact object (neutron star, black hole) and a main sequence star. Another classification divides those sources into the Low Mass X-ray Binaries and High Mass X-ray Binaries (LMXBs and HMXBs) regarding the mass of the donor star (-3000which can be less or more than several solar masses). The common type of HMXBs are the Be X-ray binaries, where donor is the Be star. An example of that object is $LSI + 61303$ (Gregory et al., 1979), which is a variable radio source.

In the LMXBs, the matter is transferred to disk via Roche lobe, in contrast to HMXBs, where the matter is transferred via stellar wind. In some Neutron Star X-ray Binaries like LMC X-4 and SMC X-1 (names come from the Large Magellanic Cloud and Small Magellanic Cloud galaxies), the inflow proceeds via Roche lobe.

---

[2] In Chapters 3 and 5 the lightcurve data are presented, Chapters 4 and 6 are devoted to the possible approximation of the lightcurves

[3] An example of the Iron line absorption is presented in Chapter 3

[4] See Chapter 3

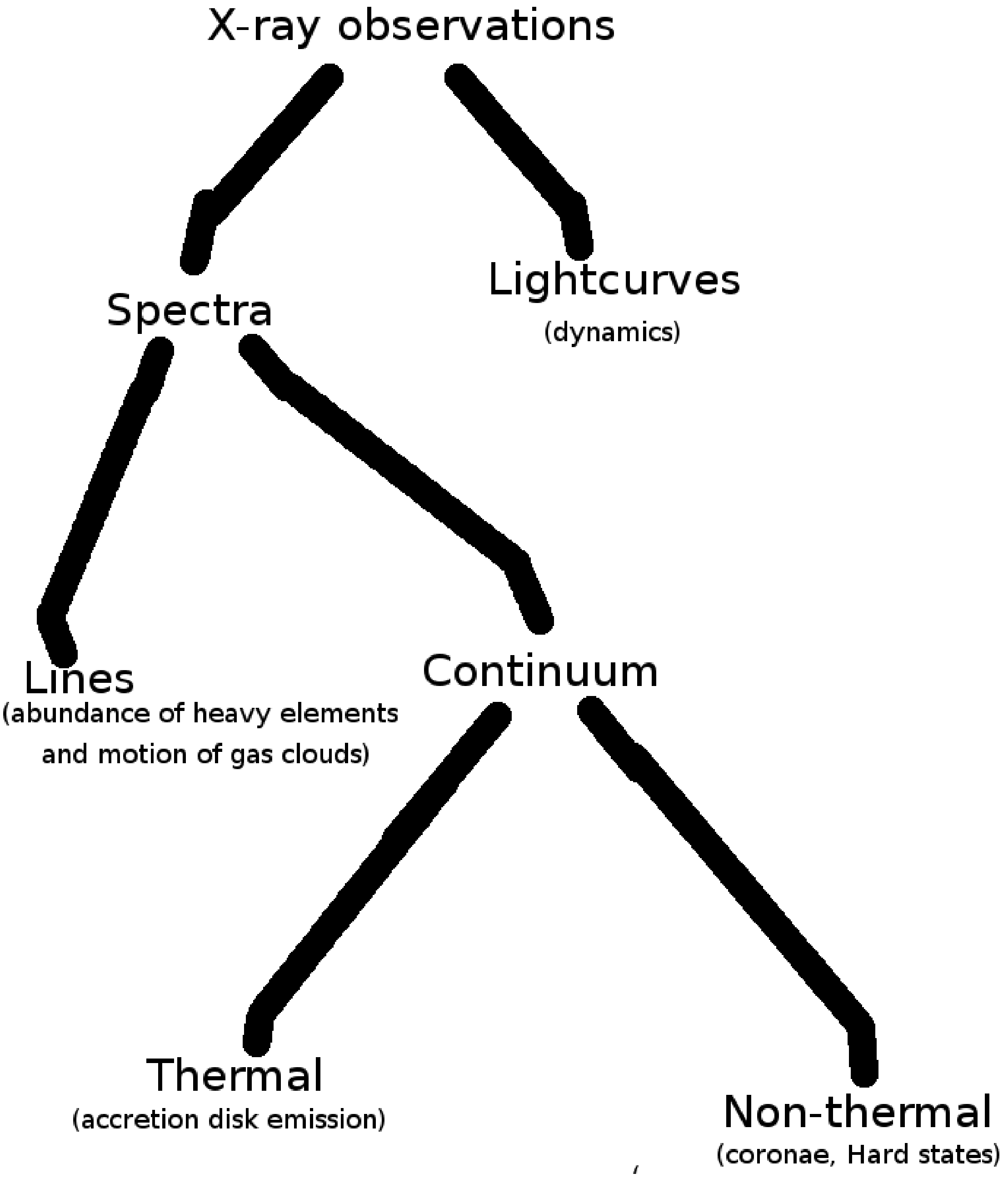

Figure 1.9: Scheme of different types of X-ray data which are being provided by the X-ray observatories

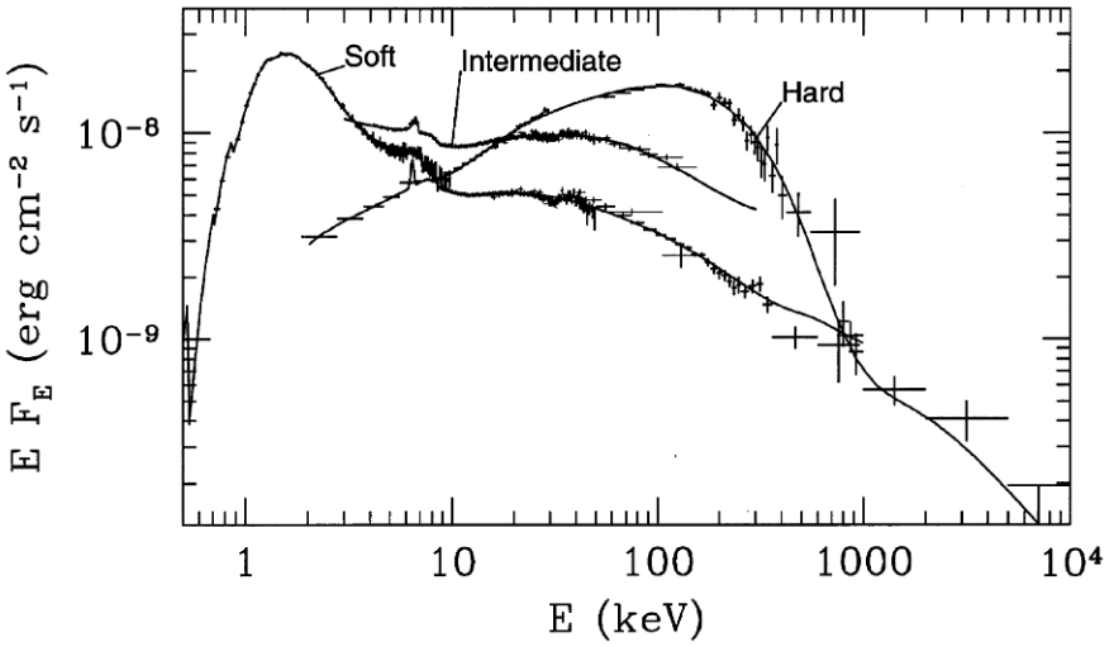

Figure 1.10: Comparison of the observed spectra in Soft, Intermediate and Hard states from the Cyg X-1 source (Gierliński et al., 1999). For more details about these observations, see (Gierliński et al., 1999).

In the Low Mass X-ray binaries the donor is normally a main sequence star with mass $M \approx M_{\odot}$. The well-known microquasar GRS 1915+105 is an example the Low Mass X-ray binary, with the rapid rotation of the central object. Furthermore, the sources can be divided also into transient (being active only temporarily, like X-Ray companion of the V404 Cygni) and persistent (being active through many years of continous observations).

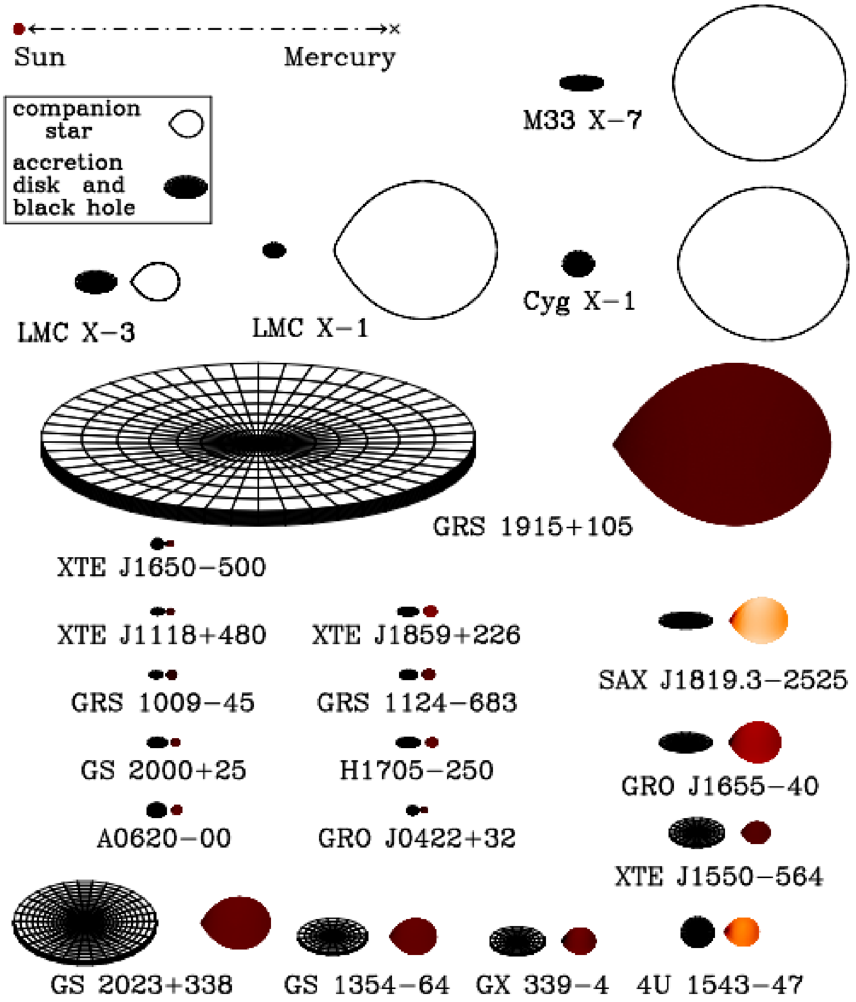

Figure 1.11: Schematic sketch to scale of 21 black hole binaries (see scale and legend in the upper-left corner). The tidally-distorted shapes of the companion stars are accurately rendered in Roche geometry. The black holes are located in the center of the disks. A disk's tilt indicates the inclination angle i for the binary, where $i = 0$ corresponds to a system that is viewed face-on; e.g. $i = 21$ for $4U1543 - 47$ (*bottom right*) and $i = 75$ for $M33X - 7$ (*top right*). The size of a system is set by the orbital period, which ranges from 33.9 days for the giant system $GRS1915 + 105$ to 0.2 days for tiny $XTEJ1118 + 480$. Three well-studied persistent systems (M33 X-7, LMC X-1 and Cyg X-1) are located in the $upper-right\ corner$. The other 16 systems are transients. (Figure courtesy of J.Orosz)

Chapter 2

Optically thick and geometrically thin accretion disks and local thermal instability

In this Chapter I present an introduction to accretion disk theory, done in classical paper of Shakura and Sunyaev (Shakura & Sunyaev, 1973). The idea of α viscosity will be presented in the next Chapter. The general form of the equations of visco-thermal disk dynamics presented in this Chapter, follows Janiuk, Czerny & Siemiginowska (2002).

2.1. Optically thick and geometrically thin accretion disks

In general the very basic parameters of accretion process include the central object mass, amount of mass falling down per unit of time and the matter angular momentum. More detailed studies can include also the BH spin. The mass scale spreads from a few solar masses (X-ray binaries), through newly discovered Intermediate Mass Black Holes (IMBH) up to supermassive black holes in the centers of Active Galactic Nuclei.

2.1.1. BH masses

The Hawking radiation process sets the lower limit for the black hole being able to survive cosmological timescales.The mass of such a black hole is about 10^{15}g. The primordial black holes (Hawking, 1971; Carr & Hawking, 1974; Page, 1976), with masses $10^{15} - 10^{26}$ g can give a possible contribution to the dark matter, however, as it has been shown by Abramowicz et al. (2009), collisions between the stars and primordial black holes, are in practice undetectable. The black holes with the stellar masses are the final products of the massive stars evolution. Their masses exceed TOV (Tolmer-Oppenheimer-Volkoff) limit (about 2 $M_{\odot}$), being the maximum possible mass for the neutron stars. The heaviest known stellar-mass black hole is GW150914 object, being a result of binary black hole merger, having mass about 62 $M_{\odot}$ (Abbott et al., 2016). Another interesting class of black holes are the Active Galactic Nuclei, with masses spread from 10^6 up to $10^{10} M_{\odot}$. On the axis of mass, between those two classes of Black Holes are IMBHs.

2.1.2. Angular momentum

One of the first well described cases of behaviour of matter was the spherical accretion problem (Bondi et al., 1952). The Bondi accretion defines the characteristic radius, depending on the sound speed c_s: $r_B = \sqrt{\frac{2GM}{c_s^2}}$, called Bondi radius. The low-angular momentum flows, which accrete almost radially and relatively weakly feel the centrifugal barier can model e.g. the weakly-active galaxy centers like the *Sagittarius A** in the Milky Way, with detectable oscillating shocks (Sukova & Janiuk, 2015). The upper limit for the angular momentum for stable solution is connected with equilibrium between the centrifugal force and gravitational attraction. It results in Keplerian disk, being a stable radial configuration, with the slow radial drift of the (Paczyński & Bisnovatyi-Kogan, 1981). This thesis is focused on disks rotating with Keplerian angular velocity.

$$\Omega = \sqrt{\frac{GM}{r^3}}. \tag{2.1}$$

In principle, the model described in Janiuk, Czerny & Siemiginowska (2002) used the angular velocity connected with Paczyński-Wiita potential circular orbits $\Omega_{\rm PW} = \Omega(1-\frac{r_{\rm Schw}}{r})^{-1}$. but during the tests no significant change in the lightcurve shape has been noticed. in Janiuk, Czerny & Siemiginowska (2002) used the : Figure (2.1) presents different types of accretion flows. The S-shaped branch of the stationary solution refers to the optically thick, geometrically thin accretion disk model, described in Chapters 3, 4 and 5. At low densities, another branch of solutions is found. It is optically thin, quasi-spherical and hot flow. The advection is dominant cooling mechanism. This work is focused on theory of Keplerian, optically thick and geometrically thin disks and its application to the observed X-ray sources.The Paczyński-Wiita potential is used since, as I showed, it well catches the properties of the extact Schwarzschild solution. In the studies of the time evolution the hydrostatic equilibrium is assumed, so I neglect sound waves, concentrating on the thermal and viscous evolution. Also the advection term is included, as in stationary solutions of Abramowicz et al. 1988 (Abramowicz et al., 1988) since it provides efficient cooling mechanism during outbursts. The heat diffusion in radial dimension is regarded as negligible and skipped, along with the short-time solutions in the form of sound waves.

2.2. The stationary model

2.2.1. Local parameters

We describe the disk in the cylindrical coordinates system (r, z, ϕ). Model used in this thesis is 1.5 dimensional, which means that in numerics we integrate over one spacial dimension (radius) and rotation of the matter is included in the value of Ω driving the viscous dissipation. The disk is described by thermodynamical quantities: temperature T, density ρ, pressure P, and thickness H. To simplify the formulae, we introduce the surface density Σ, being the bulk density integrated over the height. To measure the amount of heat produced and emitted in the disk we introduce following parameters:

- q_+ - heat production per volume unit
- q_- - cooling per volume unit
- Q_+ - heat production per surface unit (q_+ vertically integrated)

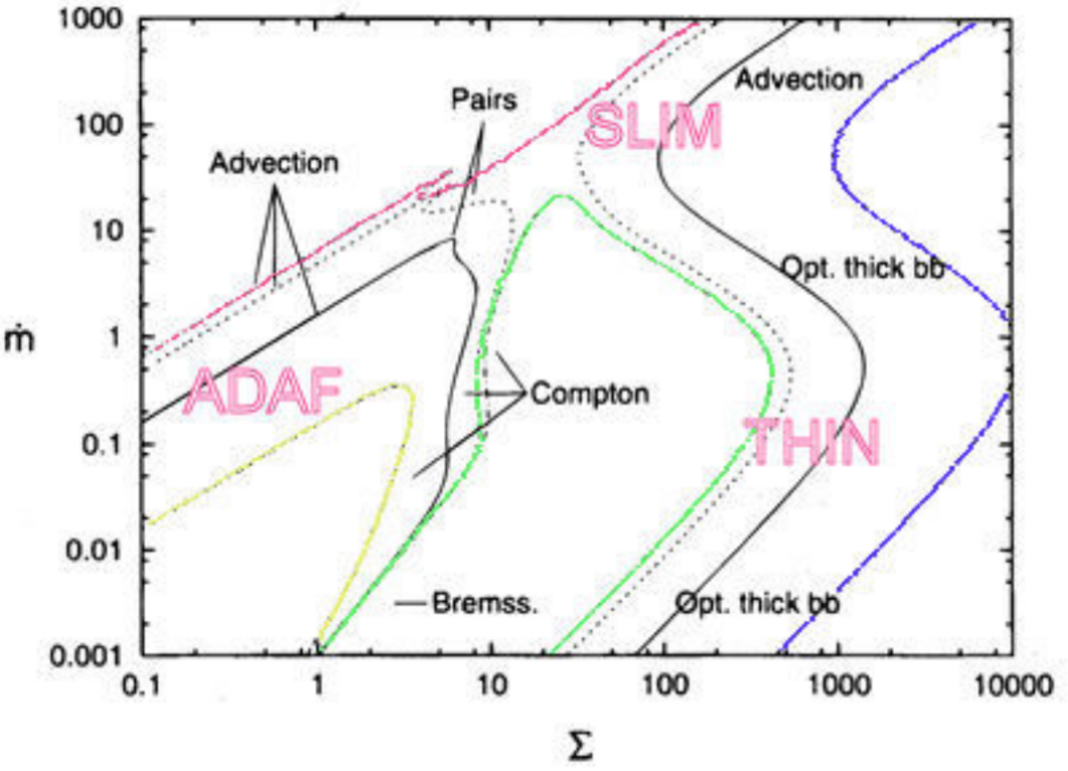

Figure 2.1: Stability curves (in terms of non-dimensional $\dot{m}$ and surface density Σ [g cm^{-2}]. Different types of accretion disks (Bjoernsson et al., 1996). The optically thick, geometrically thin disks can be found for high values of Σ and $\dot{m} < 1$. ADAF = Advection Dominated Accretion Flow.

- Q_- - heat emission per surface unit (q_- vertically integrated)

We assume that the disk consists of the gas and radiation, thus the pressure is described by the equation of state:

$$P = P_{\rm gas} + P_{\rm rad}, \tag{2.2}$$

where

$$P_{\rm gas} = a\rho T, \tag{2.3}$$

and

$$P_{\rm rad} = bT^4, \tag{2.4}$$

where $a = \frac{k_b}{m_h}$, $b = \frac{4\sigma_B}{3c}$, k_b - Boltzmann constant, m_h - proton mass, σ_b - Stefan-Boltzmann constant and c - speed of light. We perform the disk intergation in vertical direction and use the equatorial values of density and temperature, and integration constants C_1, C_2 and C_3 defined as in Janiuk, Czerny & Siemiginowska (2002):

$$C_1 = \frac{\int_0^H dz P(z)}{P_{\rm equatorial} H}, \tag{2.5}$$

$$C_2 = (\frac{\int_0^H dz \rho(z) F(z)}{\rho_{\rm equatorial} F(0) H})^{-1}, \tag{2.6}$$

$$C_3 = \frac{\int_0^H dz \rho(z) z}{\rho_{\rm equatorial} H^2}. \tag{2.7}$$

In Equation (2.6) $F(z)$ is the local energy flux for given z from the two-dimensional model. For all the computations for purpose of this thesis the values are assumed as follows: $C_1 = 1.25$, $C_2 = 6.25$ and $C_3 = 0.17$.

2.2.2. Stress tensor and heating rate

The heating of the accretion disk is driven by the viscous processes, being turbulent in origin. The more detailed prescription of the viscosity is presented in Chapter 4. These processes are described by the kinematic viscosity ν. This quantity determines the stress tensor. Its most important component, in case of viscous dissipation Keplerian disk is $T_{r\phi}$:

$$T_{r\phi} = \nu r \frac{\partial \Omega}{\partial r}. \tag{2.8}$$

We can also integrate the stress tensor vertically:

$$\tau_{r\phi} = \frac{1}{2H} \int_{-H}^{H} dz T_{r\phi}. \tag{2.9}$$

So, the bulk heating rate in the equatorial plane and the heating rate per surface unit are as follows:

$$q_+(z=0) = T_{r\phi}(z=0) r \frac{\partial \Omega}{\partial r}, \tag{2.10}$$

$$Q_+ = \tau_{r\phi} r \frac{\partial \Omega}{\partial r} H. \tag{2.11}$$

2.2.3. Inner boundary condition

Due to the existence of the Innermost Stable Circular Orbit, which results from the detailed GR computation for the black hole metric resulting in effective potentials presented in the Chapter 1, the inner boundary condition is needed to reproduce the real physics in the model, reflecting it the global disk structure via the shear stress. The torque τ_F acting on mass ring at radius r is as follows:

$$\tau_F = 2\pi r^2 \tau_{r\phi}. \tag{2.12}$$

On the other hand, the torque is responsible for the dissipation of angular momentum $\dot{M} r^2 \Omega$, where $\dot{M}$ is accretion rate, and Ω is angular velocity:

$$\dot{M} r^2 \Omega = \tau_F. \tag{2.13}$$

Combining Eq. (2.12) and Eq. (2.13) results in the formula for the locally generated stress $\bar{\tau}_{r\phi}^{local}$:

$$\bar{\tau}_{r\phi}^{local} = \frac{\dot{M}\Omega}{2\pi}. \tag{2.14}$$

The total $\tau_{r\phi}^{tot}$ consists of the local shear stress and the stress connected with the boundary condition:

$$\bar{\tau}_{r\phi}^{tot} = \bar{\tau}_{r\phi}^{local} + \bar{\tau}_{r\phi}^{boundary}. \tag{2.15}$$

Boundary term $\bar{\tau}_{r\phi}^{boundary}$ is the integration constant from the angular momentum conservation equation. Free boundary condition for the innermost radius r_{min} is given by:

$$\bar{\tau}_{r\phi}^{tot} = 0 \tag{2.16}$$

The total emitted flux is equal to shear stress times the radial gradient of angular velocity:

$$F = \bar{\tau}_{r\phi}^{tot} r \frac{\partial \Omega}{\partial r}. \tag{2.17}$$

Applying the formula for the angular velocity from Eq. (2.1) to Eq. (2.17) formula for the flux is derived:

$$F = \frac{3GM\dot{M}}{8\pi r^3}\left(1 - \sqrt{\frac{r_{\mathrm{min}}}{r}}\right). \tag{2.18}$$

In our description, we assume the hydrostatic equilibrium, which gives a constraint:

$$P_{\mathrm{eq}} = C_3 \rho \Omega^2 H^2, \tag{2.19}$$

where C_3 is a constant defined in Eq. (2.7).

2.2.4. Stationary model and time dependent model

Full computation of above model, with one special assumption that the stress tensor is proportional to the total pressure was done by Shakura & Sunyaev (1973). This thesis involves the dynamical phenomena, using the (perturbed) equilibrium solutions of the stationary model only as initial conditions for variable models described in the subsequent Chapters.

2.2.5. Heating and cooling

In stationary models, heating and cooling rates determine the structure of the disk, being equal to each other ($Q_+ = Q_-$). For all the cases (both stationary and non-stationary) the heating ratio is equal to F_{TOT} presented in Eq. (2.18). The cooling is thermal and inversely proportional to the local vertical optical thickness ($Q_- \propto T^4/\tau$), where optical thickness $\tau = \kappa\Sigma$. From Eqs. (2.9, 2.11) we can write the formula for the heating rate per unit time per surface unit:

$$Q_+ = C_1 T_{\mathrm{r}\phi} r \frac{\partial \Omega}{\partial r} H, \tag{2.20}$$

and the radiative cooling rate per unit time per surface unit is

$$Q_- = C_2 \frac{4\sigma_{\mathrm{B}} T^4}{3\kappa\Sigma}. \tag{2.21}$$

where κ is the opacity coefficient. In most cases I assume that it is dominated by the Thomson scattering, i.e equal to 0.34 $\mathrm{cm}^2\ \mathrm{g}^{-1}$ (see Eq. 1.12).

2.3. Time-dependent equations

2.3.1. Diffusion equation

The first of two equations governing the behaviour of the disk is so-called diffusion equation. It can be derived from the continuity equation in the cylindrical coordinate system:

$$\frac{\partial \Sigma}{\partial t} = \frac{1}{r}\frac{\partial (r\Sigma v_r)}{\partial t}. \tag{2.22}$$

The outflow (actually, mostly inflow) velocity depends on the local kinematic viscosity ν:

$$v_r = -\frac{3}{\Sigma} r^{-1/2} \frac{\partial}{\partial r}\left[\nu \Sigma r^{1/2}\right]. \tag{2.23}$$

Combining these two equations results in the final formula:

$$\frac{\partial \Sigma}{\partial t} = \frac{1}{r}\frac{\partial}{\partial r}[3r^{1/2}\frac{\partial}{\partial r}(r^{1/2}\nu\Sigma)]. \tag{2.24}$$

2.3.2. Energy equation

Starting from the energy conservation equation in the general form, we connect entropy S, local cooling q_- and local heating q_+:

$$T[\frac{\partial}{\partial t} + (v_r \frac{\partial}{\partial r})]S = q_+ - q_-. \tag{2.25}$$

The first necessary input for the model is to determine the thermodynamical parameters of the gas. Adopting the equation of state (gas plus radiation, Eq. 2.2), the internal energy u is as follows:

$$u = \frac{3}{2}aT + 3\frac{bT^4}{\rho}. \tag{2.26}$$

Defining $\beta = \frac{P_{\mathrm{gas}}}{P}$, leads to the following formula for the rate of change of internal energy density

$$du = \frac{P}{\rho}((12 - 10.5\beta) d\log T - (4 - 3\beta) d\log\rho). \tag{2.27}$$

Since the internal energy can change via bulk work, $dw = -\frac{p}{\rho^2} d\rho$, or heat processes TdS the energy conservations gives us:

$$TdS = du - \frac{p}{\rho^2} d\rho. \tag{2.28}$$

With the formula for the entropy:

$$TdS = \frac{P}{\rho}((12 - 10.5\beta) d\log T - (4 - 3\beta) d\log\rho), \tag{2.29}$$

the equation (2.25) gains the form:

$$(12 - 10.5\beta)[\frac{\partial \log T}{\partial t} + v_r \frac{\partial \log T}{\partial r}] + (4 - 3\beta)[\frac{\partial \log \rho}{\partial t} + v_r \frac{\partial \log \rho}{\partial r}] + = q_+ - q_-. \tag{2.30}$$

From Eq.(2.30), putting $\rho = \frac{\Sigma}{H}$, we obtain finally:

$$\frac{\partial \log T}{\partial t} + v_r \frac{\partial \log T}{\partial r} = \frac{4 - 3\beta}{12 - 10.5\beta} (\frac{\partial \log \Sigma}{\partial t} - \frac{\partial \log H}{\partial t} + v_r \frac{\partial \log \Sigma}{\partial r} - v_r \frac{\partial \log H}{\partial r}) + \frac{Q_+ - Q_-}{(12 - 10.5\beta) PH} \tag{2.31}$$

which is equivalent to Eq. (33) in Janiuk, Czerny & Siemiginowska (2002) under assumption that disk is not strongly deformed (radial derivative of H is small in comparison to derivative of Σ).

2.4. Radiation pressure instability

We can investigate the stability of the disk, focusing on both the viscous and thermal phenomena. Both the computations and observed X-ray phenomena considered in this thesis cover the timescales long in comparison to the local dynamical timescale. We advocate in this thesis that the radiation pressure instability, appearing on the thermal/viscous timescales is the most probable explanation of the limit-cycle oscillation in many accretion disks sources. The $\alpha-$prescription of Shakura & Sunyaev (1973)[1]leads to conclusion that the thermal and viscous processes described by the Eqs.(2.24, 2.31) appears in separated timescales and the thermal timescale is several orders of magnitude shorter than viscous timescale, so in thermal timescale $\Sigma \approx const.$ Thus we can write a condition for the thermal instability:

$$\frac{\partial \log Q_+}{\partial \log T} > \frac{\partial \log Q_-}{\partial \log T}. \tag{2.32}$$

In the most standard prescription, the cooling rate is proportional to the fourth power of the temperature (radiative cooling according to the Planck blackbody emission) [2], so

$$\frac{\partial \log Q_-}{\partial \log T} = 4. \tag{2.33}$$

The heating rate is much more complex, since in the Eq. (2.20), under assumption of constant Σ, $Q+ \propto T_{r\phi} P$. Shakura & Sunyaev (1973) assumed that the disk is turbulent and $T_{r\phi}$ is proportional to the total pressure $T_{r\phi} \propto P$. Thus for high enough temperatures, where the radiation pressure term in the equation of state (Eq.2.2) prevails ($P \propto T^4$), we get that $Q_+ \propto T^8$, so with Eq.(2.33), we conclude that the disk will be blown by the radiation pressure.

Disk instability under radiation pressure has been discovered by Pringle, Rees & Pacholczyk (1973). A year later Lightman & Eardley (1974) showed that radiation pressure

---

[1] which is described in more detailed way in Chapters 3 and 4

[2] For more detailed prescription of the cooling rate in accretion disks see Chapter 6

dominated disks are also viscously unstable, and both radiation and viscous stability of α-disk was studied by Shakura & Sunyaev (1976). However, the presence of disk instability does not mean that radiation pressure dominated disks does not exist. The stabilization of the disk is provided by the advection term introduced by Muchotrzeb Paczyński (1982) and Abramowicz et al. (1988) and present in Eq. (2.31) via the radial derivatives. Combined effect of the thermal radiation pressure instability and advection leads to the limit-cycle oscillations with characteristic timescales and amplitudes, which found confirmation in numerous sources [3] [4] [5].

---

[3] An example of the radiation pressure instability of IGR J17091 is presented in Chapter 3

[4] An example of the radiation pressure instability of HLX-1 intermediate-mass black hole is presented in Chapter 5

[5] For more detailed discussion about the disk viscosity see Chapter 4

Chapter 3

Microquasar IGR J17091-3624 as an example of oscillating accretion disk

In this Chapter we introduce the code GLADIS (Global Accretion Disk Instability Simulation), used also for some computations in Chapters 4, 5 and 6. Particularly in this Chapter, we apply it to explain the *heartbeat* oscillation of the microquasar IGR J17091-3624, discovered in this source in X-ray observations with RXTE in early 2011, (Altamirano et al., 2011a). Using the code, described in this Chapter, we model the accretion disk evolution responsible for the X-ray emission of the modeled source. We show that the variable wind outflow plays a role in regulating the amplitude and period of these oscillations.

3.1. The alpha disk model

In the standard α-model of the accretion disk (Shakura & Sunyaev, 1973), the non-zero component $\tau_{r\phi}$ of the stress tensor is assumed to be proportional to the total pressure. The latter includes the radiation pressure component, which scales with temperature as T^4 and blows up in hot, optically thick disks for large accretion rates. In general, an assumption about the dependence of $\tau_{r\phi}$ on the local disk properties leads to a specific prediction of the behaviour of the disk heating. This in turn affects the heating and cooling balance between the energy dissipation and radiative losses. Such a balance, under the assumption of hydrostatic equilibrium, is calculated numerically with a closing equation for the locally dissipated flux of energy given by the black hole mass and global accretion rate. The local solutions of the thermal balance and structure of a stationary accretion disk at a given radius may be conveniently plotted in the form of a so-called stability curve of the shape S. Here, distinct points represent a fixed annulus in a disk, with temperature and surface density determined by the accretion rate. For small accretion rates, the disk is gas pressure dominated and stable. The larger the global accretion rate, the larger part of the disk will be affected by the radiation pressure and the extension of the instability zone grows in radius. The hottest areas of the disk are heated rapidly, the density decreases, as the local accretion rate grows; more material is transported inwards. The disk annulus empties because of both increasing accretion rate and decreasing density, so there is no self-regulation of the disk structure. However, the so called 'slim-disk' solution (Abramowicz et al., 1988), where the advection of energy

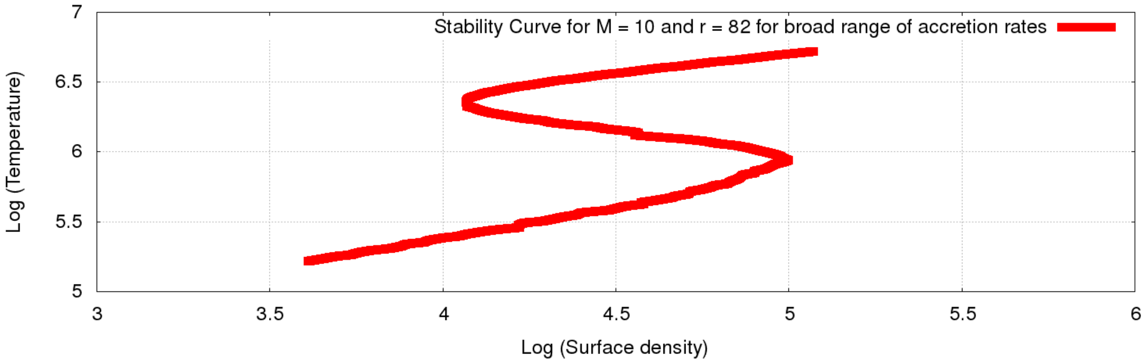

Figure 3.1: An example of the stability curve of the accretion disk ($M = 10 M_\odot$, $r = 82$ Schwarzschild radii).

provides an additional source of cooling in the highest accretion rate regime (close to or above the Eddington limit), provides a new stable branch. Hence, the advection of some part of energy allows the disk to survive and oscillate between the hot and cold states. Such oscillating behaviour leads to periodic changes in the disk luminosity. To model such oscillations, obviously, the time-dependent structure of the accretion flow needs to be computed, instead of the stationary solutions described by the S-curves.

3.1.1. Value of α viscosity parameter

The physical parameters of the model are the black hole mass, accretion rate (Eddington ratio) at the outer edge of the disk, and α viscosity. The first two parameters can be constrained from observation, but the value of α is chosen arbitrarily. In principle, it can be in the range $0 < \alpha < 1$. Our choice of $\alpha = 0.02$ as a reference value was motivated by observations of AGNs. Siemiginowska & Czerny (1989) interpreted the quasar variability as the local thermal timescale at a radius corresponding to the observed wavelength in the accretion disk, and they determined the value of 0.1 for a small sample of quasars. The same method, for larger sample objects (Palomar-Green quasar sample), gave the constraints $0.01 < \alpha < 0.03$ for sources with luminosities $0.01 L_{Edd} < L < L_{Edd}$ (Starling et al., 2004). Values in the range $0.104 < \alpha < 0.337$ were found for blazars from their intra-day variability (Xie et al., 2009) but those variations, even if related to the accretion disk, might be coming from Doppler-boosted emission and the timescale is then under-estimated. The stochastic model of AGN variability (Kelly et al., 2009; Kozłowski, 2016) allows for determination of the characteristic timescales and their scaling. Kelly et al. (2009) give the value of the viscosity parameter $\alpha = 10^{-3}$ estimated at the distance of 100 R_{Schw} , but the actual value implied by Eq. (5) in Kelly et al. (2009) is 0.2. This value would be lower if the radius was smaller. More precise results come from Kozłowski (2016)

$$\tau_{\text{char}}[years] = 0.97 \left[\frac{M}{8 \times 10^8 M_\odot} \right]^{0.38 \pm 0.15} . \tag{3.1}$$

This characteristic timescale is obtained at a fixed wavelength band, or disk temperature, and the location of a fixed disk temperature T in the Shakura-Sunyaev disk also depends on the black hole mass. We thus identify this timescale with the thermal timescale, and

N_p	period	error	variance	duration of outburst	error	variance	N_o
25	441.163	52.7	341.63	10.682	0.384432	2.5209	44
30	684	77.9	397.3	29.2857	3.81897	19.8076	27
40	1199	47.6	184.4	57.0582	2.8143	11.2537	16
50	1342	43.8	158.0	70.664	3.4465	12.8924	15
75	1381	21.1	76.0	76.6695	2.1083	7.8827	14
100	1402	18.5	64.2	78.5713	2.0588	7.42309	13

Table 3.1: Resulting heartbeat outbursts modeled with different grids. First column N_p, gives the number of grid points. Last column, N_o, gives the number of outbursts in time interval of 20 ks

obtain an expression for the viscosity parameter

$$\alpha = 0.4(\frac{T}{10^4 K})^{-2}\left[\frac{M}{8\times 10^8 M_\odot}\right]^{0.12\pm 0.15}. \tag{3.2}$$

We see that the viscosity does not depend on the black hole mass within the error. The variability study of Kozłowski (2016) was perfomed predominantly in the r band of the Sloan Digital Sky Survey (SDSS), centered at 6231 Å, with quasars being mostly at redshift 2. The conversion between the local disk temperature and the maximum disk contribution at a given wavelength is given approximately as $h\nu = 2.43kT$ (where h and k are the Planck and Boltzmann constants). Therefore, the dominant temperature in the Kozłowski (2016) sample is about 28 000 K, and the corresponding viscosity parameter is 0.044 for the black hole mass $\sim 8.0\times 10^8 M_\odot$ and 0.015 for $\sim 8.0\times 10^4 M_\odot$. Thus we assume the parameter $\alpha = 0.02$ in the model which we study in this and the next Chapters.

3.2. The code GLADIS

The heartbeat oscillations in IGR J17091 can be explained via intrisnsic oscillations of an accretion disk driven by the thermal-viscous instability. Using time-dependent code GLADIS [1], the evolution of an accretion disk responsible for the X-ray emission of the source is modeled with respect to the variable wind outflow. The code GLADIS was subsequently developed and applied in a number of works to model the evolution of accretion disks in Galactic X-ray binaries and AGNs (Janiuk & Czerny, 2005; Czerny et al., 2009; Janiuk & Misra, 2012).

3.2.1. The grid tests

The code allows for computations with a variable time-step down to a thermal timescale, adjusting to the speed of local changes of the disk structure. At first, we tested it and found that the denser grid results in perfectly regular flares. First, we tested the code parameterized with the accretion rate equal to the Eddington one, and central object mass of $M = 10M_\odot$. The grid covers the area from the inner radius R_{in} equal to 3 Schwarzschild radii to external radius equal to 100 Schwarzschild radii. In Table 3.1 we

---

[1] whose basic framework was initially described by Janiuk, Czerny & Siemiginowska (2002)

summarize the tests of our numerical grid. We see that denser grid leads to a better regularity of outbursts. For number of grid points equal to 100 the average period is equal to 1401.92 with variance of periods between outbursts equal to 64.1, which is less that 5 per cent. We conclude that outbursts are regular in our model and may accurately describe the heartbeat effect. This result will be used in this Chapter and the next Chapters.

3.3. Winds, jets and coronae - behind the standard accretion disk model

The accretion disk consists of highly-energetic plasma. Like any gas in thermal equilibrium in a gravitational well (e.g. like the Sun or other main sequence stars) the plasma in accretion disks contains some particles which are fast enough to escape from the gravitational field.

If the partile velocity at a given radius r exceeds the escape velocity, the flux of particles leaves the accretion disk in a form of wind.

If the partile energy at a given radius r is not large enuogh to make the particle velocity largen than escape velocity, the particles are freed from the disk flow and form a quasi-staic corona, being responsible for the non-thermal emission. The contribution of coronae dominates the source spectrum in the hard X-ray band (over 10 keV) of the soft states. The power law X-ray emission in the hard states likely comes from the innermost optically thin ADAF and/or very compact source, located close to the symmetry axis and possibly related to a failed jet.

In some of the disk states, the most energetic particles escape. Presence of the magnetic field helps in collimation of the wind flux. In some of the accretion disk sources, like Active Galactic Nuclei - quasars, and X-ray binaries - microquasars, the wind outflow is observed apart from very powerful jets with significant radio emission.

The wind forms an additional plasma present in the accretion disk neighbourhood. It can be detected via the absorption spectral lines, responsible for the transition between different ionization states of the elements. In case of the highly ionized heavy elements like Iron, their spectral lines reach the band of soft X-rays (e.g. about 6.9 keV for $K\alpha$ line of Fe XXVI, the Hydrogen-like Iron). The movement of the wind particles is visible in the shift of the lines, and line intensity contains information about the wind column density. Those quantities can be measured if the instrument resolution is good enough for detection of the spectral lines. The observations of the spectral lines taken from the Chandra HETG detector are important for the estimation of the wind strength in various X-ray sources (Miller et al., 2006; Netzer, 2006; King et al., 2012).

3.4. Possible interplay between wind and limit-cycle oscillations

The wind can play stabilizing role, holding back the effects from the radiation pressure instability. During the ejection, the local accretion rate and local density drops and the disk remains locally stable, especially in the hottest and most crucially instability-contributing annuli. As a result, the powerful instability is suppresed by the dropping

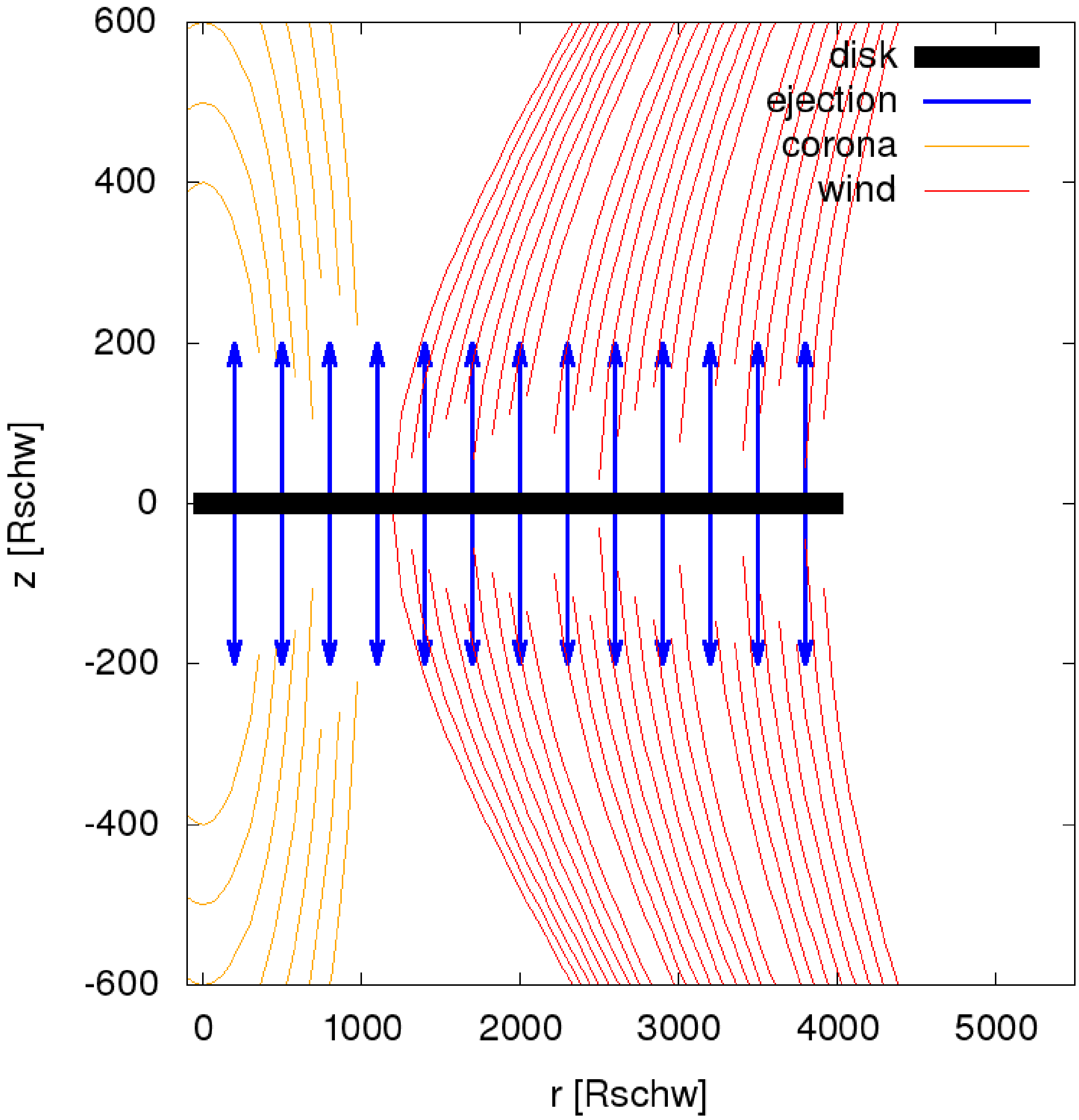

Figure 3.2: Scheme of the wind ejection from the accretion disk

optical depth making the cooling processes much more efficient in comparison to the viscous heating. This phenomenon found its confirmation in observations.

3.5. IGR J17091 microquasar

3.5.1. The discovery

The IGR J17091 microquasar has been discovered by Kuulkers et al. (2003) thanks to the data from the Integral satellite. This source has been classified as a black hole candidate. It is a moderately bright transient X-ray binary with peak flux level about 10 mCrab. Existence of IGR J17091-3624 has been previously confirmed in the archival data from TTM-KVANT (Revnivtsev et al., 2003) and *Beppo*SAX Wide Field Camera (in 't Zand et al., 2003). The source presents various variability patterns (Altamirano et al., 2011a), being similar to the GRS 1915+105, although the source is less luminous. There are many possible explaination of this source faintness is smaller BH mass.

3.5.2. IGR J17091 mass

For the purpose of models in this Chapter, we followed the results of Rebusco et al. (2012) which were obtained from the features of the high frequency Quasi Period Oscillations. Other method, used later by Iyer et al. (2015) determined its mass between 8.7 and 15.6 $M_{\odot}$, and the discussion about the exact mass value of the IGR J17091-3624 is still open. Nevertheless, the huge universality of the thin accretion disk model preserves the nature of the oscillation from the bias connected with the mass determination and the qualitative conclusions about wind-heartbeat correlation are general and, to some extent, are unsensitive on black hole mass. [2]

3.5.3. The time variability

Altamirano et al. (2011a) found several variability patterns of IGR J17091. The outburst from February, March and April 2011 have been recorded both by the SWIFT and RXTE satellite. The source peak increased up to 120 mCrab. The RXTE data showed a continous progression of quasi-periodic flare-like events with frequency $25-30$ mHz (Altamirano et al., 2011b). Altamirano et al. (2011b) classified the variability of IGR J17091 with the same scheme as Belloni et al. (2000) for GRS 1915+105, which has been classified into several variability classes. The flux intensity of IGR J17091-3624 is many times weaker than in GRS1915+105. It is thought that this can be caused by the lower BH mass in IGR J17091-3624 (Rebusco et al., 2012) or retrograde spin of IGR J17091 (Rao & Vadawale, 2012). To determine the timing behaviour of IGR J17091 and presence or absence of periodical flare-like events associated with the heartbeat state during a period that includes the four *XMM-Newton* and *Chandra* observations (April 2011 - October 2012), the analysis of the data collected by *Swift*/XRT $0.2-10$keV lightcurve was performed using the standard XRT pipeline. An example of the *Swift*/XRT heartbeat state observation of IGR J17091 is shown in Fig. (3.3).

---

[2] For the more detailed discussion about the relationship between the black hole mass and lightcurve parameters see next Chapter

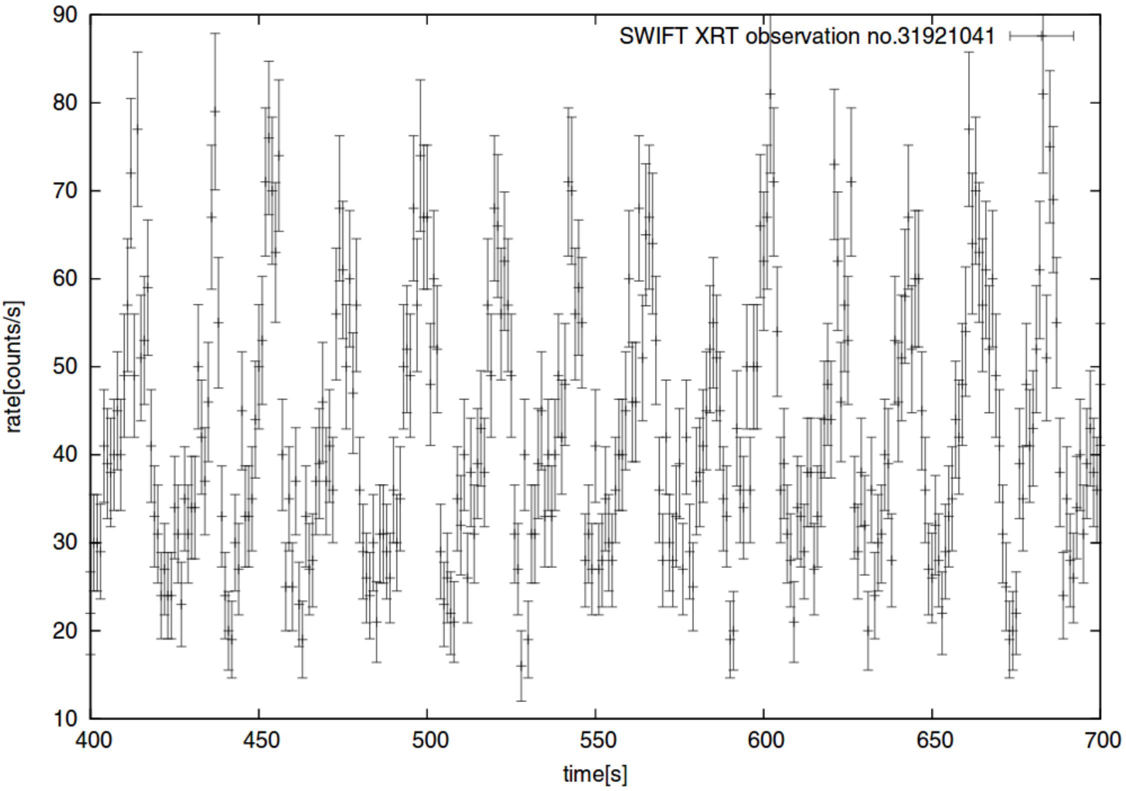

Figure 3.3: X-ray light curve of the source IGR J17091 as observed by *Swift*/XRT.The observation ID is 31921041.

The characteristic feature of the IGR J17091 is particularly fast and ionized wind observed during its soft spectral state (King et al., 2012). According to King et al. (2012) the wind, detected via Fe XXV (He-like) and Fe XXVI (H-like) blueshifted absorption lines gains the velocities up to 9000 and 15000 km s^{-1}. These values are significantly larger (an order of magnitude) than previously observed in stellar-mass black holes. According to the combined results from the SWIFT/XRT lightcurve and both Chandra and XMM-Newton spectral lines, the bluepresence of wind is anti-correlated with bluethe presence of the heartbeat oscillations. The observational confirmation of that correlation is presented in Fig. (3.4). The same correlation in the model is presented in Fig. (3.6).

3.5.4. The model of the wind

For the IGR J17091 modeling purpose, the variant version of the GLADIS code has been used with additional wind prescription (Janiuk, Czerny & Siemiginowska, 2002). We adopted a function that assumes the following wind-launching power, blueapproaching unity with growing Eddington ratio $\dot{m}$:

$$f_{\text{out}} = 1 - \frac{1}{1 + A\dot{m}} \tag{3.3}$$

The blueparameter A regulates bluethe amount of energy lost in the outflow, so the energy remaining bluein the disk is only a fraction of that produced bluein the disk. blueTherefore, in the energy conservation equation (2.31), the heating ratio Q_+ is replaced by $Q_+(1 - f_{\text{out}})$. The total ejection rate (the bluefraction of energy lost through the wind) in presented in Fig. (3.5) So the energy conservation equation gains the form:

$$\frac{\partial \log T}{\partial t} + v_r \frac{\partial \log T}{\partial r} = \frac{4 - 3\beta}{12 - 10.5\beta} \left(\frac{\partial \log \Sigma}{\partial t} - \frac{\partial \log H}{\partial t} + v_r \frac{\partial \log \Sigma}{\partial r} - v_r \frac{\partial \log H}{\partial r} \right) + \frac{Q_+(1 - f_{\text{out}}) - Q_-}{(12 - 10.5\beta)PH} \tag{3.4}$$

This assumption resulted in significant bluereduction of the ourburst amplitude. In Fig (3.6) we present two lightcurves for different wind parameters A. In Fig.(3.7) we present the blueglobal outburst properties - periods and relative amplitudes for chosen set of given A and $\dot{m}$.

3.6. Average mass loss, density, and column density of the wind

The mass-loss rate, describing the amount of matter escaping from the disk per unit of time per unit of disk area in the vertical direction is equal to the ratio of the locally generated flux in the accretion disk, with a fraction determined by f_{out} in Eq. (3.3), to the energy charge per particle, $\dot{m}_z = F_{\text{out}}/(\Delta E/m_p)$. The local flux is given by Eq. (2.18). The energy change per particle is on the order of the virial energy $\Delta E = Bk_B T_{\text{vir}}$, so it results in the final formula (in [g s^{-1} cm^{-2}])

$$\dot{m}_z = B^{-1} \frac{3}{4} \frac{1}{r} \Sigma v_r f(r) f_{\text{out}} \tag{3.5}$$

with f_{out} given by Eq. (3.3). The total mass loss is given by $\dot{m}_z$ over the disk is:

$$M_{\text{wind}} = \int_{R_{min}}^{R_{max}} dr \dot{m}_z 4\pi r. \tag{3.6}$$

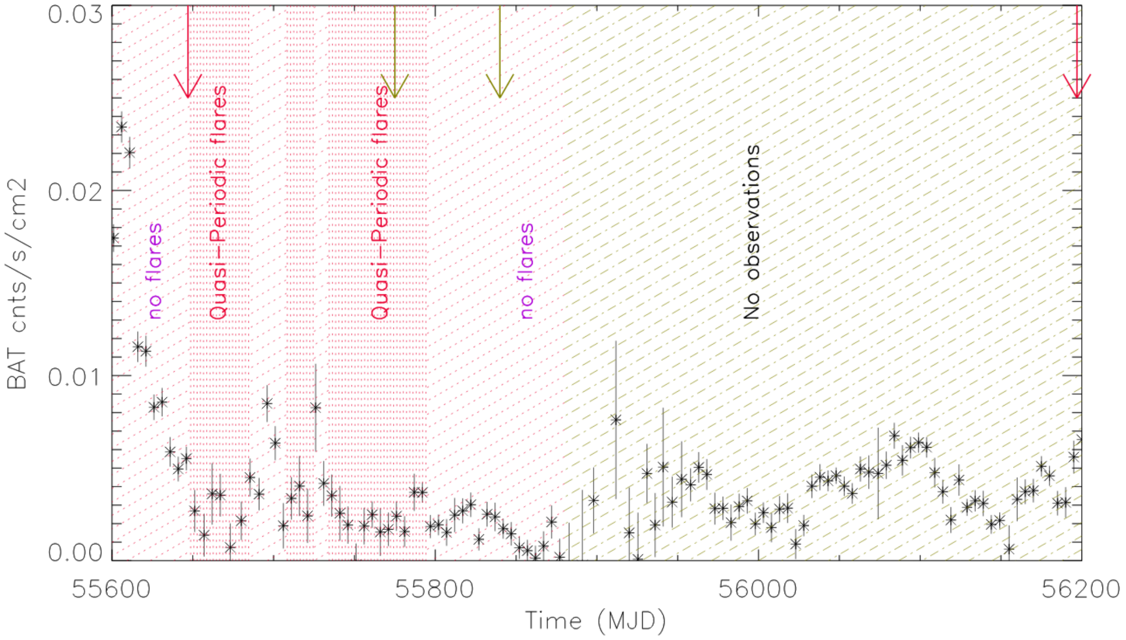

Figure 3.4: Swift/BAT 15 - 50 keV light curve shown on the background of a timeline sketch created from the Swift/XRT, RXTE/PCA,Chandra , and XMM data analysis, showing the anticorrelation between the wind and heartbeat in IGR J17091 The second Chandra observation (second green arrow) shows a fast, ionized wind, while the first XMM-Newton observation (first red arrows) and the first Chandra observation (first green arrow) lie in the heartbeat zone and do not show any detectable wind outflow. During the last XMM-Newton observation (second red arrow), the source is in a hard state. The parts with no flare are marked with red-oblique-dashed lines. Finally, the green-oblique-dashed lines bluemark periods without bluededicated observations.

Modified Julian Days and date:

MJD 55600 = 8th February 2011
MJD 55800 = 27th August 2011
MJD 56000 = 14th March 2012
MJD 56200 = 30th September 2012

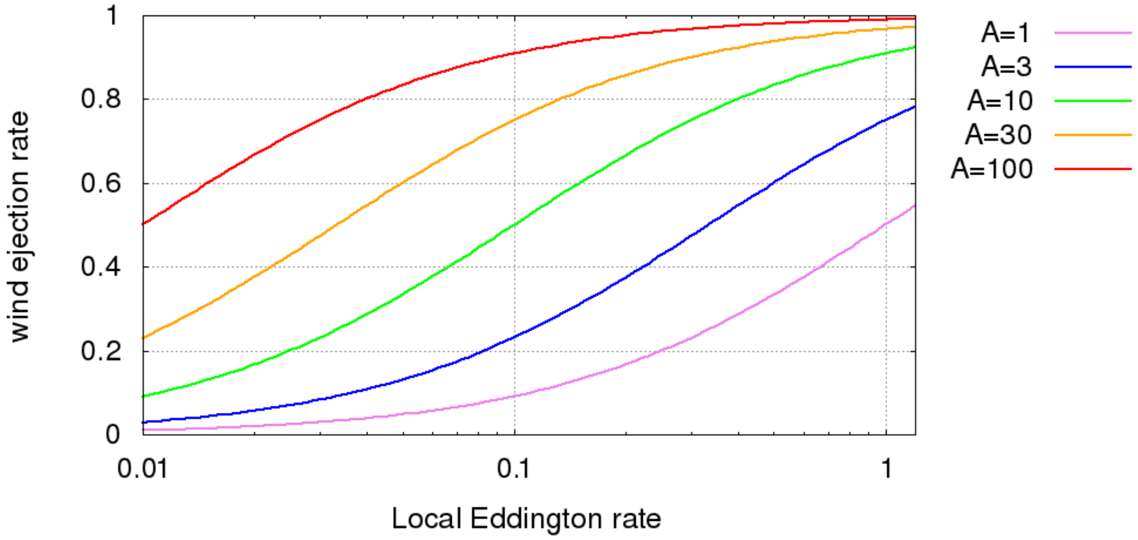

Figure 3.5: Dependence of the wind ejection rate on the wind strength parameter (Eq.(3.3))

We assume that outer radius of the accretion disk is equal to $4 \times 10^4 R_g$, which is the largest possible size in the IGR J17091, as estimated from the parameters of the binary. The smallest radius, R_{min}, according to the Schwarzschild solution, could be located at the marginally stable orbit around the black hole, that is, at $6\frac{GM}{c^2}$, for a nonrotating black hole.

We computed results for several values of the smallest radii from which the wind is launched, to fit its observational parameters. The actual mass loss will be at this order, or somewhat smaller, as the wind particles may be accelerated to obtain kinetic energy not necessarily equal to the virial energy, but rather having a velocity a few times their escape velocity at the radius r. Therefore the upper limit for the wind column density is calculated, depending on our model parameter A.

3.7. Comparison between the wind model and observations of IGR J17091

3.7.1. Spectral line analysis

King et al. (2012) reported about the particularly fast and ionized wind observed during the soft spectral state. Two detected lines (6.91 and 7.32 keV) can be associated with blueshifted He-like Iron Fe XXV and H-like Iron Fe XXVI with velocities 9000 and 15000 km s^{-1}. To sum up, the wind consists of two components:

1. *first*, faster, ejected with velocity $v_{w,1} = 15700 \pm 600$ km s^{-1}
2. *second*, slower, ejected with velocity $v_{w,2} = 9700^{+800}_{-700}$ km s^{-1}

According to above, those two components can correspond with two different ejection zones - faster component corresponds to lower radii and slower component correspond to larger radii. The photoionization modeling of the data presented in Fig. (3.8) allows the estimation of mass loss rates at the level of 2.7×10^{17} g s^{-1} and 4.2×10^{17} g s^{-1} in

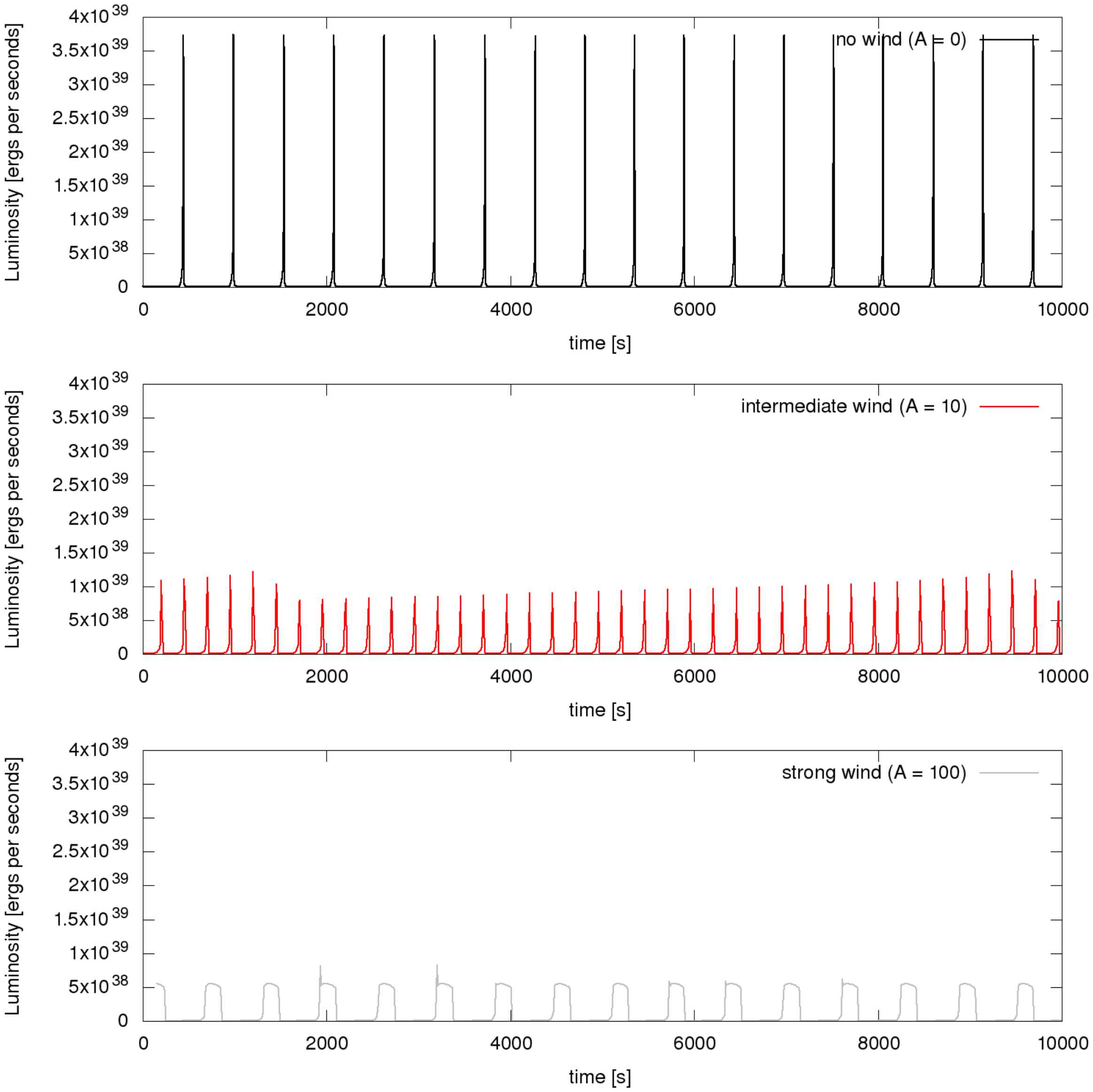

Figure 3.6: Model lightcurves for different jet ejection power A for $M_{\mathrm{BH}} = 6M_{\mathrm{odot}}$, $\alpha = 0.02$, $\dot{m} = 0.1$. **Upper panel:** Model lightcurve for $A = 0$. **Middle panel:** Model lightcurve for $A = 10$. **Lower panel:** Model lightcurve for $A = 100$

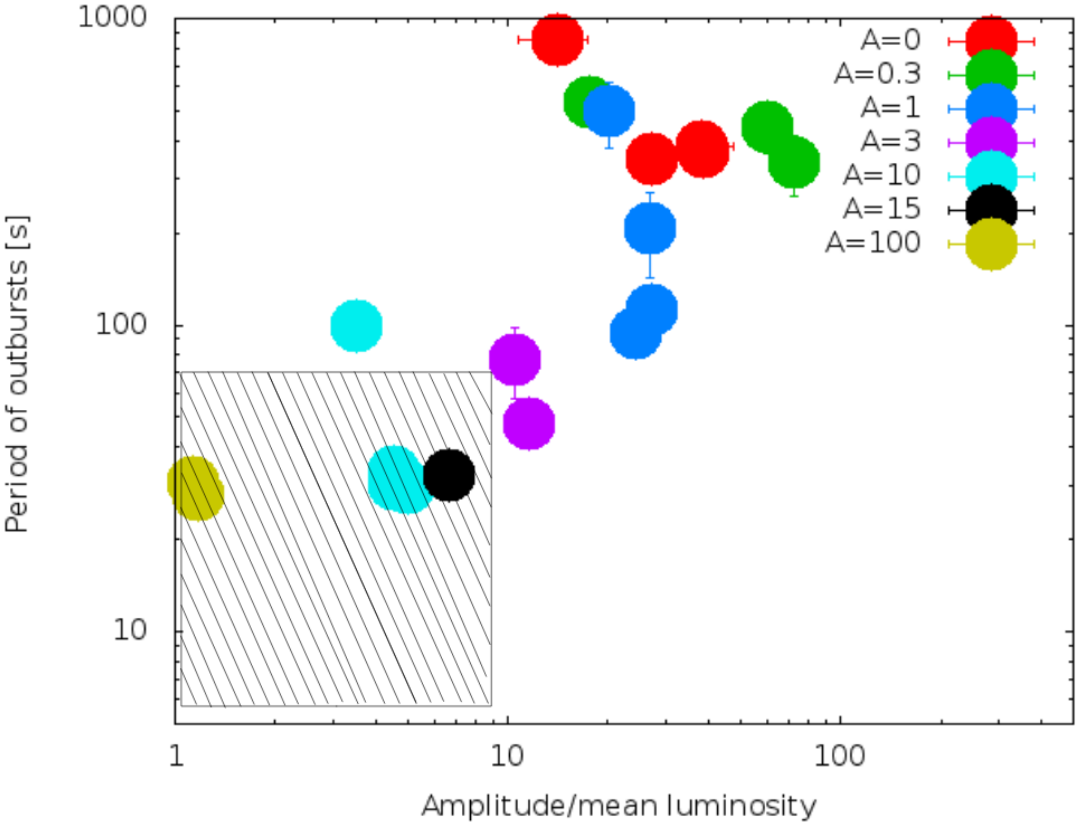

Figure 3.7: Dependence of the outburst amplitudes and periods on the wind strength A. Shaded regions mark observed amplitudes and timescales of the microquasar heartbeats. Different colors mark different values of the parameter, as indicated in the plot. Models were ran for $\dot{m}$ between 0.1 and 0.4. In general, the lower the accretion rates, the shorter the outbursts, as long the instability occurs.

case of the quiescence state and 2.5×10^{16} g s^{-1} and 3.9×10^{16} g s^{-1} in the heartbeat variable state [3]. For this Chapter, we adopted the black hole mass in the IGR J17091 microquasar to be equal of $6M_{\odot}$.

3.7.2. Mass loss and ejection radii

Studying the radial profiles of the local accretion rate can help estimate of the wind ejection zones. The innermost area of the accretion disk in the heartbeat states is strongly thermally unstable. The dynamical processes results in complicated temporal and spacial behaviour of vertical ejection rate $\dot{m}_z(r)$.

For radii below 70 Schwarzschild radii, the dependence of $\dot{m}_z(r)$ derived from Eq. (3.5) is a complicated function, while at larger radii it scales with radius as a simple power law with index -1.8. Therefore this relation and its normalization to best-fit model for the heartbeat oscillating disk was fitted, that is, with $A = 15$. After simple integration:

$$\dot{M}_{wind}(r, R_{max}) = 1.635 \times 10^{16}(R_{max}^{0.2} - r^{0.2})\frac{\mathrm{g}}{s} \tag{3.7}$$

where in the above the argument $r = R_{min} \leq 70$ is expressed in Schwarzschild radii units. From this relation, the extension of the wind-launching zone is constrained, taking into account the radius r determined by the velocity of the wind equal to the escape velocity at that radius, which can be constrained by the spectral analysis (provided the wind is detectable in the data). Thus for the two wind components the minimal radii are at the ranges of $R_{\rm min,1} = 380\ R_{\rm Schw}$ and $R_{\rm min,2} = 950\ R_{\rm Schw}$ respectively. Furthermore, the strong dependence of the wind mass-loss rate on the strength parameter can be noted. With $A = 300$, a stable disk solution is found in our simulations, while the mass-loss rate $\dot{M}_{\rm wind}$ wind is about ≈ 12 times higher than for our heartbeat model with $A = 15$. Such a strong wind definitely stabilizes the heartbeat oscillations, while it should give clear observable signatures in the *Chandra* spectra, such as those which are presented in Fig. 3.8. Taking the values of the wind velocities and mass-loss rates to be the same as those in the 12406 *Chandra* observation, the wind-launching zones are estimated at the level $950 - 4200$ and $380 - 4700$ Schwarzschild radii for the first and second wind components.

3.7.3. Wind density

The wind mass-loss changes in time as a result of the outbursts. Averaging the solutions, the total mass loss caused by the wind is obtained at the level of $\dot{M}_{wind} = 3 \times 10^{16} - 2 \times 10^{17}$g s^{-1}. The wind density at R_{max} is equal to:

$$\rho_{wind}(R_{max}) = \frac{\dot{M}_{wind}}{4\pi R_{max}^2 v_{\rm esc}} \tag{3.8}$$

where v_{esc} is the escape velocity at R_{min}. In best-fit heartbeat model, which is obtained with $A = 15$ to reproduve the oscillations amplitude and period,the density of the wind is equal to $\rho_{wind} = 2 \times 10^{-16} - 7.2 = 2 \times 10^{-16}$ g cm^{-3}, depending on the wind-launching radius. Assuming that wind consists of protons, regarding the fact that $\rho_{wind} \approx R^{-2}$ the column density of the (spherically symmetric) wind is calculated. The observable column

---

[3] Those values are estimations are the upper limits, since no significant wind component for that source has been found

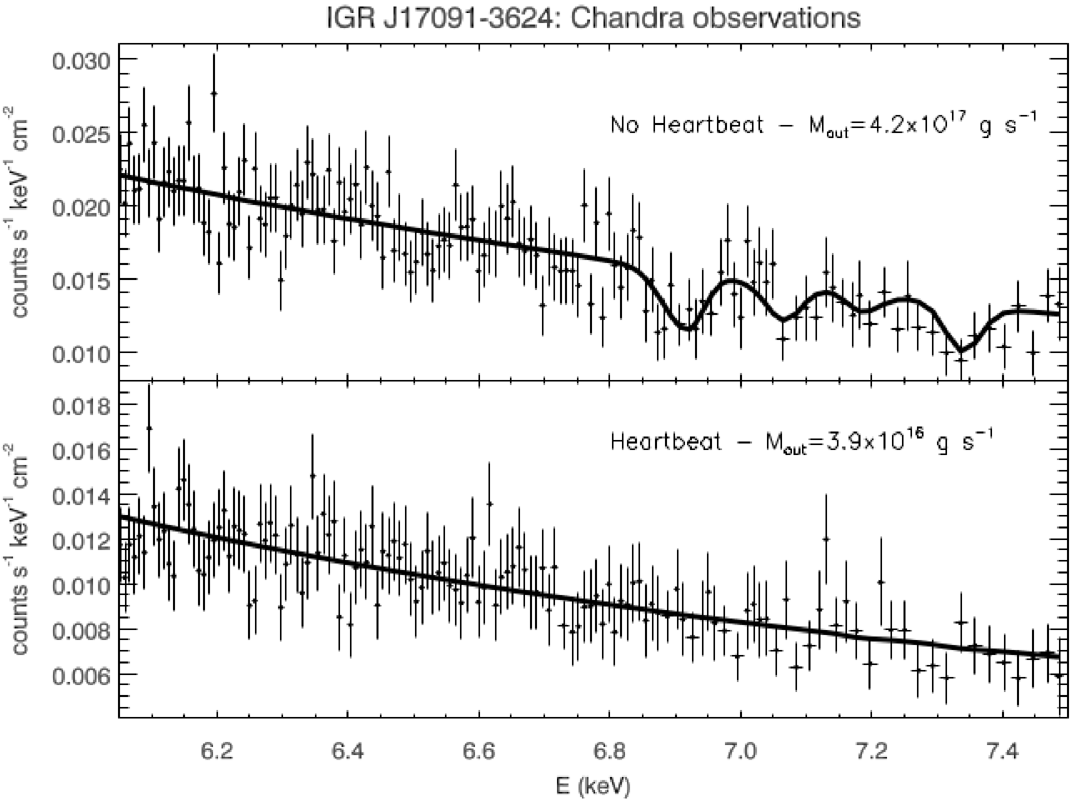

Figure 3.8: Chandra ACIS-S HETG spectra for observations 12406 (upper panel) and 12405 (lower panel) in the $6 - 7.5$ keV energy range.

R_{min}	$\dot{M}_{\mathrm{wind}}$ [g s^{-1}]	ρ_{wind} [g cm^{-3}]	N_{H} [cm^{-2}]
3	$2.18 \cdot 10^{17}$	$2.0 \cdot 10^{-16}$	$5.66 \cdot 10^{21}$
70	$8.84 \cdot 10^{16}$	$3.9 \cdot 10^{-16}$	$1.10 \cdot 10^{22}$
150	$7.68 \cdot 10^{16}$	$5.0 \cdot 10^{-16}$	$1.07 \cdot 10^{22}$
350	$6.04 \cdot 10^{16}$	$7.1 \cdot 10^{-16}$	$2.00 \cdot 10^{22}$
2000	$3.06 \cdot 10^{16}$	$7.2 \cdot 10^{-16}$	$2.04 \cdot 10^{22}$

Table 3.2: Exemplary results of the disk/wind model. The parameters are accretion rate $\dot{m} = 0.1$, wind strength $A = 15$, black hole mass $M = 6M_{\odot}$, wind extension $R_{\mathrm{max}} = 40000R_g$. The column density is calculated assuming $f_1 = 0.0015$.

number density of particles is then be given by $N_H = \rho_{wind}(R_{max})R_{max}(fm_p)^{-1}$, where f is the filling factor, in principle unknown. The filling factor is a correction describing the geometry of the gas distribution. The resulting wind mass-loss rate and density for wind strength parameter $A = 15$ and several values of the inner radius at which the wind is launched are summarized in Table 3.2.

3.8. Discussion

3.8.1. General picture for the IGR J17091

In microquasar IGR J17091 the wind consists of two different components. The time-dependent radiation pressure dominated disk instability model implemented by the GLADIS code reproduces the anti correlation between the wind ejection rate and the occurrence of heartbeat oscillations.

Now, the question remains whether the bound wind, ejected with the velocities that are below the escape velocity for a black hole with accretion disk, is observationally detectable. This part of the flow, also crucial for stabilizing the accretion disk oscillations, could contribute to the hard X-ray corona (see Fig. 3.2).

In general, the coronae in X-ray binaries are visible as the power-law tails in the spectra in hard X-ray band, being the most significant in the hard states (See Fig. 1.11).

Indeed, as Fig. (3.4) shows, there are no strong correlation between the flaring and non flaring activity and the $15 - 50$ keV hard X-ray emission. A slight drop in the hard X-ray emission can be noticed during the flaring states.

3.8.2. Viability of the radiation pressure instability model in the context of wind

The best-studied example of the radiation pressure instability in action is the microquasar GRS 1915+105, which in some spectral states exhibits cyclic X-ray outbursts that fit limit-cycle oscillations of an accretion disk well. This source has been known for 20 years, and only recently another microquasar of that type was discovered. This is IGR J17091, the second excellent candidate source that shows radiation-pressure-driven variability on observable timescales.

In addition, other selected Galactic X-ray binaries that were discussed in more detailed way in Janiuk & Czerny (2011) support that there are P_{rad} instabilities in their accretion disks. Nevertheless, many sources accretes at a high accretion rate to even Eddington rate ratios that show no limit-cycle oscillations on timescales adequate for the radiation pressure instability. Some stabilizing mechanisms need to be considered to explain the apparent stability of the high accretion rate sources. One plausible mechanisms discussed in the literature possibly affecting the stability of accretion disks is the jet or wind outflow.

The luminosity outbursts for the pure radiation pressure instability are too large with respect to the amplitudes observed in IGR J17091. The most plausible scenario is that the energetic wind is launched from the accretion disk and partially stabilizes it, depending on its strength and mass-loss rate. The range of plausible wind strengths based on the timescales and amplitudes of the disk flares they allow was determined. The wind may either partially stabilize the disk oscillations to produce regular outbursts, but of moderate amplitudes, or even completely stabilize the disk.

In the spectroscopic observations, it may not always be detectable because of its high ionization state or because the velocities required very close to the black hole are below the escape velocity; in that case, the MHD mechanism instead drives the formation of a quasi-static bound corona above the disk. However, the observed winds agree well with the scenario described by our model.

Nevertheless, the wind is only one out of the possible stabilizing effects in the accretion disks. More detailed discussion on the accretion disks stability will be presented in the next Chapter.

3.9. Conclusions

Our final conclusions from the comparison of the wind-heartbeat interplay are as follows:

1. The heartbeat oscillations of the X-ray luminosity of IGR J17091 detected during its outburst in 2011 are attributed to the radiation pressure instability of the accretion disk.
2. The outflow launched from the disk at the cost of part of the locally dissipated energy flux is a plausible mechanism to regulate the amplitude of these oscillations.
3. The strong outflow may stabilize the disk and completely suppress the heartbeat.
4. The observed properties of the wind detected from IGR J17091 in the state without the heartbeats allowed us to constrain the the mass-loss rate at large distances in the disk.

Chapter 4

Generalized model with modified viscosity

4.1. Introduction

This Chapter presents a general model of the visco-thermal instabilities in the accretion disks, extending the previous approach. Chapter 3 was devoted to modeling of one source - microquasar IGR J17091. We showed anticorrelation between the limit-cycle oscillations and the wind outflow, verified by the spectral and timing analysis. Nevertheless, the model presented in Chapter 3 involved only the special case of detectable wind. In the absence of detectable wind, the X-ray lightcurve appears to be only probe of the internal accretion disk and black hole parameters.

Because of the ubiquity of accretion disks sources this topic deserves more detailed studies. Black hole masses range from stellar mass black holes in X-ray binaries, through intermediate mass black holes (IMBHs), up to the supermassive black holes in quasars and active galaxy centers (AGNs). The geometrically thin, optically thick accretion disk that is described by the theory of Shakura and Sunyaev is probably most relevant for the high/soft spectral states of black hole X-ray binaries, as well as for some active galaxies, such as Narrow Line Seyfert 1s and numerous radio quiet quasars (Brandt et al., 1997; Peterson et al., 2000; Foschini et al., 2015).

The topic of this Chapter is dependence between the non-diagonal terms of stress tensor $T_{\mathrm{r}\phi}$ (determining the viscous dissipation in accretion disk) on the pressure-contributing factions - gas pressure P_{gas} and radiation pressure P_{rad}. In the simplest possible case, the viscous dissipation might be proportional to the total pressure.

The accretion disk is described by 5 local variables - thickness H, density ρ, temperature T and pressures P_{rad} and P_{gas}. The following assumptions:

1. Thermal equilibrium between gas and radiation
2. Equations of state
3. Hydrostatic equilibrium in vertical direction

reduce the numbers of local parameters in the hydrodynamical model (neglecting the magnetic field extra degrees of freedom) to 2, so any possible phenomenological prescription for $T_{\mathrm{r}\phi}$ can be written as a function on the gas and radiation, or gas and total pressure. To simplify, we can write

$$T_{\mathrm{r}\phi} = \alpha P f(\beta) \tag{4.1}$$

where $\beta = \frac{P_{\mathrm{gas}}}{P}$ is gas-to-total pressure ratio, and f is a regular continous function tending to 1 if only β tends to 1. The case of $f(\beta) = 1$ has been included in the the simple albeit powerful α prescription for the viscosity in the accreting plasma, introduced by Shakura & Sunyaev (1973) and used in Chapter 3 to determine heating in the accretion disk. This simple scaling of viscous stress with pressure is also reproduced in the more recent numerical simulations of magnetised plasmas (Hirose et al., 2006; Jiang et al., 2013; Mishra et al., 2016), however being not capable to model the global dynamics and fit the observations. In this thesis, we advocate the global model governed by the set of equations (2.24, 2.31) being able to reproduce the observable effects like regular changes in disk luminosity like $\rho - class$ variability of the sources GRS 1915 and IGR J17091. In particular, the function f can model such effects like the stabilizing influence of the magnetic field on the disk.

In this Chapter I study a broad range of theoretical models of radiation-pressure-driven flares and prepare the results to confront with observational data. The appearance of the radiation pressure instability in hot parts of accretion disks can lead to significant outbursts for all scales of the black hole mass. Temperature and heat production rate determine the outburst frequency and shape. Different effective prescriptions for turbulent viscosity affect the instability range and the outburst properties. Thus, by confronting the model predictions with observed flares, the constraints can be put on those built-in assumptions. In the current Chapter we make a systematic study showing how the model parameters modify the local stability curve and global disk behaviour. The parameter space of the model is expanded. The methodology is modified, extended by the parameter μ, which allows for a continuous transition between the gas and radiation pressure dominated cases. The wind outflow is neglected, though, as in many sources the observable constraints for its presence are too weak.

In this Chapter, the key parameters characterising the data are determined. This approach makes the dependence of the models on the parameters much more clear, and it allows for much easier comparison of the model with observational data.

4.2. Observational universality of disk oscillations

4.2.1. X-ray binaries

The time-dependent effects connected with non-stationary accretion are clearly important. In particular, a number of observational facts support the idea of a cyclic activity in the high-accretion-rate sources. One of the best studied examples is the microquasar GRS 1915+105, which in some spectral states exhibits cyclic flares of its X-ray luminosity, well fitted to the limit cycle oscillations of an accretion disk on timescales of tens or hundreds of seconds (Taam et al., 1997; Belloni et al., 2000; Neilsen et al., 2011). Those heartbeat states are known since 1997, when the first XTE PCA observations of this source were published (Taam et al., 1997), while recently yet another microquasar of that type, IGR J17091-3624, was discovered (Kuulkers et al., 2003; Capitanio et al., 2009). The heartbeat states were also found for this source (Altamirano et al., 2011a; Capitanio et al., 2012; Pahari et al., 2014; Janiuk et al., 2015). Furthermore, a sample of sources proposed in Janiuk & Czerny (2011) was suggested to undergo luminosity oscillations, possibly induced by the non-linear dynamics of the emitting gas. This suggestion was confirmed by the recurrence analysis of the observed time series, presented in Suková et al. (2016).

One possible driver of the non-linear process in the accretion disk is its thermal and viscous oscillation induced by the radiation pressure term; it can be dominant for high enough accretion rates in the innermost regions of the accretion disk, which are the hottest. The timescales of such oscillations depend on the black hole mass, and are on the order of tens to hundreds of seconds for stellar mass BH systems.

4.2.2. Active Galactic Nuclei

For a typical supermassive black hole of $10^8 \mathrm{M}_\odot$, the process would require timescales of hundreds of years. Therefore, in active galactic nuclei (AGNs) the evolution under the radiation pressure instability can not be observed directly. Nevertheless, statistical studies may shed some light on the sources' evolution. For instance, the Giga-Hertz Peaked quasars (Czerny et al., 2009) have very compact sizes, which would directly imply their ages. In the case of a limit-cycle kind of evolution, these sources would in fact not be very young, but 'reactivated'.

4.2.3. Intermediate-Mass Black Holes

Another class of objects, which are claimed to contain the BH accretion disk, are the Ultraluminous X-ray sources (ULXs). ULXs are a class of sources that have a luminosity larger than the Eddington one for the heaviest stellar-mass objects ($> 10^{40}$ ergs s^{-1}). Therefore, ULXs are frequently claimed to contain accreting black holes with masses larger than the most massive stars and lower than AGNs ($10^3 - 10^6 M_\odot$). They are called intermediate-mass black holes (IMBHs). In some of such sources, the radiation pressure instability were found.

4.3. Model

4.3.1. Expression for the stress tensor - different prescriptions

The difficulty in finding the proper physical description of the turbulent behaviour of gas in the ionised area of an accretion disk led to the adoption of several distinct theoretical prescriptions of the non-diagonal terms in the stress tensor term $T_{\mathrm{r}\phi}$. Gas ionisation should lead to the existence of a magnetic field created by the moving electrons and ions. The magnetic field in the disk is turbulent and remains in thermodynamical equilibrium with the gas in the disk. For a proper description of the disk viscosity, different complex phenomena should be included in $T_{r\phi}$. For a purely turbulent plasma we can expect the proportionality between the density of kinetic energy of the gas particles and the energy of the magnetic field (Shakura & Sunyaev, 1973). However, the disk geometry allows the magnetic field energy to escape (Sakimoto & Coroniti, 1989; Nayakshin et al., 2000). Following Shakura & Sunyaev (1973), one can therefore assume that the non-diagonal terms in the stress tensor are proportional to the total pressure with a constant α:

$$T_{\mathrm{r}\phi} = \alpha P. \tag{4.2}$$

On the other hand, Lightman & Eardley (1974) proved the instability of the model described by Shakura & Sunyaev (1973). Following that work, Sakimoto & Coroniti (1981) proposed another formula which led to a set of stable solutions without any appearance of the radiation pressure instability:

$$T_{\mathrm{r}\phi} = \alpha P_{\mathrm{gas}}. \tag{4.3}$$

Later, Merloni and Nayakshin motivated by the heartbeat states of GRS 1915+105, investigated the square-root formula. Their results are presented in paper (Merloni & Nayakshin, 2006). The formula is given by:

$$T_{\mathrm{r}\phi} = \alpha\sqrt{PP_{\mathrm{gas}}}. \tag{4.4}$$

This prescription was introduced by Taam & Lin (1984) in the context of the Rapid Burster and used later by Done & Davis (2008) and Czerny et al. (2009) both for Galactic sources and AGNs. In the current work, a more general approach is applied, along with the introduction of the entire family of models, with the contribution of the radiation pressure to the stress tensor parameterised by a power-law relation with an index $\mu \in [0, 1]$. We therefore construct a continuous transition between the disk, which is totally gas pressure dominated, and the radiation pressure that influences the heat production (Szuszkiewicz, 1990; Honma et al., 1991; Watarai & Mineshige, 2003). The formula for the stress tensor is a generalisation of the formulae in Equations (4.2), (4.3), (4.4) and is given by:

$$T_{\mathrm{r}\phi} = \alpha P^{\mu} P_{\mathrm{gas}}^{1-\mu}. \tag{4.5}$$

In this work, the behaviour of the accretion disk with the tensor formula (4.5) is investigated for a very broad range of black holes and different values of μ. A similar analysis has been performed also by Merloni & Nayakshin (2006) for different values of α (here, α is fixed with a constant value, which is at the level of 0.02). Regarding the existence of a magnetic field inside the accretion disk, the viscosity can be magnetic in origin, and can reach different values for differently magnetised disks. As the strong global magnetic field can stabilise the disk (Czerny et al., 2003; Sądowski, 2016), the parameter μ can be treated as an effective prescription of magnetic field.

4.3.2. Parameters and characteristics of the results

Starting from the time-dependent computations from a certain initial state, the disk evolves for some time until the disk develops a specific regular behaviour pattern. Different variability patterns (a constant luminosity of the disk, i.e. stable solution, flickering, or large flares) depend on the input parameters. We parameterise the models by the global parameters: the black hole mass M, the external accretion rate, as well as the physical prescription for the stress, α and μ. In this study we mostly limited our modelling to a constant (arbitrary) value of $\alpha = 0.02$, since the scaling with α is relatively simple, and we wanted to avoid computing the four-dimensional grid of the models. We discussed our motivation in Chapter 3, and here we also perform a limited analysis of the expected dependence on this parameter. Those parameters are not directly measured for the observed sources. In the current work, we focus on the unstable accretion disks. We thus construct from our models a set of output parameters that can be relatively easily measured from the observational data: the average bolometric luminosity L, the maximum bolometric luminosity L_{max}, the minimum bolometric luminosity L_{min}, the relative amplitude of a flare, $A = \frac{L_{\mathrm{max}}}{L_{\mathrm{min}}}$), and the period, P. In order to parameterise the shape of the light curve, a dimensionless parameter Δ is introduced. The Δ is equal

Value	Symbol
Black hole mass	M
Accretion rate	$\dot{m}$
First viscosity parameter	α
Second viscosity parameter	μ

Table 4.1: Summary of the model input parameters

Value	Symbol
Bolometric luminosity	L
Period	P
Amplitude ($L_{\max}/L_{\min}$)	A
Flare duration to period ratio	Δ

Table 4.2: Summary of the characteristic quantities used to describe the accretion disk flares

to the ratio of the flare duration to the period. Flare duration is defined as the time between the moments where the luminosity is equal to $(L_{\max}+L_{\min})/2$ on the ascending slope of the flare, and the luminosity $(L_{\max}+L_{\min})/2$ on the descending slope of the flare. We then compare L, A, P and Δ obtained for several distinct black hole mass scales. In Table 4.1 the model input parameters are summarized. The accretion rate $\dot{m}$ is presented in Eddington units $\dot{m} = \frac{\dot{M}}{\dot{M}_{Edd}}$. The Eddington accretion rate $\dot{M}_{Edd}$ is proportional to the Eddington luminosity, and inversely proportional to the accretion efficiency $\dot{M}_{Edd} = \frac{L_{Edd}}{\eta c^2}$. Accretion efficiency is assumed at the level of $\eta = \frac{1}{16}$ for all models and ISCO at the level of $6\frac{GM}{c^2}$.

In Table 4.2 we summarise the probed characteristics of the accretion disk flares are summarized.

4.4. Local stability analysis

We first perform a local stability analysis in order to formulate basic expectations and limit the parameter space. In general, the disk is locally thermally unstable if for some temperature T and radius r, the local heating rate grows with the temperature faster than the local cooling rate:

$$\frac{d\log Q_+}{d\log T} > \frac{d\log Q_-}{d\log T}. \tag{4.6}$$

In this analysis, the timescales were considered as different for the thermal and viscous phenomena which is justified for a thin disk.

4.4.1. Stability and timescales

For thin, opaque accretion disks, there appears a strong timescale separation between thermal (connected with the local heating and cooling) and viscous phenomena. The thermal timescale, for a disk rotating with angular velocity Ω, is $t_{\text{th}} = \alpha^{-1}\Omega^{-1}$. The appearance of viscous phenomena, connected with the large-scale angular momentum transfer is connected with the disk thickness, so that $t_{\text{visc}} = t_{\text{th}}\frac{R^2}{H^2}$. We focus now on the thermal phenomena. On thermal timescales the local disk surface density is constant, and only the vertical inflation is allowed. Therefore, for the thermal timescale $\Sigma \approx const.$ From Eqs. (2.20) and (4.5):

$$Q+ = \frac{3}{2} C_1 \alpha P^{\mu} P_{\rm gas}^{1-\mu} H \Omega. \tag{4.7}$$

Assuming that the disk maintains the vertical hydrostatic equilibrium $H = P/(C_3 \Sigma \Omega^2)$, and defining $x = \frac{P_{\rm gas}}{P_{\rm rad}} + 0.5$. Eq. (4.7) can be rewritten as:

$$Q_+ = \alpha \frac{3}{2C_3 \Sigma \Omega^2} P^{1+\mu} P_{\rm gas}^{1-\mu} = \frac{3}{2} \frac{\alpha}{C_3 \Sigma \Omega^2} P_{\rm rad}^2 (x+1/2)^{1+\mu} (x-1/2)^{1-\mu}. \tag{4.8}$$

Then, if we assume a constant Σ regime:

$$\frac{dx}{dT} = -\frac{7}{2} \frac{(x+1/2)(x-1/2)}{2xT}, \tag{4.9}$$

we get

$$\frac{d \log Q_+}{d \log T} = 1 + 7\mu \frac{1-\beta}{1+\beta}, \tag{4.10}$$

where $\beta = \frac{P_{gas}}{P} = \frac{x-1/2}{x+1/2}$. Finally, from Eq. (4.10) and Eq. (4.6):

$$\frac{d \log Q_+}{d \log T} > 4, \tag{4.11}$$

which is fulfilled if the condition:

$$\beta < \frac{7\mu - 3}{7\mu + 3} \tag{4.12}$$

is satisfied (Szuszkiewicz, 1990). This gives the necessary condition for the instability for the case of μ-model, so that the instability occurs only if $\mu > 3/7$.

4.4.2. Magnetised disk and its equivalence to μ model

The existence of strong magnetic fields can stabilise the radiation-pressure dominated disk (Zdziarski & Svensson, 1994; Czerny et al., 2003; Sądowski, 2016). We can assume a significant magnetic contribution to the total pressure P, defining it as follows:

$$P = P_{\rm rad} + P_{\rm gas} + P_{\rm mag}. \tag{4.13}$$

Let us define the disk magnetisation coefficient $\beta' = \frac{P_{mag}}{P}$. The formula (4.13) was put into the Shakura-Sunyaev stress-energy tensor (i.e. for $\mu = 0$ in Eq. 4.8), and then:

$$\frac{d \log Q_+}{d \log T} = 8(1 - \beta'). \tag{4.14}$$

Here, the value of $\beta' = \frac{1}{2}$ means that there is an equipartition between the energy density of the gas, radiation and magnetic energy density. It corresponds to the complete stabilisation of the disk, so that $\frac{d \log Q_+}{d \log T} \leq \frac{d \log Q_-}{d \log T}$. From the formula (4.12), β' and μ can be connected as follows:

$$\mu = 1 - \frac{8}{7}\beta'. \tag{4.15}$$

Regarding the observed features, the model of the magnetised disk is equivalent to the μ model for the radiation-pressure dominated disks in terms of appearance of thermal instability.

4.4.3. Disk magnetisation and flare amplitude

The energy equation (2.31) can give us a direct connection between the heating rate and pressure. Under assumption that the heating rate dominates the cooling rate:

$$\frac{dT}{dt} = CT^{7(\mu-1)}, \tag{4.16}$$

where C is a constant, since in thermal timescale we can neglect viscous processes like radial flow. C depends on local values of Σ and Ω. This simple, first-order differential equation gives us the following dependence on the heating growth:

$$\frac{d\log T}{d\log t} = \frac{1}{7(1-\mu)}. \tag{4.17}$$

It explains why flares can be possibly sharper for bigger μ.The above formula gives a linear, approximate estimation of the solution of the full, non-linear model, presented in the following Sections of this Chapter. This feature is directly confirmed in the Fig. (4.10). It can also give another criterion for determination of a proper value of μ, and can be used as a test for the validity of μ-model in confrontation with the observational data. Most of the luminosity comes from a hot, inner thermally unstable region of the disk ($r \approx< 70r_{\rm Schw}$), and the colder, outer thermally stable region gives only minor contribution to the total luminosity:

$$\frac{d\log L}{d\log t} = \frac{4}{7(1-\mu)}. \tag{4.18}$$

Regarding the timescale separation, and assuming that the flaring of the disk is stopped by the viscous phenomena after $t \approx t_{\rm visc}$, we get the following formula for the dependence between the relative amplitude $A = \frac{L_{\rm max}}{L_{\rm min}}$ and the viscous to thermal timescales rate:

$$\log A = \frac{4}{7}\frac{1}{1-\mu}\log\left[\frac{t_{\rm visc}}{t_{\rm th}}\right]. \tag{4.19}$$

Furthermore, a useful formula that connects the presence of magnetic fields can be derived along with the amplitude of the limit-cycle oscillations:

$$\log A = \frac{1}{2}\frac{1}{\beta'}\log\left[\frac{t_{\rm visc}}{t_{\rm th}}\right]. \tag{4.20}$$

In the rest of this Chapter, a more detailed analysis of the relation between the outburst amplitude and other light curve properties on the μ parameter will be presented, which is possibly corresponding to the scale of magnetic fields.

4.5. Results - stationary model

First, an exemplary set of stationary models was computed, to verify the expected parameter range of the instability. Eq. (4.12) gives the relation between the maximum gas-to-total pressure ratio and the minimum value of the μ parameter. Numerical computations are performed for an intermediate black hole mass of $3 \times 10^4 M_\odot$, and I plot the stability curve at the radius $R = 7.82 R_{Schw} = 15.74\frac{GM}{c^2} = 6.88 \times 10^{10}$cm. The disk is locally unstable if the slope $\frac{\partial\Sigma}{\partial T}$ is negative (Eq. (4.6)). It gives the necessary, but not the sufficient condition for the global instability, as for the appearance of the significant flares, the area of the instability should be sufficiently large. We compute the S-curves (see Chapter 3), which are presented in Fig. (4.1) for different values of μ. The wider μ, the bigger the negative slope area on the S-curve, and therefore the larger the range

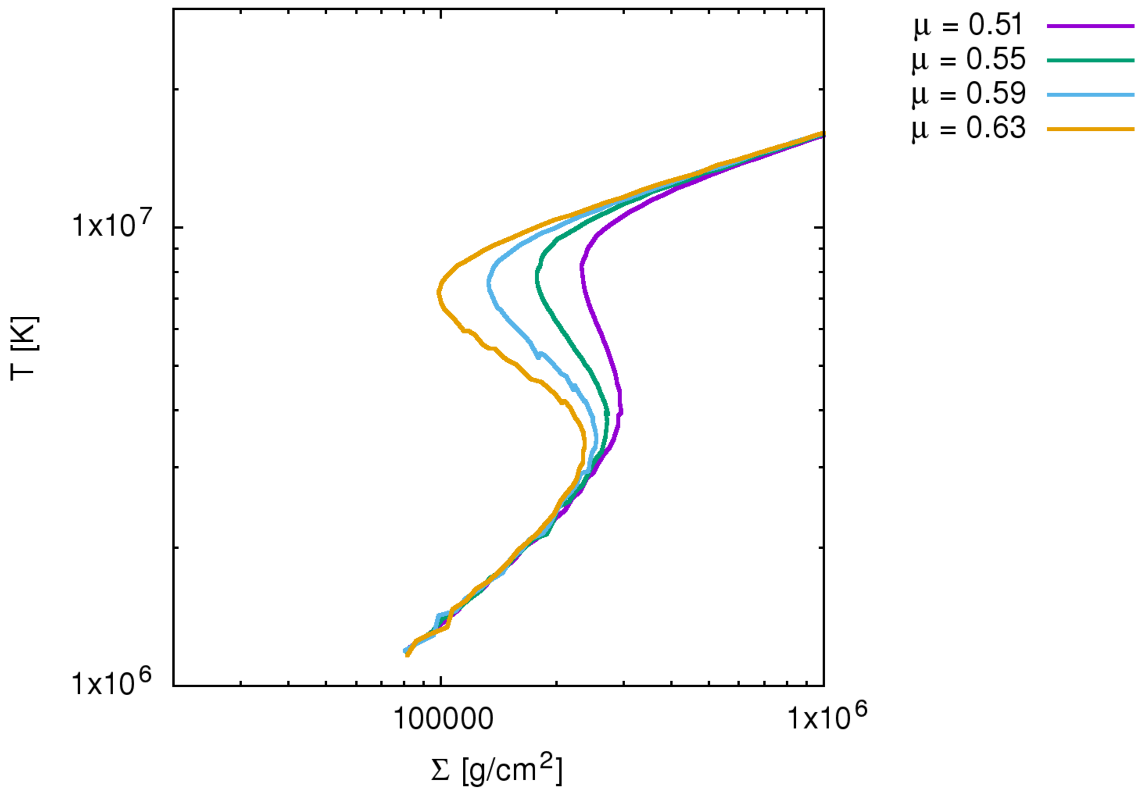

Figure 4.1: Local stability curves for $\mu = 0.51$, $\mu = 0.55$, $\mu = 0.59$ and $\mu = 0.63$. Parameters: $M = 3 \times 10^4 M_{\odot}$, $\alpha = 0.02$, and $\dot{m} = 0.7$. The chosen radius is $R = 7.82 R_{Schw} = 15.74 \frac{GM}{c^2} = 6.88 \times 10^{10}$ cm, corresponding to the inner, hot area of the disk. The curves depend strongly on the μ parameter, and larger μ provides a larger negative derivative range corresponding to the unstable state.

of the instability. However, only the hot, radiation-pressure-dominated area of the disk remains unstable, and for larger radii the S-curve bend moves towards the enormously large, super-Eddington external accretion rates. In effect, for sufficiently large radii, the disk remains stable. The same trend is valid also for stellar mass (microquasars) and supermassive (AGN) black holes (Janiuk & Czerny, 2011).

4.6. Results - time dependent model

This section is focused on the numerical computations of the full time-dependent model. The full computations of the radiation pressure instability models was performed since the stability curves give us only the information about the local disk stability. However, the viscous transport and the radial temperature gradients deform the local disk structure, and the time evolution of the disk at a fixed radius resulting from the global simulations does not necessarily follow the expectations based on local stability analysis.

Figures 4.2 and 4.3 present the stability curves (red) and the global solutions of the dynamical model plotted at the same single radius (green).

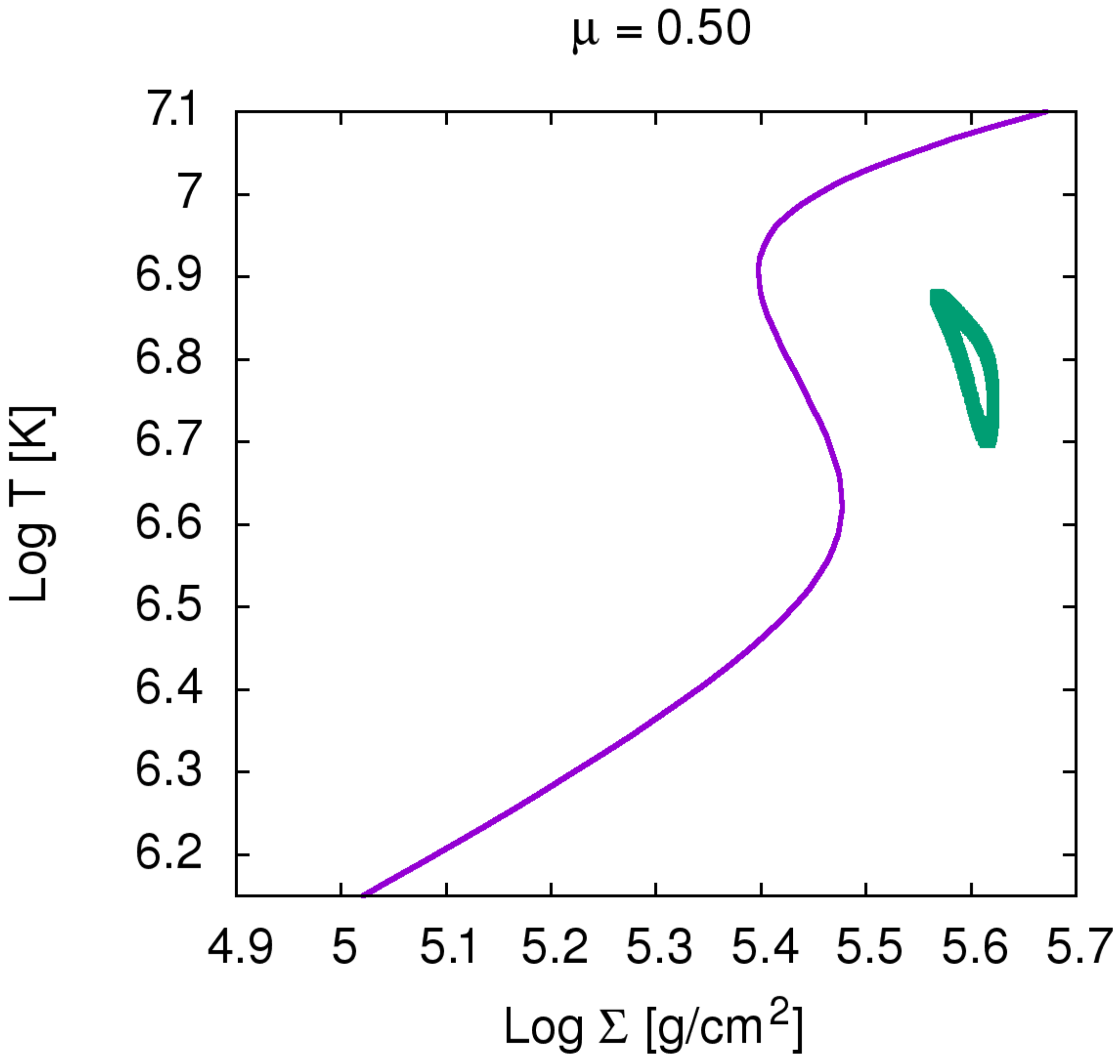

Figure 4.2: T and Σ variability for the model with $\mu = 0.5$ for a typical IMBH accretion disk. The computation shows a weakly developed instability. Parameters: $M = 3 \times 10^4 M_\odot$, $\alpha = 0.02$, and $\dot{m} = 0.25$. The plot is made for the radius $R = 7.82 R_{Schw} = 15.74 \frac{GM}{c^2} = 6.88 \times 10^{10}$ cm. The red curve represents the stationary model and the green dots show local values of the temperature for the time-dependent computation.

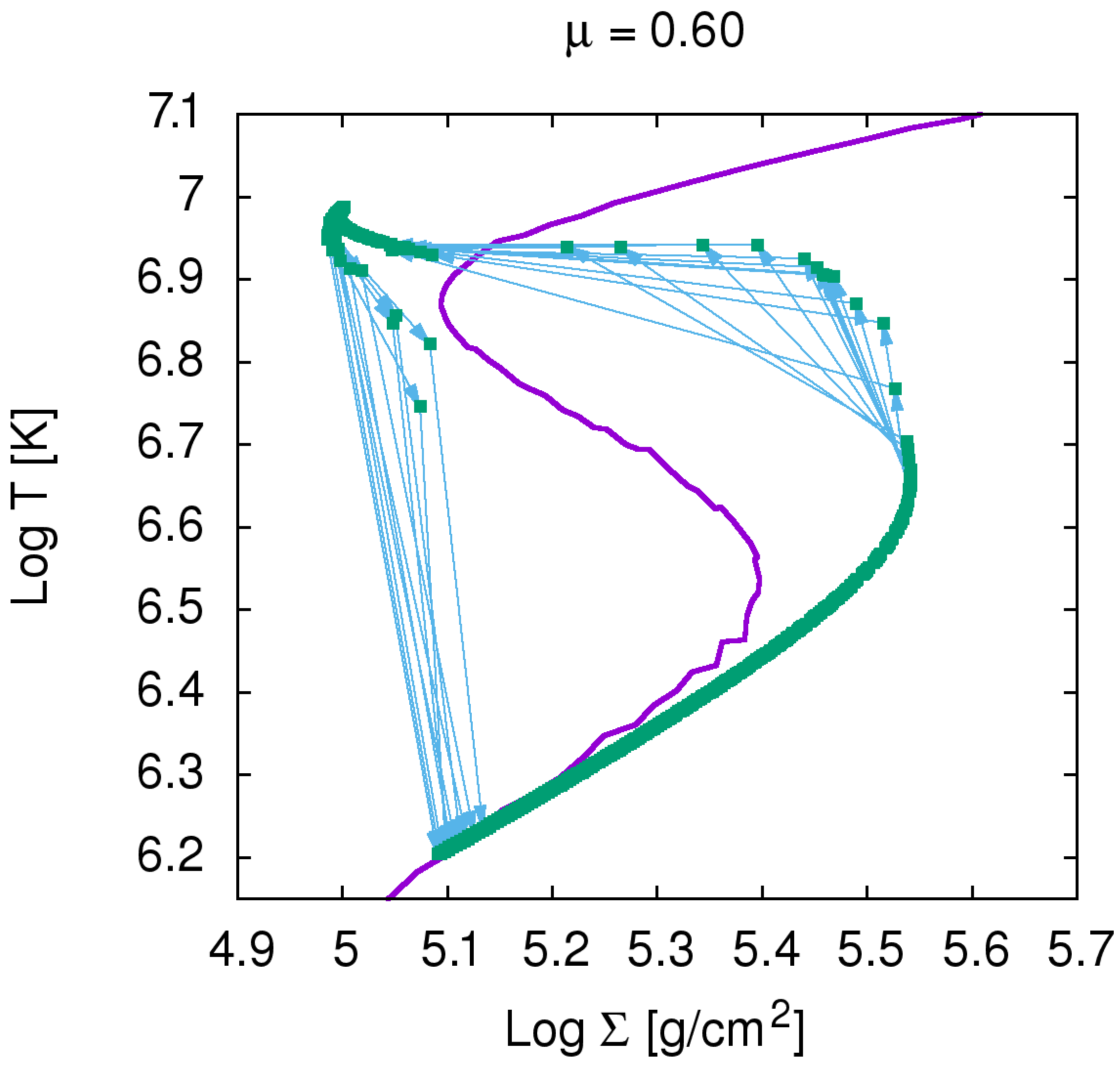

Figure 4.3: T and Σ variability for the model with $\mu = 0.6$ for a typical IMBH accretion disk. The models present a strongly developed instability, leading to huge outbursts. Parameters: $M = 3 \times 10^4 M_\odot$, $\alpha = 0.02$, and $\dot{m} = 0.25$ for the radius $R = 7.82 R_{Schw} = 15.74 \frac{GM}{c^2} = 6.88 \times 10^{10}$cm. The red curve represents the stationary solution and the green dots show local values of the temperature and density in the dynamical model. The points occupy both the upper and lower branches of the S-curve. Green points represent the most common states of the disk, while blue vectors represent directions of the most common rapid changes of local T and Σ.

Stronger bending of the shape of the light curves appears for larger μ resulting in broader development of the instability, visible in the shape of light curves (Figs. 4.4, 4.5). Low values of μ cause the presence of the instability within a small range of radii, therefore the instability is additionally dumped by the stable zones. The time-dependent solution never sets on the stability curve, the covered area in Fig. (4.2) is very small, and the corresponding global light curve shows only small flickering. The growth of the instability for large values of μ results in the dynamical values of T forming two coherent sets (see Figure 4.3), and the solution follows the lower branch of the stability curve. This part of the evolution describes the prolonged period between the outbursts.

To compare the model with data, the model behaviour should be known for the large ranges of parameters. Grid of models was run for typical stellar mass $M = 10M_{\odot}$, for intermediate black hole mass $M = 3 \times 10^4 M_{\odot}$, and for supermassive black holes ($M = 10^8 M_{\odot}$). The viscosity parameter has been adopted at the level of $\alpha = 0.02$ throughout all the computations, and accretion rates ranged between $10^{-1.6}$ and $10^{-0.2}$ in Eddington units. For each mass, the relations between period, amplitude, and duration divided by period has been presented.

According to Czerny et al. (2009), the threshold accretion rate (the sufficient rate for the flares to appear) is at the level of 0.025 for AGNs. For our models, the critical value of accretion rate is at the level of $0.025 - 0.1$ of the Eddington rate. Below, our results are presented through a set of mutual correlations between observable characteristics of the flares, P, A, and Δ (see Table 4.2), and the model parameters, $\dot{m}$, M, and μ.

4.6.1. Light curve shapes

Here the different characteristic modes of the flares are presented. Because of the non-linear dynamics of the system it is expected that the flares will form different patterns of variability, which should be comparable to the observed patterns. For that non-linear system we can distinguish between the flickering behaviour and the strong flares. In Figures 4.4 and 4.5 typical cases of flickering and outburst flares are presented. The difference between the flickering and outburst modes lies not only in their amplitudes; which can be seen in Figure 4.5. The long low luminosity phase, when the inner disk area remains cool, is not present in the flickering case, presented in Fig. 4.4. The latter, corresponds to the temperature and density variations presented in Fig. (4.2), where the surface density of the disk does not change significantly. In contrast, Fig. (4.5) presents the case where the surface density changes significantly and Σ needs a long time to grow to the value where rapid heating is possible. In the case of flickering we can distinguish two phases of the cycle: (i) heating, when the temperature in the inner regions of the disk is growing rapidly, and (ii) advective, when the inner annuli cool down significantly, and are then extinguished when the disk is sufficiently cool. Now, after a strong decrease of advection, the heating phase repeats again. In the case of the burst, the phases (i) and (ii) are much more developed and advection is able to achieve instantaneous thermal equilibrium of the disk, in contradiction to flickering, where the disk is always unstable. The instantaneous equilibrium leads to the third phase (iii), diffusive, when the surface density in the inner annuli of the disk is growing up to the moment when the stability curve has a negative slope, and the cooling rate, Q_{-}, is significantly smaller in comparison to the heating rate, Q_{+}. Then, the phase of heating repeats.

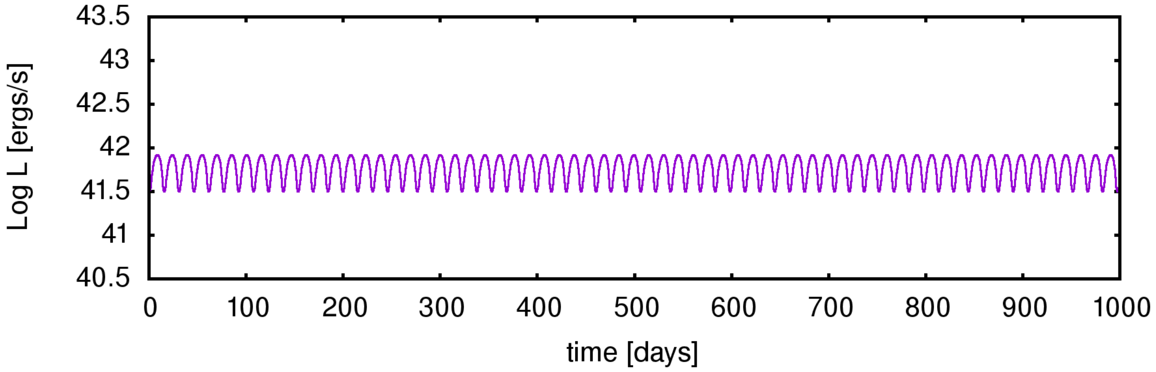

Figure 4.4: Typical flickering light curve for intermediate mass black hole and smaller μ ($M = 3 \times 10^4 M_{\odot}$, $\mu = 0.5$, $\dot{m} = 0.25$)

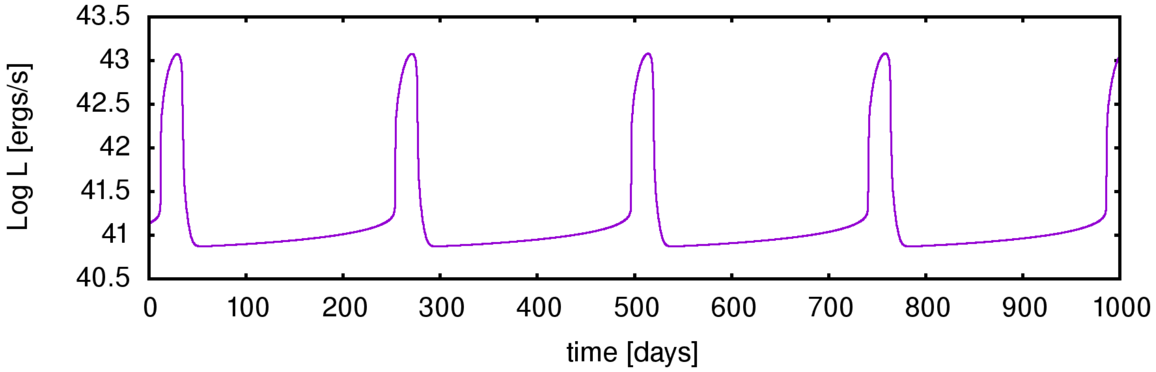

Figure 4.5: Typical outburst light curve for intermediate mass black hole and larger μ ($M = 3 \times 10^4 M_{\odot}$, $\mu = 0.6$, $\dot{m} = 0.25$).

4.6.2. Amplitude maps

Figure 4.6 shows dependencies between the accretion rate, μ coefficient, and flare amplitude. The black area corresponds to cases of stable solutions without periodic flares. The violet area corresponds to a small flickering, and red and yellow areas correspond to bright outbursts. Since for a given accretion rate and μ the AGN disks are much more radiation-pressure-dominated (Janiuk & Czerny, 2011), the critical values of the accretion rates in Eddington units are the lowest for AGNs. Thus, the stabilising influence of a magnetic field is more pronounced for the microquasars, than for AGNs. Our results include different variability patterns. As shown in Figure 4.6, for a given set of μ and accretion rate, the relative amplitude varies by many orders of magnitude (from small flares, changing the luminosity by only a few percent, up to the large outbursts with amplitudes of ~ 200 for microquasars, ~ 1000 for intermediate black holes, and ~ 2000 for AGN). The flare amplitude grows with accretion rate and with μ. To preserve the average luminosity on sub-Eddington level, also the light curve shape should change with at least one of these parameters. Let Δ be the flare duration to period ratio, as defined in Table 4.2. To preserve the average luminosity L, the energy emitted during the flare plus energy emitted during quiescence (between the flares) should be lower than the energy emitted during one period. Since the radiation pressure instability reaches only the inner parts of the disk, the outer stable parts of the disk radiate during the entire cycle, maintaining the luminosity at the level of $L_{\rm min}$. This level can be computed from Eq. (2.18) since the outer border of the instability zone is known.

4.6.3. Amplitude and period

In Figure 4.7, the dependence between period and amplitude for the microquasars, intermediate mass black holes and AGN, is presented respectively. In general, the amplitude grows with the period P, μ, and accretion rate $\dot{m}$. Figure 4.7 was made for the three grids of these models which result in significant limit-cycle oscillations (i.e. $L_{\rm max}/L_{\rm min} > 1.2$). In these computations regular and rectangular grids was used. For $M = 10 M_{\odot}$ and $M = 3 \times 10^4 M_{\odot}$, $\alpha = 0.02$ (as explained in Sect. 3.1.1), and the viscosity parameter ranges were $\mu = \{0.44, 0.46, ..., 0.80\}$ and $\log \dot{m} = \{-1.6, ... - 0.4, -0.2\}$. For $M = 10^8 M_{\odot}$ we chose a different range and sampling, $\mu = \{0.44, 0.45, ..., 0.56\}$, but the same range of $\dot{m}$. The range of $\dot{m}$ was adjusted to cover all the values for which the instability appears. The values of μ were chosen to consist of supercritical ones, according to Eq. (4.12) (i.e. larger than $\mu_{\rm cr} = 3/7$). The upper cut-off of μ (i.e. 0.8 for XRBs and IMBHs, and 0.56 for AGNs) was chosen because of computational complexity that arises for larger μ. Nevertheless, the observed properties of the sources (see, e.g. Table 4.5 in Section 4.8) suggest that in any case the values of μ are limited.

The results shown by points in Fig. (4.7) can be fitted with the following formula:

$$\log P \text{ [sec]} \approx 0.83 \log \frac{L_{\rm max}}{L_{\rm min}} + 1.15 \log M + 0.40. \tag{4.21}$$

Here P is the period in seconds and M is the mass in Solar masses. The above general relation gains the following forms, being applicable for the sources with different black hole mass scales:

$$\log P_{\rm MICR} \text{ [sec]} \approx 0.83 \log \frac{L_{\rm max}}{L_{\rm min}} + 1.15 \log \frac{M}{10 M_{\odot}} + 1.55, \tag{4.22}$$

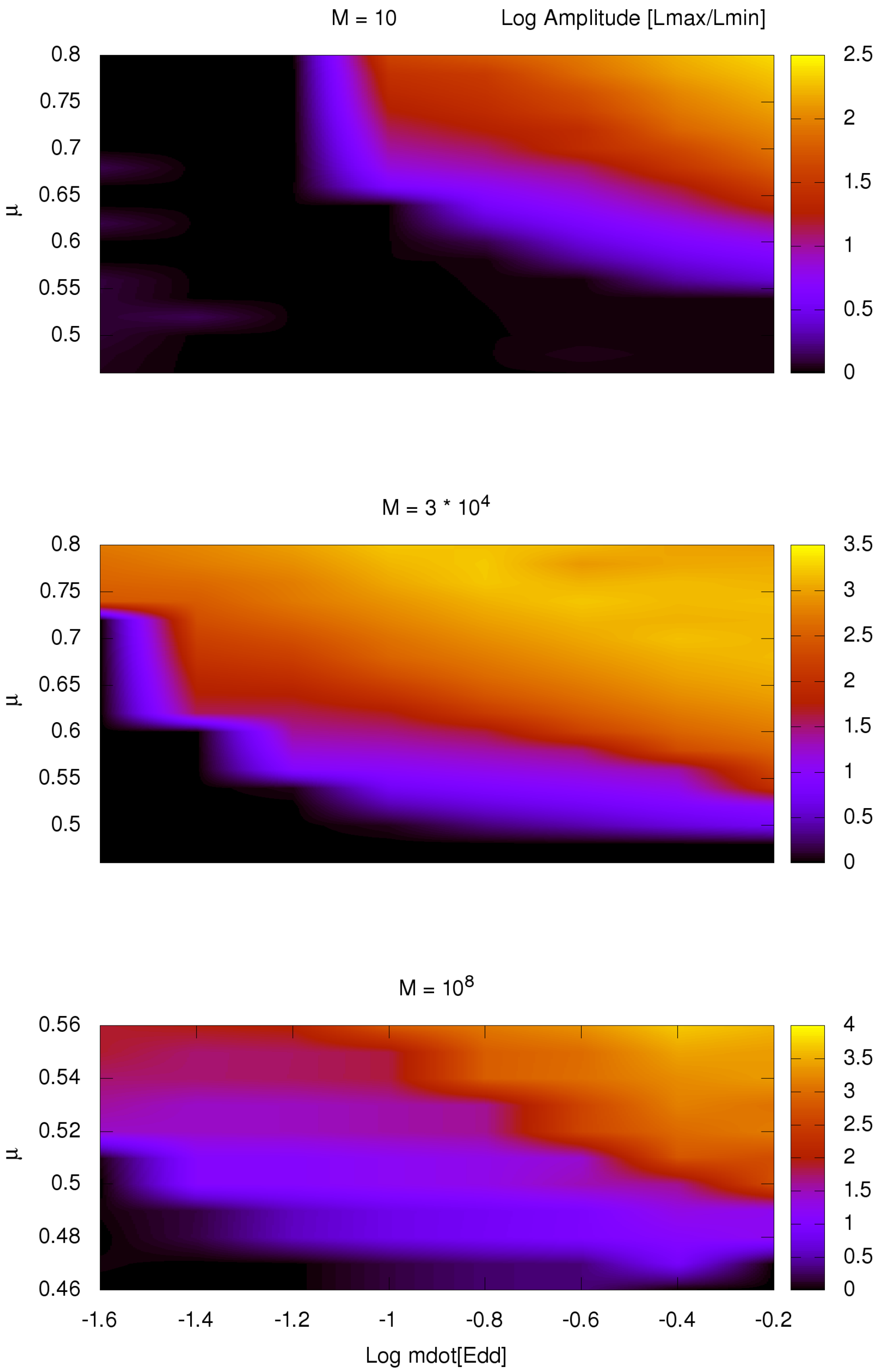

Figure 4.6: Amplitude map for different values of accretion rates and μ for the accretion disk around a stellar-mass black hole ($M = 10M_\odot$, **upper panel**), around an intermediate-mass black hole ($M = 3 \times 10^4 M_\odot$, **middle panel**), and around a supermassive black hole ($M = 10^8 M_\odot$, **bottom panel**). Black regions represent no flares and a lack of instability.

for the microquasars (see fit on Fig. 4.7), then

$$\log P_{\mathrm{IMBH}}\ [\mathrm{days}] \approx 0.83 \log \frac{L_{\max}}{L_{\min}} + 1.15 \log \frac{M}{3 \times 10^4 M_\odot} + 0.53 \tag{4.23}$$

for intermediate mass black holes (see fit on Fig. 4.7), and finally

$$\log P_{\mathrm{AGN}}\ [\mathrm{years}] \approx 0.83 \log \frac{L_{\max}}{L_{\min}} + 1.15 \log \frac{M}{10^8 M_\odot} + 2.1 \tag{4.24}$$

for active galaxies (see fit on Fig. 4.7).

From the formula (4.21) the values of masses of objects can be estimated, if the values of P and A are known. The period-amplitude dependence is universal, and, in the coarse approximation, does not depend on μ. The positive correlation between period and amplitude indicates that those observables originate in one nonlinear process, operating on a single timescale. Although the variability patterns can vary for different accretion rates, for a given mass, the period and amplitude are strongly correlated and can describe the range of instability development. It can, in general, be adjusted by the specific model parameters, but the basic disk variability pattern is universal in that picture.

4.6.4. Amplitude and width

In Figure 4.8 the relation between the flare amplitude and its width is presented. Both values are dimensionless and show similar reciprocal behaviour for the black hole accretion disks flares across many orders of magnitude. The value of Δ can help us to distinguish between different states of the source. It should also be noted that Δ depends on the amplitude of the outburst only for small amplitudes, while for the larger ones, Δ remains approximately constant. The most convenient classification is to introduce the 'flickering' mode (A < 50), which corresponds to the large ratio of the flare duration to its period ($\Delta > 0.15$), and the 'outburst' mode (A > 50), which corresponds to the small flare duration to period ratio ($\Delta < 0.15$). The latter appears for high μ and $\dot{m}$, while the former occurs for low μ and $\dot{m}$.

4.6.5. Width, period, and μ

In Fig. (4.9) the relation between the period of flares and width of flares is presented. The timescale of flare scales is approximately inversely proportional to the mass. According to Fig. (4.9), the flare duration to period rate Δ only weakly depends on the value of accretion rate. The dependence on μ is more significant for all the probed masses. Thus, the flare shape is determined mostly by the microphysics of the turbulent flow and its magnetisation, which is hidden in the μ parameter, and not by the amount of inflowing matter expressed by the value of accretion rate $\dot{m}$. In Figure 4.10, the result from Fig. (4.9) are presented along with linear log fits connecting the values of Δ, μ, and the black hole mass M, which can be described by the formula:

$$-\log \Delta = (1.9 + 1.2 \log M)(\mu - 3/7). \tag{4.25}$$

From Eq. (4.25), it can be concluded that the flare shape depends predominantly on the disk magnetisation. Equation (4.25) enables to estimate the behaviour of the sources even for the values of μ higher than those used in Figure 7. As a result, larger μ correspond in general to narrower flares. This effect is even more pronounced for larger black hole masses. Therefore, the outburst flares are more likely to occur for larger values of μ.

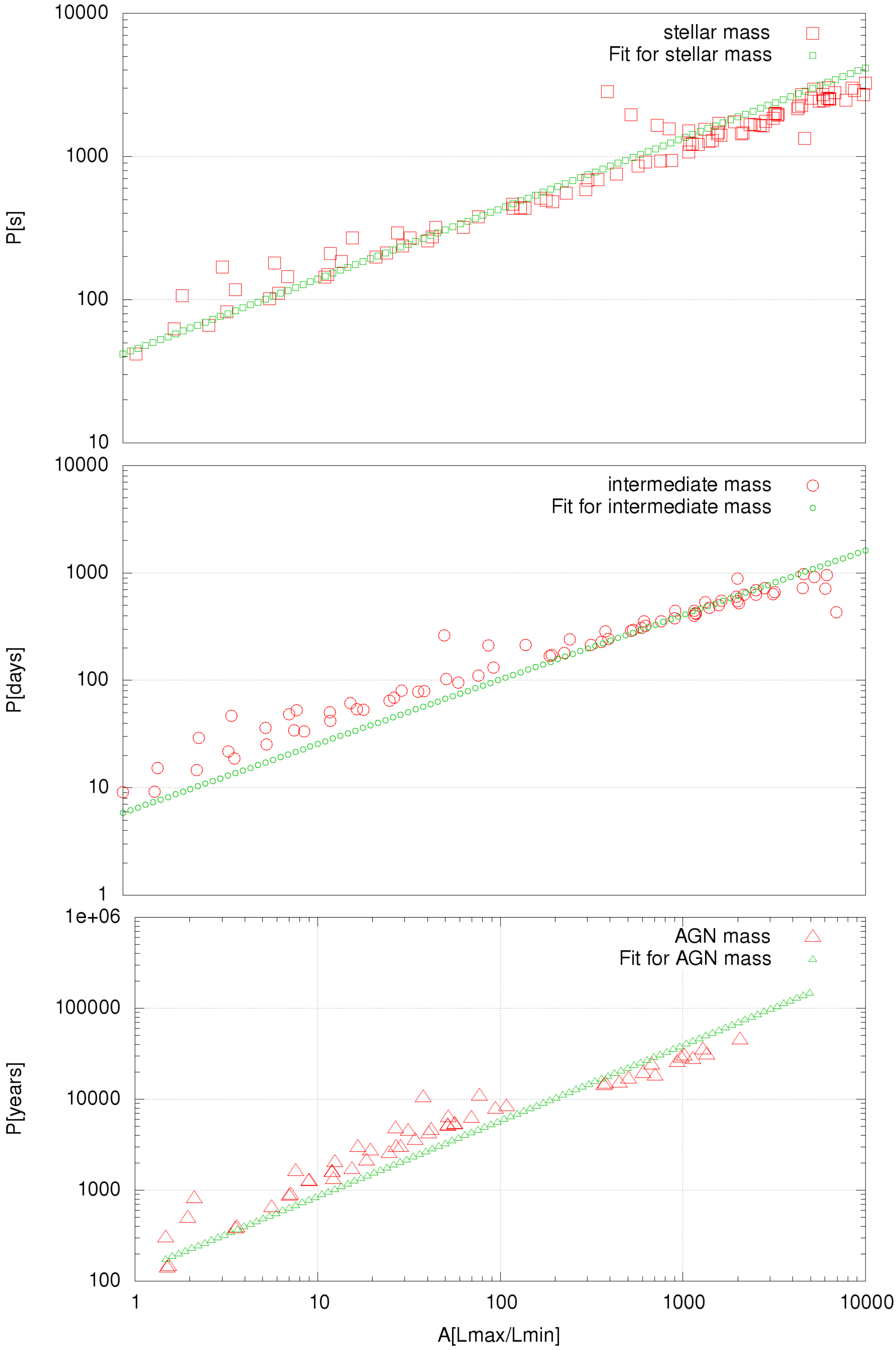

Figure 4.7: Dependence between period and amplitude of flares for a stellar-mass black hole ($M = 10M_\odot$, **upper panel**), an intermediate-mass black hole ($M = 3 \times 10^4 M_\odot$, **middle panel**), and a supermassive black hole ($M = 10^8 M_\odot$, **bottom panel**). Computations were made for a range of μ but values for a different μ lie predominantly along the main correlation trend resulting in a very low scatter.

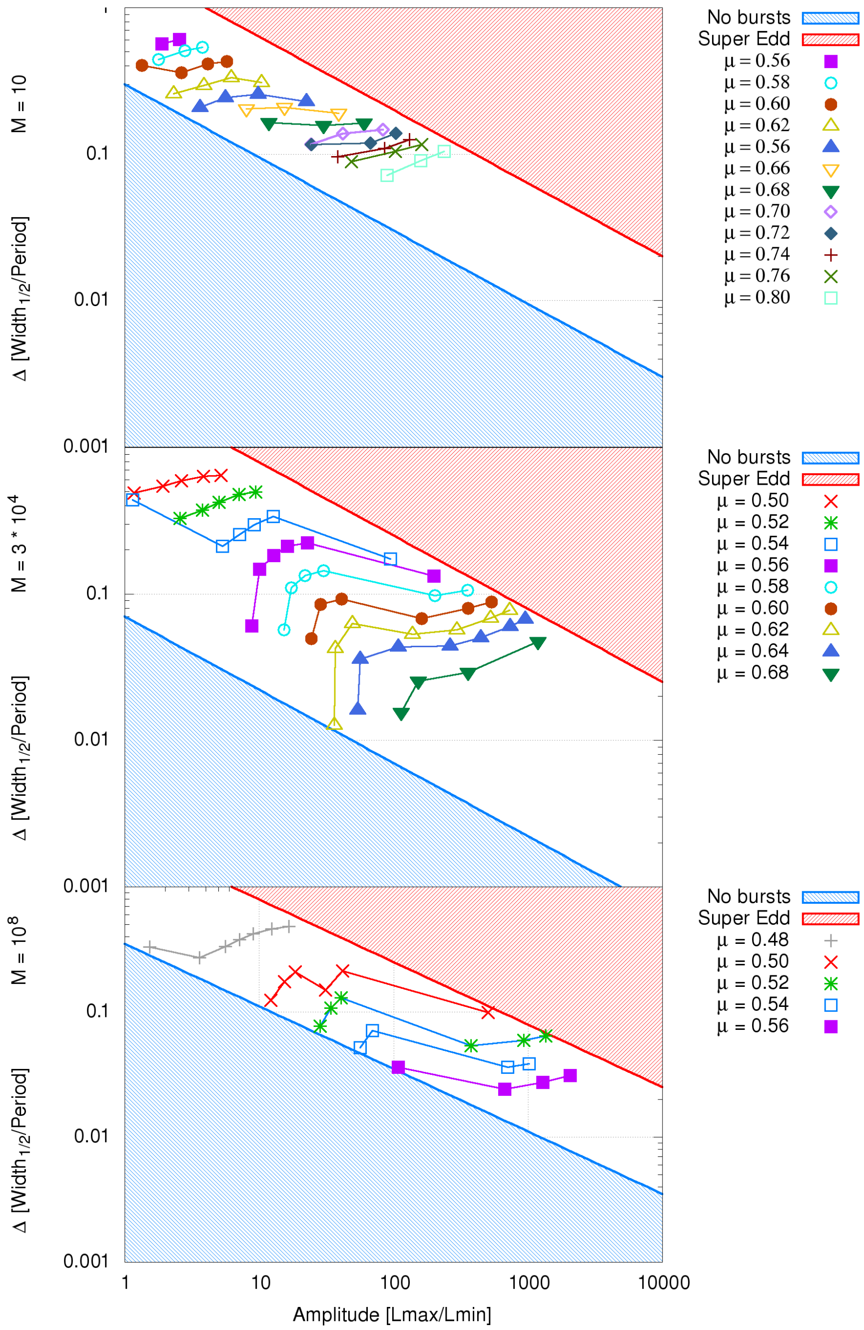

Figure 4.8: Dependence between the amplitude and width of flares for a stellar-mass black hole ($M = 10 M_{\odot}$, **upper panel**), an intermediate-mass black hole ($M = 3 \times 10^4 M_{\odot}$, **middle panel**), and a supermassive black hole ($M = 10^8 M_{\odot}$, **lower panel**). The ranges of μ are given for each figure. The colour lines represent isolines for different μ. The scatter is now larger than in Fig. (4.7).

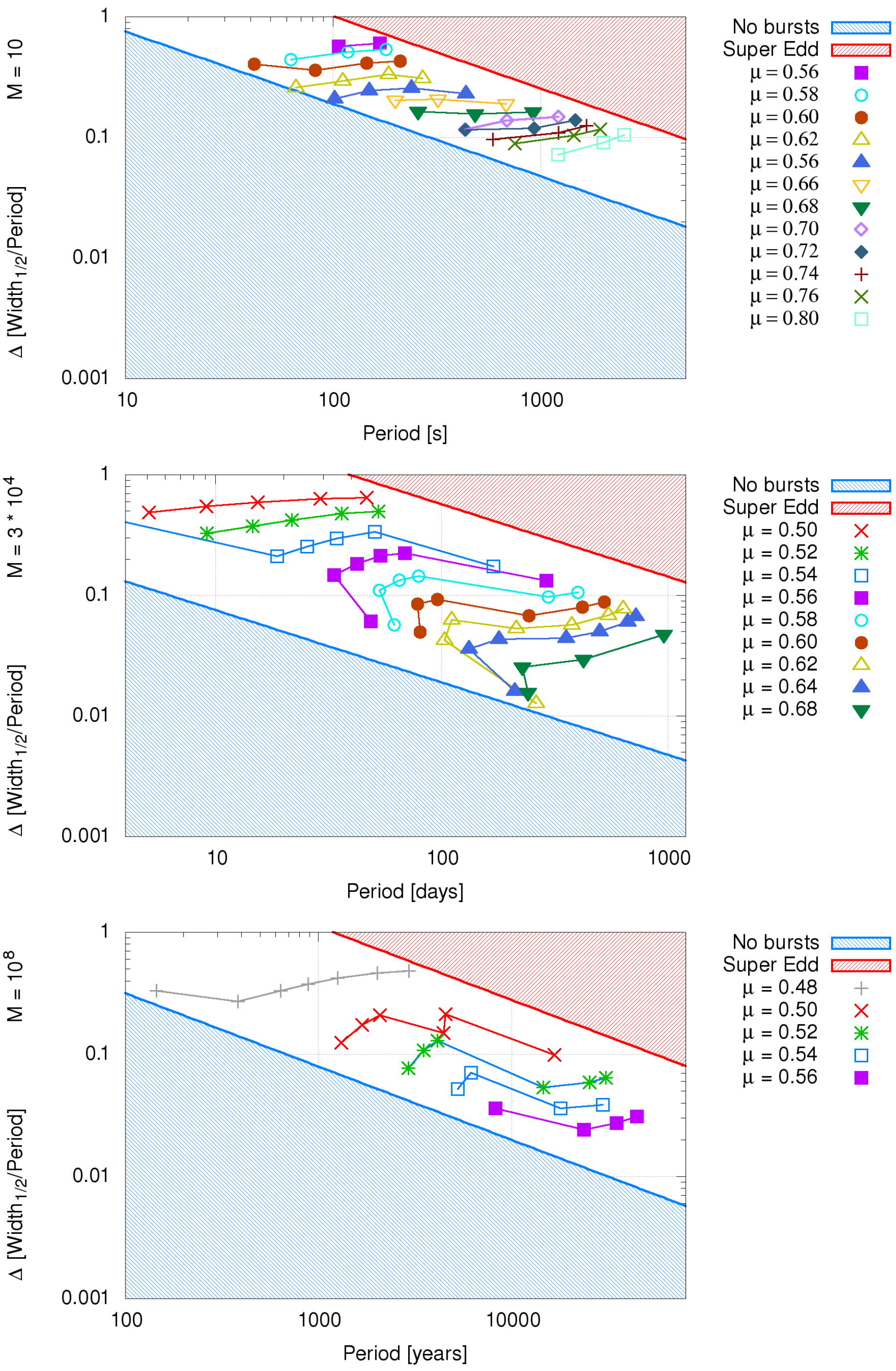

Figure 4.9: **Upper panel**: Dependence between period and width of flares for a stellar-mass black hole ($M = 10 M_{\odot}$). The graph was prepared for a range of $\mu \in [0.44 : 0.8]$. **Middle panel**: Dependence between period and width of flares for an intermediate-mass black hole ($M = 3 \times 10^4 M_{\odot}$). The graph was prepared for a range of $\mu \in [0.44 : 0.8]$. **Bottom panel**: dependence between period and width of flares for a supermassive black hole ($M = 10^8 M_{\odot}$). The graph was prepared for a range of $\mu \in [0.44 : 0.56]$. The colored lines represent isolines for different μ.

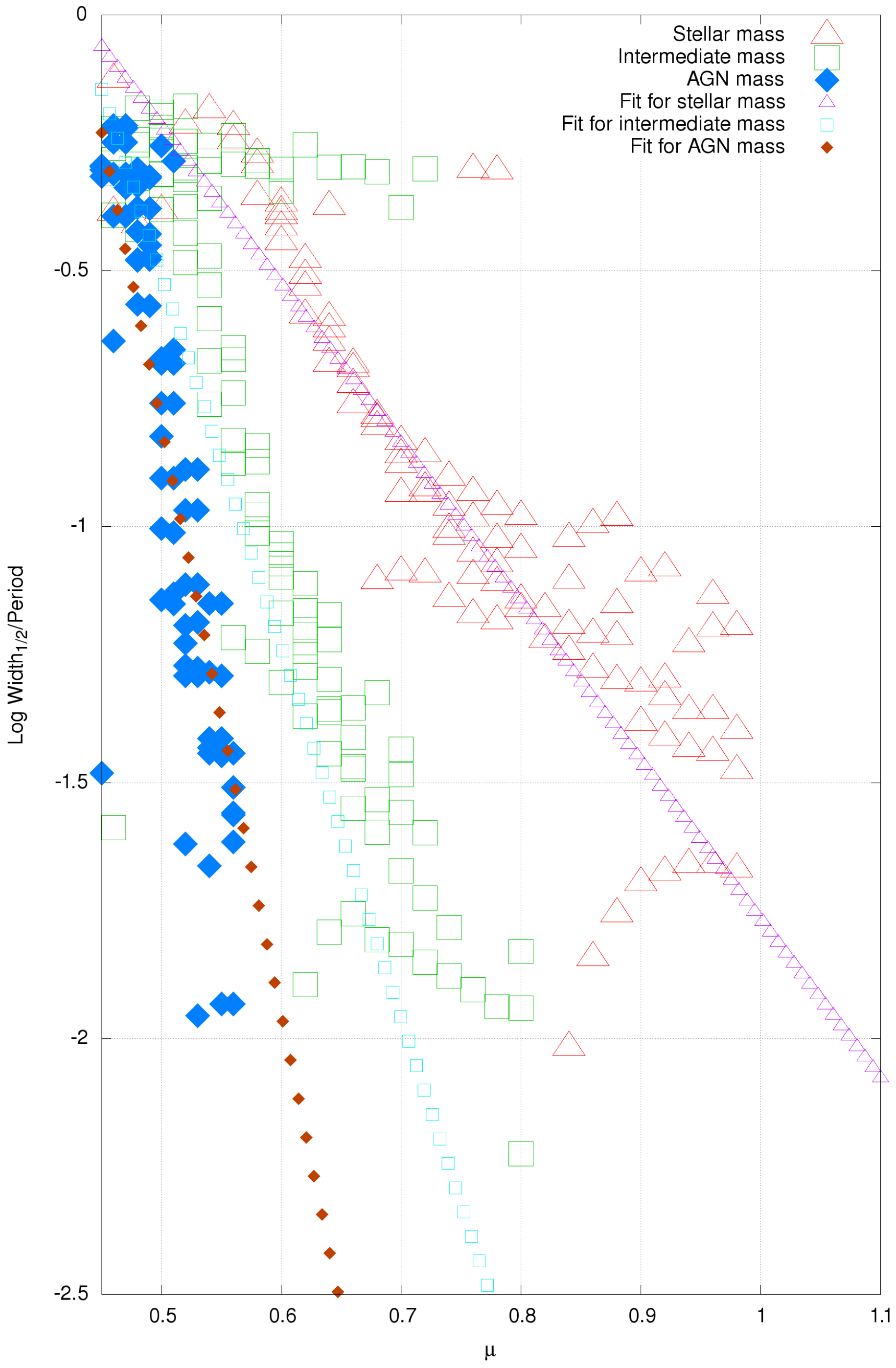

Figure 4.10: Dependence between width, μ parameter and mass. One triangle represents one model. Triangles represent the model for the stellar-mass black hole accretion disks ($M = 10 M_{\odot}$), squares represent the model for the intermediate mass black hole accretion disks ($M = 3 \times 10^4 M_{\odot}$) and diamonds represent the model for the supermassive black hole accretion disks ($M = 3 \times 10^8 M_{\odot}$). Lines consisting of corresponding shapes (diamonds, squares, triangles) represent fits for each mass.

4.6.6. Amplitude and accretion rate

In Figure 4.11 the dependence between relative amplitudes and accretion rates $\dot{m}$ for the stellar mass, intermediate mass, and supermassive black holes is shown respectively. The dependence is monotonnic for any of μ and mass. Because of the nonlinearity of evolution equations with respect to $\dot{m}$, any simple scaling relation between $\dot{m}$ and amplitudes nor periods can not be presented.

4.6.7. Limitations for the outburst amplitudes and periods

In Figures 4.8 and 4.9 the dark areas in top panels mark our numerical estimations for the possibly forbidden zones in the case of microquasar accretion disks. From those figures, we extract following fitting formulae:

$$0.3 \times A^{-0.5} < \Delta < 2A^{-0.5} \tag{4.26}$$

$$3 \times (P\ [s])^{-0.6} < \Delta < 50 \times 16P\ [s]^{-0.6}. \tag{4.27}$$

Eqs. (4.26) and (4.27) result in the following estimation for P and A

$$1.96 \times A^{0.83} < P\ [s] < 630 \times A^{0.83}. \tag{4.28}$$

In Figures 4.8 and 4.9, middle panels show the estimated range of the possibly forbidden zones in the case of the accretion disks around the intermediate-mass black holes. From those figures:

$$0.07 \times A^{-0.5} < \Delta < 2.5 \times A^{-0.5} \tag{4.29}$$

$$0.3(P\ [\text{days}])^{-0.6} < \Delta < 9 \times P[\text{days}]^{-0.6}. \tag{4.30}$$

Eqs. (4.29) and (4.30) result in the following estimation for P and A:

$$0.0021 \times A^{0.83} < P < 7500 \times A^{0.83}. \tag{4.31}$$

Finally, the dark shaded areas mark our estimations for the possibly forbidden zones for the case of supermassive black hole accretion disks (bottom panels). We get the following formulae from those figures:

$$5 \times A^{-0.5} < \Delta < 70 \times A^{-0.5} \tag{4.32}$$

$$0.35 \times (P\ [\text{years}])^{-0.6} < \Delta < 2.5 \times (P\ [\text{years}])^{-0.6}. \tag{4.33}$$

Eqs. (4.32) and (4.33) result in the following estimation for P and A:

$$4.67 \times A^{0.83} < P < 16.6 \times A^{0.83}. \tag{4.34}$$

4.7. Disk flare estimations

We derive the general estimations for the oscillation period P, its amplitude A and relative duration Δ thanks to computing a large grid of models. It has been achieved despite the uncertainty of the scaling parameter μ.

The results are summarized in Table 4.3.

We compare the allowed values of duration to period ratios (columns 3 and 4), periods (columns 5 and 6), and flare durations (columns 7 and 8). Three values of relative amplitude for each source was represent possible limitations for periods and duration times. The amplitude $A = 2$ represents faint flares, like those in the microquasar IGR J17091 (See Chapter 3). The amplitude $A = 10$ corresponds to a more developed

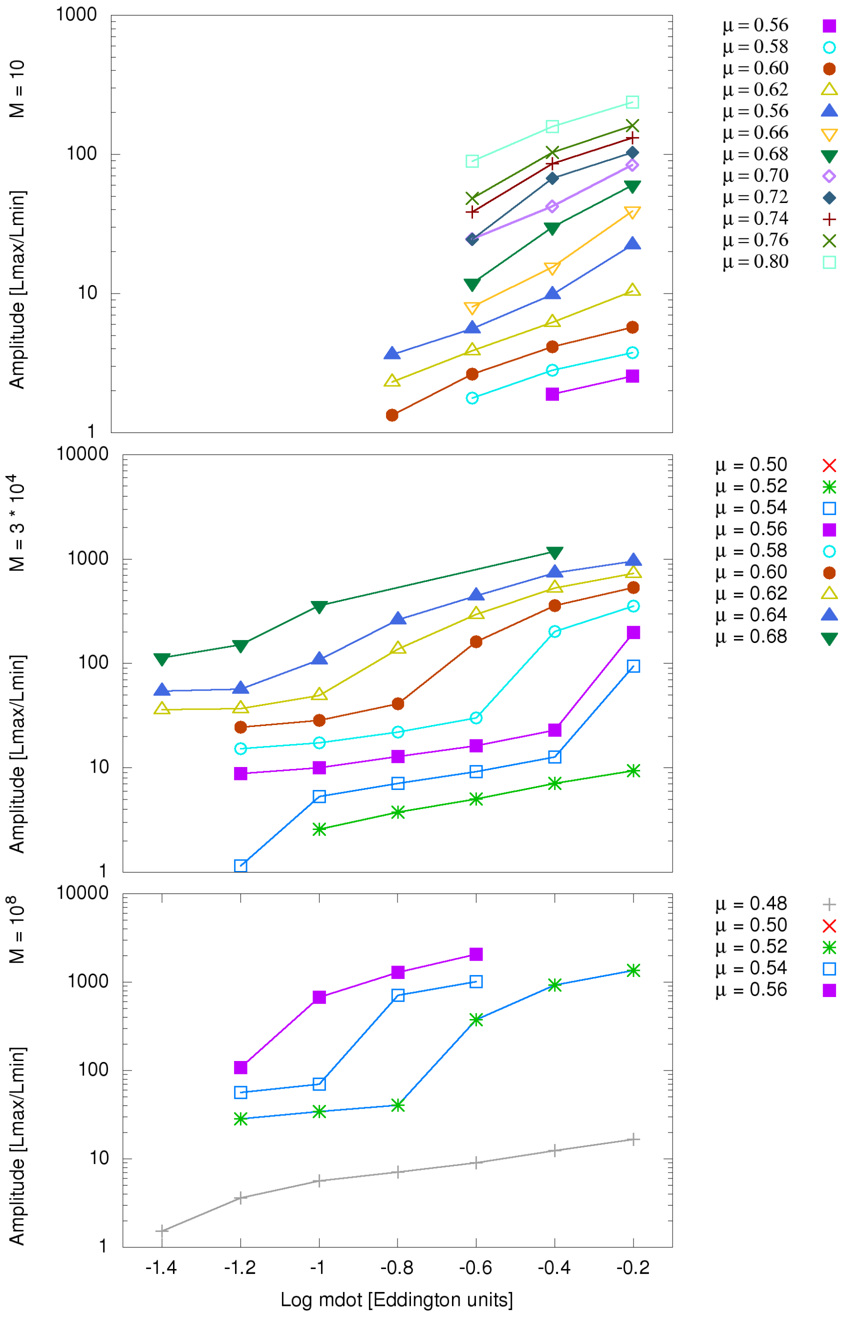

Figure 4.11:
Upper panel: Dependence between amplitude and accretion rate for a stellar-mass black hole ($M = 10M_{\odot}$).
Middle panel: Dependence between amplitude and accretion rate for an intermediate-mass black hole ($M = 3 \times 10^4 M_{\odot}$).
Bottom panel: Dependence between amplitude and accretion rate for stellar-mass black hole ($M = 10^8 M_{\odot}$). The graph was prepared for a range of μ. We can see simple unambiguous dependence for different μ-models.

Flare characteristic quantities for microquasars:			
A	Δ	P [s]	$P\Delta$ [s]
*2	0.212 - 1	3.48 - 1120	0.739 - 1120
**10	0.0949 - 0.632	13.3 - 4260	1.26 - 2690
***100	0.03 - 0.2	89.6 - 28800	2.69 - 5760
Flare characteristic quantities for IMBHs:			
A	Δ	P [days]	$P\Delta$ [days]
*2	0.0494 - 1	0.533 - 5330	0.00264 - 5330
**10	0.0221 - 0.79	0.203 - 20282	0.00449 - 16030
***100	0.007 - 0.25	1.37 - 13700	0.0960 - 34300
Flare characteristic quantities for AGNs:			
A	Δ	P [years]	$P\Delta$ [years]
*2	0.248 - 1	24.9 - 12100	6.16 - 21100
**10	0.111 - 0.796	94.7 - 46500	10.5 - 36300
***100	0.0035- 0.25	640 - 311000	22.4 - 77700

Table 4.3: Range of duration values for three kinds of source. The values for microquasars are expressed in seconds, values for IMBHs in days and values for AGNs in years. Flare regimes * - small flicker, ** - intermediate, *** - burst

Source	Mass [$M_\odot$]	*$P\Delta_{0.1}$	**$P\Delta_1$
Microquasar	10	33s	595 s
IMBH	3×10^4 days	8.59	153 days
AGN	10^8	596years	10603 years

Table 4.4: Mean flare duration values for three kinds of source. The values are taken from Eq. (4.42). * - duration for $L = 0.1 L_{\rm Edd}$, ** - duration for $L = L_{\rm Edd}$

instability case, like that in the ρ states of object GRS1915 (Belloni et al., 2000). The amplitude $A = 100$ is connected with the huge bursts, as in HLX-1 (see next Chapter). The timescales presented in the Tables are on the order of minutes for the microquasars, of months for the ULXs, and of millenia for the AGN, which corresponds to their viscous timescale. The period is strongly dependent on the amplitude and can change by several orders of magnitude for each mass. The estimations given here were made for the values of μ which are sufficient for the outbursts, but do not determine exactly the value of this parameter. Figure 4.14 (see next Section) presents a universal dependence between duration times and bolometric luminosities for the X-ray sources of different scales (microquasars with $M = 10 M_\odot$, IMBHs with $M = 3 \times 10^4 M_\odot$, and AGN with $M = 10^8 M_\odot$). Exact duration values from the fit presented in Eq. (4.42) are shown in Table 4.4. For microquasars, the values included in Table 4.3 correspond to the typical values for small and intermediate flares, the same for the case of IMBHs. In case of AGN, the appearance of big flares is necessary to verify our model with the observational data presented in the Figure 4.14.

4.8. Summary and discussion

In this Chapter, the accretion disk instability induced by the dominant radiation pressure has been studied along with the use of the generalised prescription for the stress

Source	**ID**	**P**	**A**	Δ	$C_{M\alpha}$	μ^*
IGR	ν_I	45s	2.5	0.15	6.38	0.717
IGR	ρ_{IA}	30s	3.5	0.3	3.52	0.634
IGR	ρ_{IB}	30s	4	0.4	3.198	0.589
GRS	ν_G	90s	4	0.1	8.31	0.763
GRS	ρ_{GA}	45s	5	0.25	3.87	0.661
GRS	ρ_{GB}	40s	4.5	0.4	3.77	0.583
HLX	-	400d	2.5	0.14	1.88×10^5	0.534
AGN$*$	-	10^5y	100	0.1	1.6×10^8	0.515

Table 4.5: Characteristic quantities of the RXTE PCA light curves for Galactic sources presented in Altamirano et al. (2011a) (columns $3, 4, 5$) supplemented with HLX and AGNs, and estimations of the $mass - \alpha$ relations and magnetisation of sources (columns $6, 7$). **Notation:** IGR = IGR J17091, GRS = GRS 1915, HLX = HLX-1, AGN - typical value for the sample of AGNs presented in (Czerny et al., 2009). The OBSIDs of the light curves are as follows: $\nu_I = 96420-01-05-00$ (ν state), $\rho_{IA} = 96420-01-06-00$ (ρ state), $\rho_{IB} = 96420-01-07-00$($\rho$ state) ,$\nu_G = 10408-01-40-00$ (ν state) , $\rho_{GA} = 20402-01-34-00$ (ν state) and $\rho_{GB} = 93791-01-02-00$ (ρ state), * - Values for a typical AGN. $C_{M\alpha}$ is the mass-alpha parameter defined in Eq. (4.40)

tensor. Power-law dependence has been adopted along with an index μ, to describe the contribution of the radiation pressure to the heat production. In other words, the strength of the radiation pressure instability deepens with growing μ. We computed a large grid of time-dependent models of accretion disks, parameterised by the black hole mass, and mass accretion rate. We used the values of these parameters, which are characteristic for the microquasars, intermediate black holes, or AGN. One of our key findings is that this model can be directly applicable for determination of the black hole mass and accretion rate values. We also found that the critical accretion rate, for which the thermal instability appears, decreases with growing μ (see Figure 4.6). Also, the amplitudes of the flares of accretion disks in AGN are larger than the amplitudes of flares in microquasars and in IMBHs. The flare period grows monotonously with its amplitude, for any value of mass (see Figure 4.7). The outburst width remains in a well-defined relationship with its amplitude (see Figure 4.8). We also found that there is a significant negative correlation between μ and the ratio of the flare duration to the variability period, Δ. On the other hand, the dependence between the outburst amplitude A and the mass accretion rate $\dot{m}$ is non-linear and complicated. Our results present different variability modes (Figures 4.4 and 4.5). The flickering mode is presented in Fig. 4.4. In this mode the relative amplitude is small, and flares repeat after one another. In the burst mode the amplitude is large, and the maximum luminosity can be hundreds of times greater than minimum. An exemplary light curve is shown in Fig. (4.5). In this mode long separation between the flares can be observed (i.e. an extended low luminosity state), dominated by the diffusive phenomena. A slow rise of the luminosity is the characteristic property of the disk instability model.

4.8.1. Mass - α relation

Since the thermal and viscous timescales strongly depend on α, which has only ad-hoc character and does not constitute any fundamental physical quantity, α is the parameter describing development of the MHD turbulence in the accretion disk. Thus α should, to some extent, vary depending on the source and its state; for example, the value of α for the AGN accretion disks can differ from its value for the disks in X-ray binaries. In Fig. (4.12) different light curve shapes for six different values of α are presented. In Fig. 4.13 the dependence of the light curve observables on α is presented. The formula describing fits in Fig. (4.13) is as follows:

$$\log O_X = b_X \log\alpha + c_X, \tag{4.35}$$

where $O_X = A$, P[seconds], or Δ. The coefficients are as follows $b_A = 2.25 \pm 0.11$, $c_A = 0.85 \pm 0.05$, $b_P = -0.3 \pm 0.05$, $c_P = 1.85 \pm 0.07$, $b_\Delta = -0.29 \pm 0.03$, $c_\Delta = -0.87 \pm 0.05$. The grids of models deliver some information about the correlation between the observed light curve features and the model parameters. From the Eq. (4.21) we determine the mass of an object directly from its light curve:

$$M[M_\odot] = 0.45 P[s]^{0.87} A^{-0.72}. \tag{4.36}$$

The $\Delta - \mu - M$ dependence from Fig. (4.10) and Eq. (4.25), combined with Eq. (4.36) gives us the exact estimation on μ

$$\mu = 3/7 + \frac{-\log\Delta}{1.49 + 1.04\log P - 0.864\log A}. \tag{4.37}$$

According to Eqs. (4.36) and (4.37) and Eq. (4.35) we obtain the following:

$$M[M_\odot] = 0.45 P[s]^{0.87} A^{-0.72} (\frac{\alpha}{0.02})^{-1.88}, \tag{4.38}$$

$$\mu = 3/7 + \frac{-\log\Delta + 0.87\log(\frac{\alpha}{0.02})}{1.49 + 1.04\log P - 0.864\log A}. \tag{4.39}$$

For the purpose of this work, we made an assumption that $\alpha = 0.02$ is constant, however, it can not be true in any kind of the accretion disk source, so in result our method leads to the significant degeneracy between the mass and alpha. So on, we can define the exactly determinable mass-alpha parameter $C_{M\alpha}$

$$C_{M\alpha} = \frac{M}{M_\odot} (\frac{\alpha}{0.02})^{1.88}. \tag{4.40}$$

4.8.2. Radiation pressure instability in microquasars

Quantitatively, our numerical computations, as well as the fitting formula (4.21), give the adequate description of the characteristic 'heartbeat' oscillations of the two known microquasars: GRS 1915+105, and IGR 17091-324. Their profiles resemble those observed in the so-called ρ state of these sources, as found, for example, on 27th May, 1997 (Pahari et al., 2014). For the microquasar IGR J17091, the period of the observed variability is less than 50s, as observed in the most regular heartbeat cases, that is, in the ρ and ν states (Altamirano et al., 2011a). The ν class is the second most regular variability class after ρ, much more regular than any of the other ten classes described in Belloni et al. (2000) (α, β,γ, δ, θ, κ, λ,μ, ϕ, χ). The ρ state is sometimes described as extremely regular (Belloni et al., 2000), with a period of about $60 - 120$ seconds for the case of GRS1915. The class ν includes typical Quasi-Periodic Oscillations with relative amplitude larger than 2 and a period of $10 - 100$s. Those results are applied to model heartbeat states qualitatively. Eqs. (4.21) and (4.25) allow us to determine the values of BH masses for the accretion disks and the μ parameter. The results are given in Table 4.5. For the ρ-type light curves the parameter $C_{M\alpha}$ of IGR J17091-3624 can be estimated at the level of $3.2 - 3.5$, and GRS 1915+105 at the level of $3.7 - 3.9$.

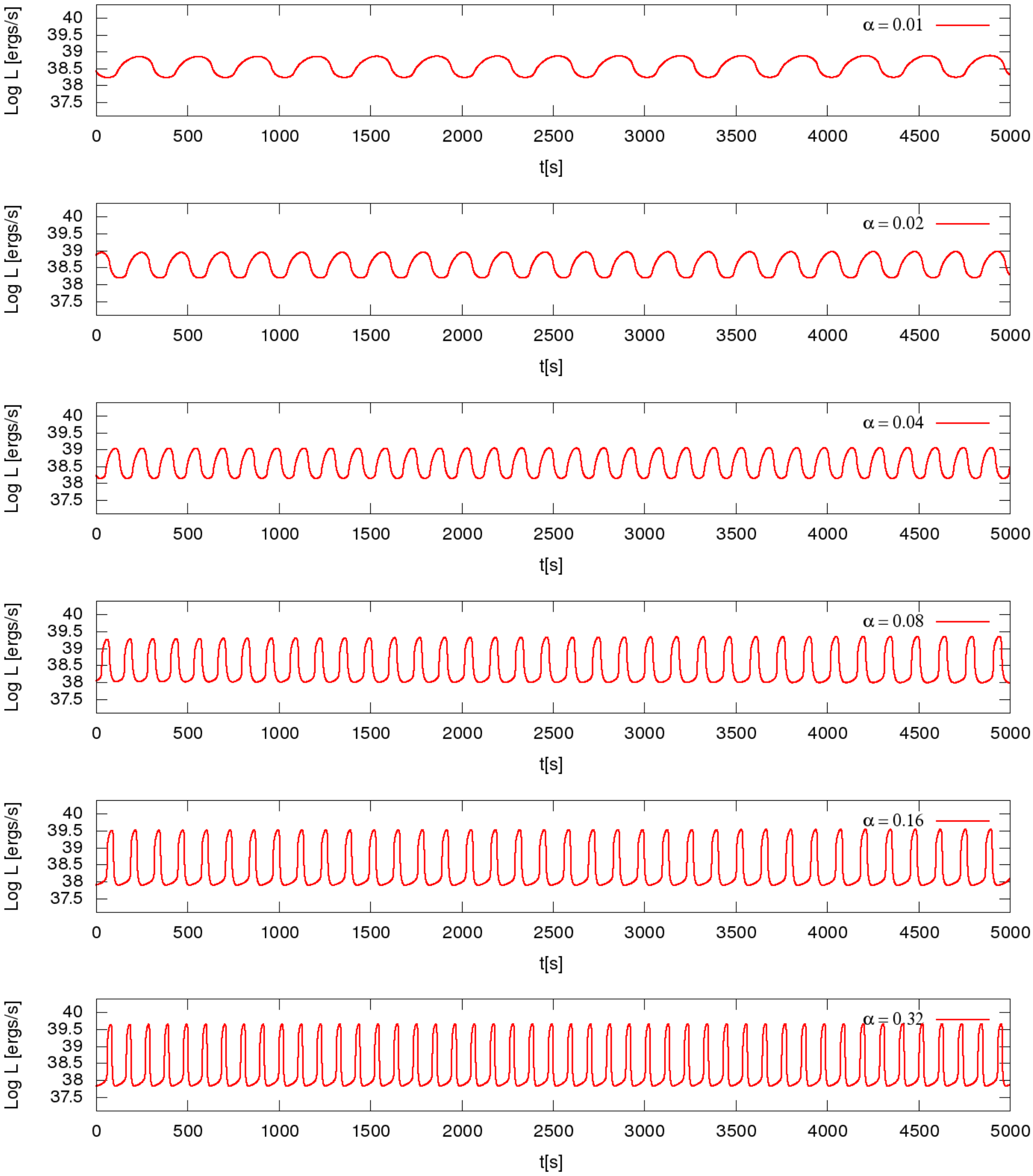

Figure 4.12: Light curves for six different values of α for $M = 10M_\odot$, $\dot{m} = 0.64$, and $\mu = 0.6$.

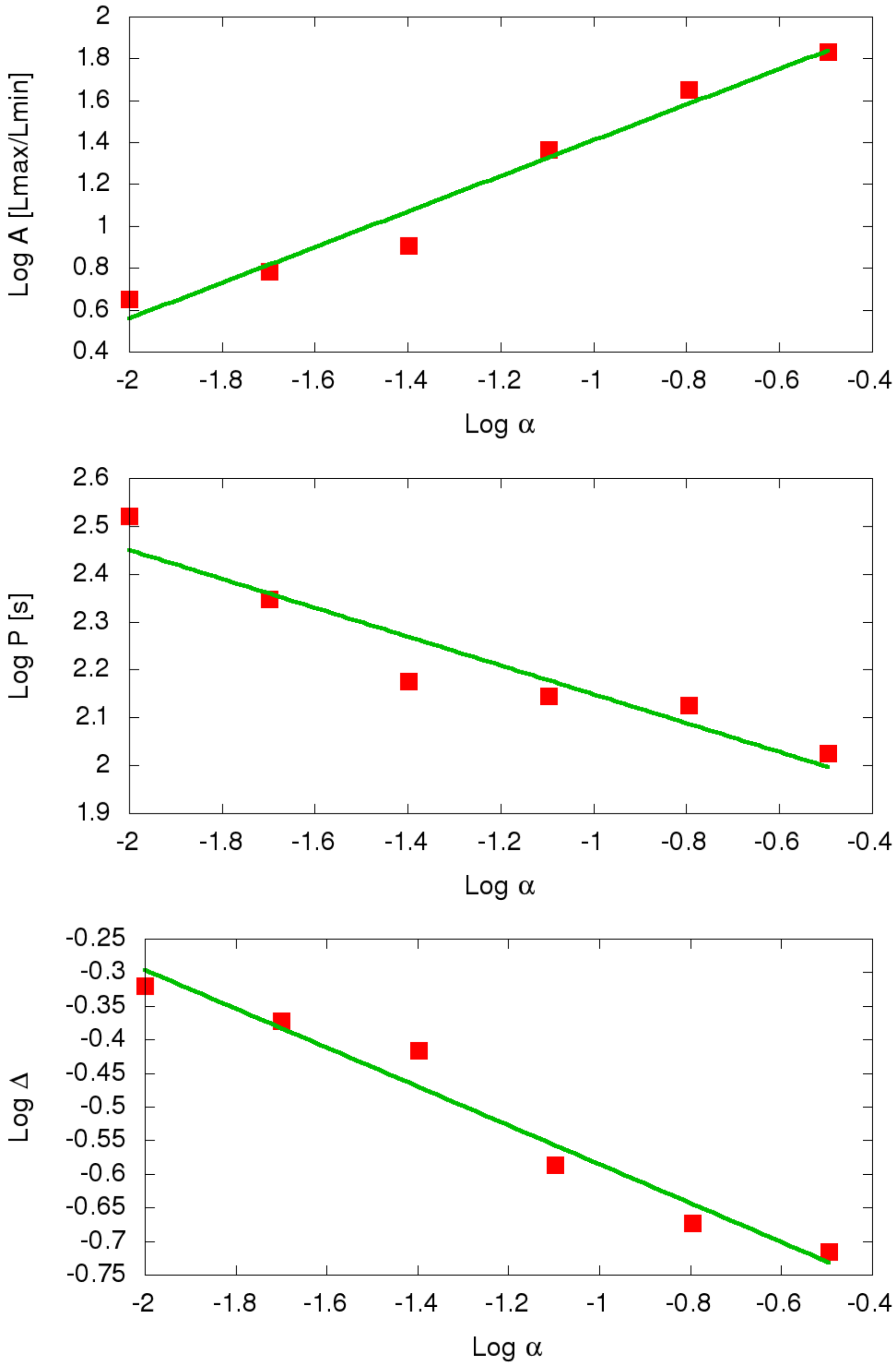

Figure 4.13: Dependence between the α parameter and observables for $M = 10M_{\odot}$, $\dot{m} = 0.64$, and $\mu = 0.6$ for $\alpha \in [0.01 : 0.32]$.

source	ID	$*\mathcal{M}$	$\frac{M}{M_\odot}$	α
IGR	ν_I	6.38	$3.95 - 4.45$**	$0.0155 - 0.0165$
IGR	ρ_{IA}	3.52	$3.95 - 4.45$**	$0.0213 - 0.0227$
IGR	ρ_{IB}	3.198	$3.95 - 4.45$**	$0.0223 - 0.0238$
IGR	ν_I	6.38	$8.7 - 15.6$***	$0.0235 - 0.0321$
IGR	ρ_{IA}	3.52	$8.7 - 15.6$***	$0.0323 - 0.0441$
IGR	ρ_{IB}	3.198	$8.7 - 15.6$***	$0.0330 - 0.0446$
GRS	ν_G	8.31	$9.5 - 10.7$	$0.0214 - 0.0228$
GRS	ρ_{GA}	3.87	$9.5 - 10.7$	$0.0322 - 0.0343$
GRS	ρ_{GB}	3.77	$9.5 - 10.7$	$0.0327 - 0.0348$

Table 4.6: Determination of α values based on the known IGR and GRS mass values (Rebusco et al., 2012; Steeghs et al., 2013; Iyer et al., 2015) and mass-α relation presented in Table 4.5. Descriptions of the sources, their states and OBSIDs are presented in Table 4.5. * - Mass - α factor ($\frac{M}{M_\odot}(\frac{\alpha}{0.02})^{-1.88}$). ** - IGR mass estimation from Rebusco et al. (2012) and (Steeghs et al., 2013) *** - IGR mass estimation from Iyer et al. (2015).

We also determine $\mu = 0.58 - 0.63$ for IGR J17091-3624 and $0.58 - 0.66$ for the *GRS* 1915, respectively. From the ν-type light curves values of $C_{M\alpha}$ parameters and μ are significantly larger. Our model thus works properly for the periodic and regular oscillations, which are produced in the accretion disk for a broad range of parameters, if only the instability appears. Irregular variability states α, β, λ and μ should be regarded as results of other physical processes. The explanation of class κ of the microquasar GRS 1915 variable state (Belloni et al., 2000) which presents modulated QPOs, seems to be on the border of applicability. In general, the method is correct for estimation of the order of magnitude, although not perfect for exact determination of the parameters due to the nonlinearity of the model. For this Chapter a constant value of $\alpha = 0.02$ was assumed, which could not be true for all values of masses. For a source with known mass, such as GRS 1915 (Greiner et al., 2001; Steeghs et al., 2013), previous estimations as a limitation for the value of α can be used, as presented in Section 4.8.2. Steeghs et al. (2013) estimated the mass of GRS1915 at the level $10.1 \pm 0.6 M_\odot$. From the high-frequency QPO comparison method used by Rebusco et al. (2012) the GRS/IGR mass ratio, which is at the level of 2.4 can be known. Combining the results of Rebusco et al. (2012) and later the GRS 1915 mass estimation from Steeghs et al. (2013), for the IGR J17091 we get $M = 4.2 \pm 0.25 M_\odot$. Results of Iyer et al. (2015) suggest the probable mass range of IGR J17091 is between 8.7 and $15.6 M_\odot$. From Tables 4.5 and 4.8.2 we conclude the possible dependence between α and the variability state or the source type. For the ν state of IGR it has been found $\alpha \approx 0.0155 - 0.0165$, for the ρ state of this source $\alpha \approx 0.021 - 0.024$, for the ν state of GRS $\alpha \approx 0.021 - 0.023$ and for the ρ state of GRS $\alpha \approx 0.032 - 0.035$. Those values can change under the assumption of the BHs spin, which can be near to extreme in the case of GRS 1915 and very low, even retrograde in the case of IGR J17091 (Rao & Vadawale, 2012). In our current model the presence of accretion disk corona is neglected.

Following the mass estimation done by Iyer et al. (2015), results in quite a consistent model for both microquasars' ν and ρ variability states - $\alpha \approx 0.023$ for the ν state and $\alpha \approx 0.033$ the ρ state, under assumption of the mass of IGR at the level of $9 - 10 M_\odot$, that is, close to the lower limit from results of Iyer et al. (2015).

The above results under the assumption of negligible influence of coronal emission on the light curve. According to Merloni & Nayakshin (2006), power fraction f emitted by the corona is given by the following formula:

$$f = \sqrt{\alpha}\left[\frac{P}{P_{\rm gas}}\right]^{1-\mu}. \tag{4.41}$$

For our model with $\alpha = 0.02$, the values of f are low, where $f = 0.141(\frac{P}{P_{\rm gas}})^{1-\mu}$, which for the values of μ investigated in the paper fulfills the inequality of $0.0125 < f < 0.141$, assuming a threshold maximal value of the gas-to-total pressure rate $\beta = \frac{P_{\rm gas}}{P}$ from Eq.(4.12). According to the fact that the *heartbeat* states are strongly radiation-pressure dominated and the coronal emission rate is lower for lower values of the μ parameter (which are more likely to reproduce the observational data), the coronal emission can be regarded as negligible.

4.8.3. Disk instability in supermassive black holes

In the scenario of radiation pressure instability, with a considerable supply of accreting matter, the outbursts should repeat regularly every $10^4 - 10^6$ years (Czerny et al., 2009). From the grid of models performed in Czerny et al. (2009), done for $\mu = 0.5$ ($\tau_{r\phi} = \alpha\sqrt{PP_{\rm gas}}$) and $10^7 M_\odot < M < 3\times 10^9$, they obtained the following formula expressing correlation between the duration time, α parameter and bolometric luminosity $L_{\rm bol}$:

$$\log(\frac{T_{\rm dur}}{\rm yr}) \approx 1.25\log(\frac{L}{\rm ergs^{-1}}) + 0.38\log(\frac{\alpha}{0.02}) + 1.25\log K - 53.6 \tag{4.42}$$

which, for the special case $\alpha = 0.02$ and neglecting the bolometric correction, has the following form:

$$\log\frac{L_{\rm bol}}{\rm ergs^{-1}} = 0.8\log(T_{\rm dur}/s) + 42.88. \tag{4.43}$$

The formula (4.43) also found its confirmation in observational data for different scales of BH masses, as presented in Fig. (4.14). This applies despite the assumption of $\mu = 0.5$ since the expected dependence on μ is weak. Combining Eqs. (4.21) and (4.25), we get:

$$\log(T_{\rm dur}/s) = (1.15 - 1.2(\mu - 3/7))\log M + 0.83\log A - 1.9\mu + 0.83. \tag{4.44}$$

Basing on the Fig. (4.14) the approximate dependence can be assumed:

$$\log A = 0.4\log M + 0.25, \tag{4.45}$$

since for the same model input parameters (e.g. $\log\dot{m} = -0.2$, $\alpha = 0.02$ and $\mu = 0.56$) the amplitude could be even a hundred times larger for the case of AGNs than for microquasars. Combining Eqs. (4.44) and (4.45) and adopting $L_{bol} = \dot{m}L_{Edd,\odot}$ where $L_{Edd,\odot} = 1.26\times 10^{38}$erg s^{-1}:

$$\log(T_{\rm dur}/yr) = (1.91 - 1.2\mu)(\log L - \log L_{\rm Edd\odot} - \log\dot{m}) - 6.68. \tag{4.46}$$

The Eq. (4.46) can be inverted:

$$\log L = \frac{1}{1.91 - 1.2\mu}\log(T_{\rm dur}/yr) + 37.1 + \frac{6.68}{1.91 - 1.2\mu} + \log\frac{\dot{m}}{0.1}. \tag{4.47}$$

The above Equation is a generalised version of the results from Czerny et al. (2009). In Fig. (4.14) the observational points from Wu et al. (2016) are presented, along with the theoretical lines as a result from Eq. (4.47) for several values of μ. There is an

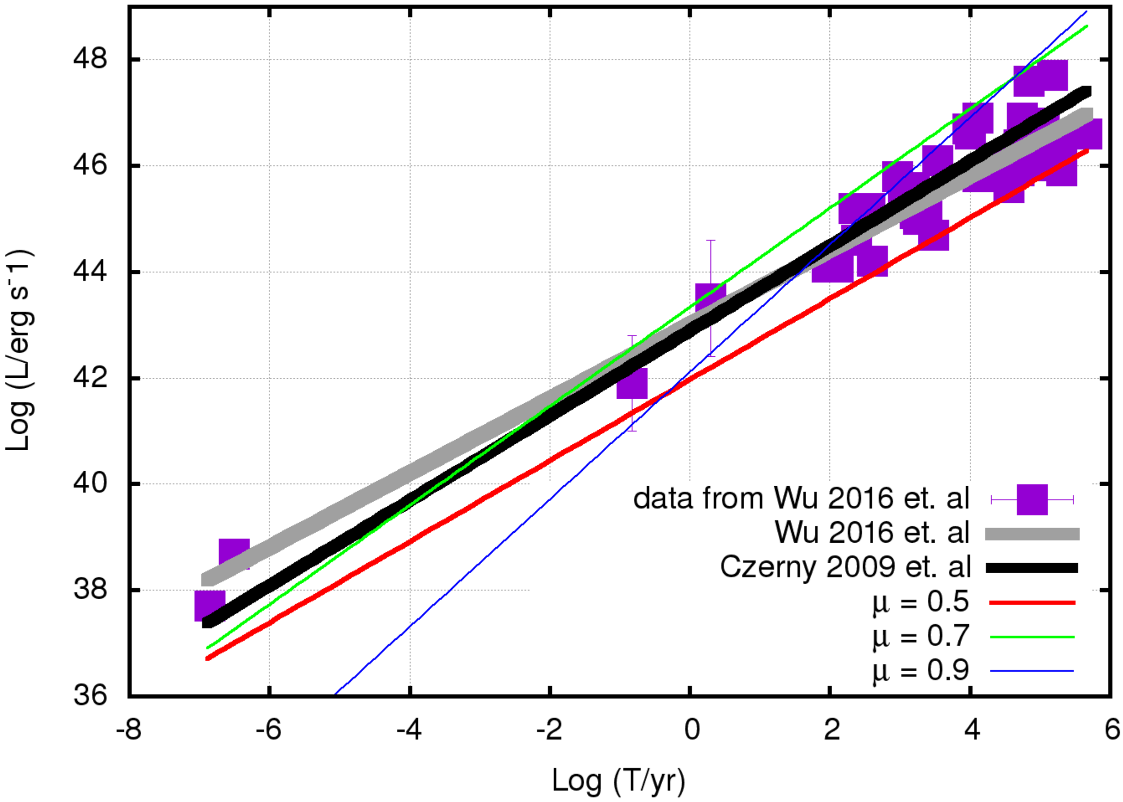

Figure 4.14: Correlation between the bolometric luminosity and the outburst duration for different-scale BHs. Thick lines represent the best fit from Wu et al. (2016), and the prediction from Czerny et al. (2009). Thin lines represent Eq. (4.47) for several different values of μ, assuming $\dot{m} = 0.1$.

assumption that the Eddington accretion rate and the accretion efficiency are roughly independent for different BH masses. The proportionality coefficient in Eq. (4.42) changes from 1.25 to $1.91 - 1.2\mu$.

The coefficient in Eq. 4.42 is equal to 1.19 for $\mu = 0.6$. For most of the known AGNs, except for the Low Luminosity AGNs, their luminosity in Eddington units is over 0.02 (McHardy et al., 2006), and the sources remain in their soft state, so the radiation pressure instability model should apply. The weak sources claimed to be AGNs, such as NGC4395 and NGC4258 (Lasota et al., 1996; Filippenko & Ho, 2003) are claimed to be in the hard state, being not described accurately by the accretion disk model of Shakura-Sunyaev. It should be possible to study the evolution of those sources statistically. Based on the known masses, accretion rates, and timescales for AGN, the luminosity distribution for the samples of AGN with similar masses or accretion rates can be acquired. This should allow us to reproduce an average light curve for a range of masses and accretion rates for a survey of the known AGNs (Wu, 2009). The averaged light curve for a big ensemble of AGN will help us to provide expected luminosity distributions or luminosity-mass, luminosity-duration relations for the AGNs existing in the universe. However, high-amplitude outbursts may complicate the study since the detection of the sources between the flares may be strongly biased as the sources become very dim. Existence of the likely value of $\mu \approx 0.6$, proven by comparison of Eqs. (4.42) and (4.46), could also help in mass determination of newly discovered objects.

Another interesting situation comprises the so-called Changing-Look-AGN, such as IC751 (Ricci et al., 2016). Although most AGN have a variability timescale on the order of thousands of years, the shape of model light curves (sharp and rapid luminosity increases) could suggest that, for some cases, luminosity changes can be observed.

4.8.4. Conclusions

A possible application of the modified viscosity model is proposed as a description of a regular variability pattern (heartbeat states) of black hole accretion disks for the microquasars, IMBHs and AGNs. The model works for optically thick, geometrically thin disks and determines the range and scale of the radiation pressure instability. The parameter μ, which describes viscosity, in a more general way, taking into account the relative contribution of pressure component, can reproduce a possibly stabilising influence of the strong magnetic field in the accretion disk. Nonlinearity of the models causes appearance of different modes of the disk state (stable disk, flickering, outbursts). Thanks to the computation of large grid of models, quantitative estimations for the variability periods and amplitudes were presented. The model light curves reproduce several different variability patterns. Also, many observables, such as, L, P, A, and Δ, can be used directly to determine the physical parameters, like α, μ, M, and $\dot{m}$. Finally, our model can be successfully applied to the mass and accretion rate determination for the intermediate-mass black hole candidate HLX-1, which will be presented in the next Chapter.

Chapter 5

The Ultraluminous X-ray source HLX-1

5.1. Introduction

The last years brought more examples of occurence of the radiation pressure instability. The timescales for Active Galactic Nuclei are still too long to observe even only one limit-cycle, even for the least massive objects. However, the model-based formulae from Chapter 4, can be applied to the class of accretion disk sources surrounding the *Intermediate-Mass Black Holes* ($10^3 - 10^6$ solar masses). This Chapter involves the case of newly discovered Intermediate-Mass Black hole HLX-1 as an example of such a source. In this Chapter, we use the method defined previously to determine the mass and accretion rate of that source, independetly on the previous spectral-based analysis. We suggest the radiation pressure instability as a mechanism driving the observed limit-cycle oscillations in this source.

5.2. Ultraluminous X-ray sources

The Ultraluminous X-ray sources (ULXs) are X-ray sources that exceed the Eddington limit for accretion on stellar-mass black holes. This class does not contain the Active Galactic Nuclei since their cases are well described and classified into Quasars or Narrow Line Seyfert I galaxies. So this term involve mostly the sources with luminosities at the level $10^{39} - 10^{44}$ erg s $^{-1}$. Among these sources we can extract several classes with a distinct nature. The two most important are ULXs containing the Neutron Stars presenting the beamed emission and Intermediate Mass Black Holes (King & Lasota, 2016). Examples of these sources are X-ray pulsars A0538-665, SMC X-16 and GRO J1744-28 (Bachetti et al., 2014). Breaking the Eddington limit, defined in Section 1 is possible only breaking the symmetry of emitting matter. In case of disk or spherical geometry breaking the limits of the standard accretion models forbids the long-lasting emission. However, the case of beamed geometry (with the radiation flux proportional to $\propto \frac{1}{r}$) does not result in one value of critical luminosity being a combination of the physical constants. In such case, the critical luminosity depends on shape and can exceed the Eddington limits tens of times. One of these sources M82 X-2 with luminosity $L \approx 1.8 \times 10^{40}$. Since this thesis is dedicated to systems with thin accretion disks, we will focus on the case of the Intermediate-Mass Black Holes. Some of the IMBH ULXs like $M74X - 14$ ($CXOUJ013651.1 + 154547$), $HLX - 1$ and 47 Tucanae, see Krauss et al. (2005); Farrellet al. (2009); Kilitzan, Baumgardt & Loeb (2017), were recently detected via the spectral analysis. In one of the objects - HLX-1 there appeared a series of documented flares in the X-ray domain, showing the persistent and repetitive nature of that source, which can be regarded as a scaled-up microquasar.

5.3. HLX-1 Intermediate Mass Black Hole

In case of black hole masses ranging from 10^3 to 10^6, the Eddington limit is at the level of $10^{41} - 10^{44}$ erg s^{-1}, and the accretion disk sources with such luminosities can undergo the limit-cycle oscillation driven by the radiation pressure instability. In previous Chapter we estimated the properties of limit-cycle oscillation and also estimated the critical value of Eddington Ratio, $\dot{m}$, necessary for the oscillations. Huge universality of the results presented in previous Chapter makes it possible to give estimations on the period, amplitude and shape of the ligthcurve. Thus we can predict that the accretion disk sources with luminosities $10^{39} - 10^{44}$ erg s^{-1} can perform the limit-cycle oscillations, for a range of their black hole masses. According to results presented in previous Chapter, for an Intermediate Mass Black Hole, the period of such oscillations should be between days and years, and duration of one flare - between hours and year, and the peak luminosity to minimum luminosity ratio (A) can exceed tens or even hundreds, contrary to microquasars. One out of such sources is presented in below.

HLX-1 is the best known case of a ULX being an IMBH candidate, which has undergone six outbursts spread in time over several years with an average period of about 400 days, a duration of about 30-60 days, and a ratio between its maximum and minimum luminosity $L_{\mathrm{max}}/L_{\mathrm{min}}$ of about several tens. The average bolometric luminosity is equal to $((\Sigma_i L_i \Delta t_i)/(\Sigma_i \Delta t_i))$, where L_i is the luminosity at a given moment and Δt_i is the gap between two observation points.

5.3.1. HLX-1 bolometric correction

The SWIFT XRT observed luminosity is at the level of $1.05 \times 10^{42} \times (K/5)$ erg s^{-1}, where K is the bolometric correction. The exact value of the bolometric correction is strongly model-dependent. The fits of the thermal state with the *diskbb* model (Servillat et al., 2011) imply a disk temperature T_{in} in the range of $0.22 - 0.26$ keV, which, combined with the 0.2-10 keV flux and the distance to the source, implies a black hole mass of about $10^4 M_{\odot}$, if the model is used with the appropriate normalization, and a bolometric correction is of 1.5 for the $0.3 - 10$ keV spectral range. The use of the *diskbb* model for larger black hole mass, $10^5 M_{\odot}$, implies an inner temperature, T_{in} of 0.08 keV, much lower than observed, but then a much larger bolometric correction at 6.6. However, the larger mass cannot be ruled out on the basis of the spectral analysis since it is well known that the disk emission is much more complex than the *diskbb* predictions, and in particular the inner disk emission has colour temperature much higher than the local black body by a factor 2 - 3 e.g. (Done & Davis, 2008),Sutton, Swartz & Roberts (2017)). Thus the overall disk emission may not be significantly modified for the outer radii, and the hottest tail can still extend up to the soft X-ray band.

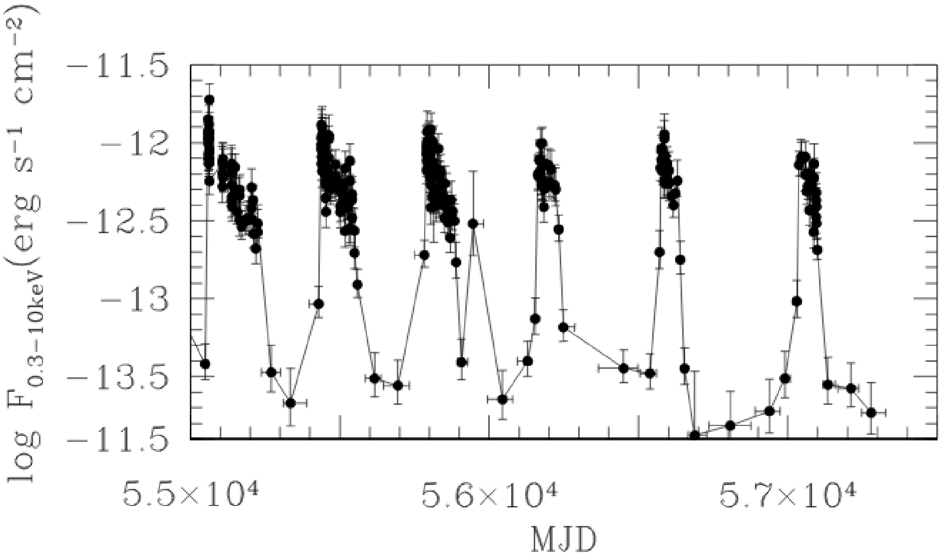

Figure 5.1: The HLX-1 lightcurve. Horizontal axis presents observation time time in Modified Julian Days (MJDs). Vertical axis represents flux registered by the SWIFT XRT device.
Modified Julian Days and date:
MJD 5.5×10^4 = 18th June 2009
MJD 5.6×10^4 = 14th March 2012
MJD 5.6×10^4 = 9th December 2014

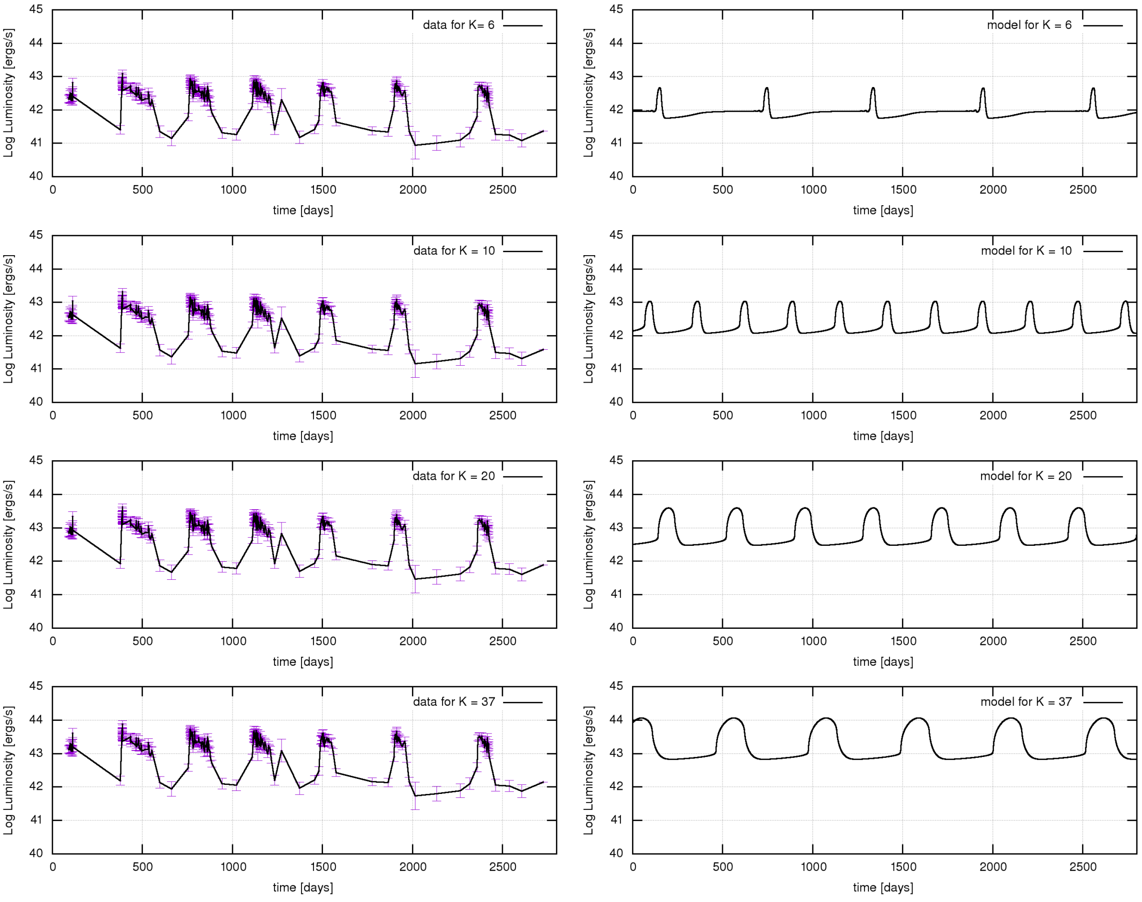

Figure 5.2: Comparison between the SWIFT XRT light curve of HLX-1 and the models. Model parameters: $\mu = 0.54, \alpha = 0.02, \dot{m} = 0.009 * K$ and $M = 1.9 \times 10^5 M_\odot$. The value of the bolometric correction is given in each panel.

5.3.2. HLX-1 mass and accretion rate determination

The model to data comparison (Fig. 5.1), being the result of our analysis, is presented in the Figure 5.2. We can rewrite the Eqs. (4.36) and (4.37) from Chapter 4. Those equations find their application to the HLX-1 mass determination from the lightcurve parameters

$$M[M_\odot] = 0.45 P[s]^{0.87} A^{-0.72}. \tag{5.1}$$

The $\Delta - \mu - M$ dependence from Fig (4.10) and Eq. (4.25), combined with Eq. (4.36) gives us the exact estimation on μ

$$\mu = 3/7 + \frac{-\log\Delta}{1.49 + 1.04\log P - 0.864\log A}. \tag{5.2}$$

The best-fit model of the HLX-1 gives the observables

- P = 400 days,
- A = 20,
- $\Delta = 0.13$.

Assuming $\alpha = 0.02$ results in the following black hole mass and μ determinations:

- $M = 1.9 \times 10^5 M_\odot$,
- $\mu = 0.54$.

Exact value of the Eddington ratio depends on the bolometric correction and is equal to $\dot{m} = 0.009 * K$. This results depend on K because of the huge nonlinearity of the model grid (resulting in a large plateau in the luminosity-Eddington rate dependence). That nonlinearity is responsible for existence of some variability patterns with modest qualitative differences between the lightcurve parameters in each class.

5.3.3. Explanation of the HLX-1 light curve irregularity

The light curve of HLX-1, presented in the Fig. (5.1), despite very regular values of peak luminosity ($\log \frac{L}{\mathrm{ergs}^{-1}}$ between 42.5 and 42.6), presents significant variability of the flare duration. According to our model, for any constant input parameter (mass, Eddington rate, α and μ), period, duration, and amplitude should remain constant. To our knowledge, the only explanation for such a phenomenon is variation in the input parameters. The variability of the central object mass is too faint (approx. 10^{-8} per one cycle for any accreting source) to be visible. The variability of $\dot{m}$ is possible, bearing in mind the fact that accretion rate of HLX-1 (order of $10^{-3} M_\odot$ per one duty cycle) can be significantly disturbed by the tidal disruption of the minor bodies such as planets with mass ranging from $10^{-6} M_\odot$ to $10^{-3} M_\odot$. A detailed description of this process can be found in Evans & Kochanek (1989), and Del Santo et al. (2014) presented its application for the case of phenomena inside the globular clusters. The Eddingtion rate $\dot{m}$ is a global parameter, strongly connected with the accretion disk neighbourhood ($\dot{m}$ can change rapidly in the case of tidal disruption). In contradiction, μ and α are the local parameters describing the MHD turbulence. As α can be connected with the rate of the typical velocity of turbulent movement to the sound speed (Shakura & Sunyaev, 1973), μ can represent the magnetisation of the disk, as shown by the Eq. (4.15). In the HLX-1 observation, out of the four observables, only the Δ parameter was changing significantly between different flares. According to Eq. (4.39) this follows from changing μ. Specifically, the growth of μ from 0.48 to 0.56 is responsible for Δ decreasing from 0.4 to 0.1 . According to those results, μ was growing during the sampling time, which can be explained by a decrease in disk magnetisation.

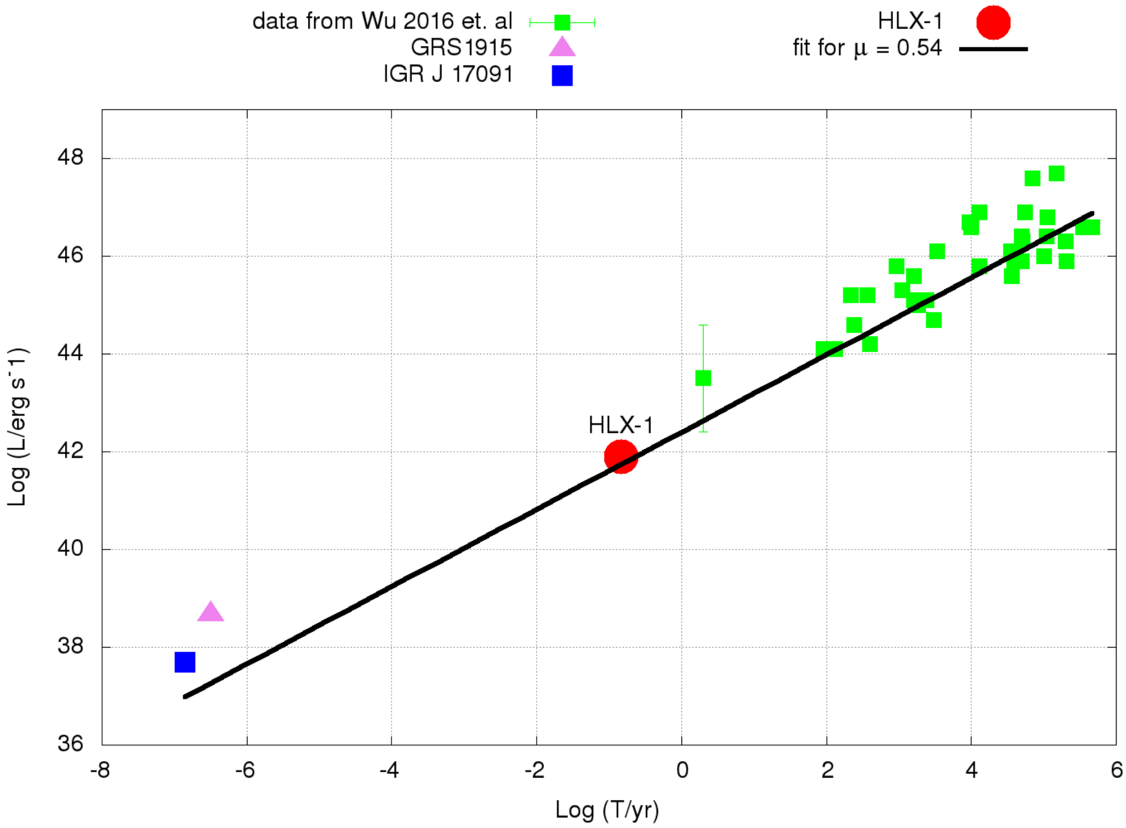

Figure 5.3: The parameters of the HLX-1 on the background of other X-ray sources. Black line represent fit from Eq. (4.47) in case of $\mu = 0.54$, green squares - sample of the AGNs. Triangle and square show the microquasars GRS 1915+105 and IGR J17091-3624, respectively. The plot illustrates a universal correlation between the luminosity and timescales of variability, as predicted by the radiation pressure instability model.

Chapter 6

Influence of the Fe ions on the accretion disk stabilization in AGN

6.1. Introduction

As concluded from the previous Chapter, the radiation pressure instability in accretion disks is a powerful, universal phenomenon driving the limit-cycle oscillations at all scales and being limited by some stabilizing, possibly magnetic processes in the accretion disks viscosity.

However, also other stabilizing mechanisms in the accretion process have been invoked, apart from the viscosity prescription itself. For instance, the propagating fluctuations in the flow (Janiuk & Misra, 2012) may suppress the thermal instability, or at least delay the development of the instability (Ross, Latter & Tehranchi, 2017). As recently discussed by Jiang et al. (2016), a possible stabilizing mechanism for the part of an accretion flow might be the opacity changes connected with the ionization of heavy elements. Using the shearing-box simulations of MRI-driven fluid in the gravitational potential of supermassive black hole (a particular value of black hole mass, $M = 5 \times 10^8 M_\odot$, was used), Jiang et al. (2016) have shown that the flow is stable against the thermal instability, if the opacity includes transitions connected with absorption and scattering on Iron ions. This is because the cooling rate, which includes now not only the Thomson scattering (constant) term, but also the absorption and line emission in the Roseland mean opacity, will depend strongly on density and temperature in some specific regions of the disk. In fact, as will be discussed below in a more detailed way, the dominant term from opacity changes may completely stabilize the flow locally. The simulations of Jiang et al. (2016) showed that effect but they did not describe the global evolution of the flow, which is the subject of present Chapter

In the Chapter 4 the broad grid of models was studied to show that the global evolution of the accretion flow under the influence of radiation pressure instability is a universal phenomenon in the black hole accretion disks across the mass scale. It has been claimed, that the influence of the opacity changes on the global time evolution of the flow is essential, although does not prevent the instability from developing. Examples of lightcurves produced by our numerical simulation illustrate this. This Chapter is organized as follows: in Sect. 6.2 the analytical condition for local thermal instability are presented, in Sect. 6.3 the values of κ opacities for the typical accretion disk densities and temperatures and range of the Iron Opacity Bump are discussed. Its influence on global disk behaviour is described in Sect. 6.4.

In this Chapter, the model described in Chapter 4 is extended, with respect to the atomic opacities. Basing on the accretion disks theory, presented in Chapters 2 and 3, and modified viscosity prescription form Eq. (4.12), described and tested in Chapter 4 and applied in Chapter 5 for the mass and accretion rate determination of the Intermediate Mass Black Hole HLX-1, we finally make an attempt to generalize our model even more, regarding the thermal instability of the optical thickness $\tau = \kappa\Sigma$, coming from the atomic contribution to the κ opacity function. Basing on the tabelarized database (Alexander et al., 1983; Seaton et al., 1994; Rozanska et al., 1999), we try to find stabilizing and destabilizing effects among all the mass-scale for the Black Hole accretion disks, from the lightest stellar mass black holes (order of magnitude of one solar mass) to the heaviest Active Galactic Nuclei (order of magnitude of ten bilion solar masses).

6.2. Local thermal stability in accretion disks

The domination of radiation pressure in the accretion disk leads to the thermal instability (Pringle, Rees & Pacholczyk, 1973; Lightman & Eardley, 1974; Shakura & Sunyaev, 1976; Janiuk, Czerny & Siemiginowska, 2002). At the instability the heating rate Q_+ grows faster with temperature than cooling rate Q_-. The appearance of local thermal instability is given by the condition:

$$\frac{d\log Q_-}{d\log T} < \frac{d\log Q_+}{d\log T}. \tag{6.1}$$

The analysis performed in Chapter 4, under the assumption on constant surface density during thermal timescales leads to following formula on heating rate derivative:

$$\frac{d\log Q_+}{d\log T} = 1 + 7\mu\frac{1-\beta}{1+\beta}, \tag{6.2}$$

where $\beta = P_{\rm gas}/P$. For the case of this work, $\alpha = 0.02$ and $\mu = 0.56$, being typical for the IMBH and AGN disks are fixed. These values has been chosen since the dynamics of the outbursts of the disk matches the observed properties of the sources as shown in Chapter 4. These values reproduce the correlation between the bolometric luminosity and outburst duration known for the observed sources, especially microquasars and Intermediate Mass Black Holes.

The radiative cooling rate depends on disk surface density Σ and physical constants Stefan-Boltzmann σ_b and speed of light. The radiative cooling rate is given by formula from Eq. (2.21). For the radiation pressure dominated disk, combined with Eqs.(6.1) and (6.2), from Eq. (2.21) for $\mu = 0.56$ we obtain the condition:

$$\frac{d\log Q_-}{d\log T} < 4.92. \tag{6.3}$$

In the model used in Chapters 3, 4 and 5 only Thomson scattering (described in Chapter 1) was assumed, which resulted in the appearance of global radiation pressure instability among sub-Eddington accretion disks. The recent results of Jiang et al. (2016) are based on stabilizing influence of the Iron opacity components. To confront the results of their short time, local 3D MHD shearing-box simulation, we propose the global model, used in previous Chapters.

Assuming κ being in general not constant function of ρ and T, the formula for log derivative of Q_- is following:

$$\frac{d\log Q_-}{d\log T} = 4 + \frac{\partial \log \kappa}{\partial \log T} - \frac{4-3\beta}{1+\beta}\frac{\partial \log \kappa}{\partial \log \rho}. \tag{6.4}$$

The Eq. 6.4 shows possible stabilizing influence of the negative slope of κ dependent on T and destabilizing influence of the positive slope of κ. Also the dependence on ρ has inluence on disk stability. The value of κ itself is not important in the local stability analysis. In case of unstable disk, less efficient cooling being an effect of the greater κ lowers the temperature of unstable equilibrium solution, and enlarge the temperature of stable solution, which can modify the duty cycle quantitatively but not qualitatively. Similarly to Chapter 4 of this thesis, the necessary value for the thermal instability is as follows:

$$\beta < \frac{7\mu + 3 - \frac{\partial \log \kappa}{\partial \log T} + 4\frac{\partial \log \kappa}{\partial \log \rho}}{7\mu - 3 + \frac{\partial \log \kappa}{\partial \log T} - 4\frac{\partial \log \kappa}{\partial \log \rho}}. \tag{6.5}$$

The thermal stability parameter s can be defined:

$$s = \frac{d\log Q_+}{d\log T} - \frac{d\log Q_-}{d\log T}. \tag{6.6}$$

Using the Eqs. (6.2) and (6.4), Eq. (6.6) can be written as follows:

$$s = -3 + 7\mu\frac{1-\beta}{1+\beta} - \frac{\partial \log \kappa}{\partial \log T} + \frac{4-3\beta}{1+\beta}\frac{\partial \log \kappa}{\partial \log \rho}. \tag{6.7}$$

The s parameter is connected with the Lyapunov exponent for the system described by the energy equation in the accretion disk with stress tensor given by Eq. (4.5). The value $s > 0$ means locally thermally unstable disk, $s \leq 0$ - locally thermally stable. Assuming $\mu = 0.56$ and $\beta << 1$ for $\rho = 10^{-8}$g cm^{-3} and $T = 10^5$ K, $s = -11$, which corresponds to local thermal stability. Nevertheless, for this density the parameter s gains positive values for $T > 3 \times 10^5$ K. Below this temperature, for $T > 1.75 \times 10^5$ K, the disk is locally thermally stable because of the negative slope of the bump. For temperatures in the range $1.1 - 1.75 \times 10^5$ K, the disk is locally thermally unstable.

6.3. The variable κ - Iron Opacity Bump

The opacity κ is the local function describing interaction of photons with matter from accretion disks. Under the assumptions of local thermal equilibrium, radiation and gas contribution to the total pressure, and local vertical hydrostatic equilibrium, both the heating and cooling rates can be described as a function of radius r, local density ρ and local temperature T. Although the radius r, affecting the angular momentum transport is important for the heating rate in the α-disk model, it affects the stability analysis only indirectly, via the parameters of stationary solutions. In Fig. (6.1) the profiles of the total opacity for solar metallicity are presented, computed as a function of density and temperature (Alexander et al., 1983; Seaton et al., 1994; Rozanska et al., 1999). The combined conditions (6.2) and (2.21) to the opacity values results in the significant local stabilization for the temperatures of $1-4\times 10^5$ K and densities about 10^{-8}g cm^{-3} typical for the AGN accretion disks.

The κ function was fitted with following formulae:

$$\kappa = \kappa_{\mathrm{Th}} + \kappa_{pl} + \kappa_{\mathrm{bump}}$$
$$\kappa_{\mathrm{Th}} = 0.34\mathrm{cm}^2\mathrm{g}^{-1},$$

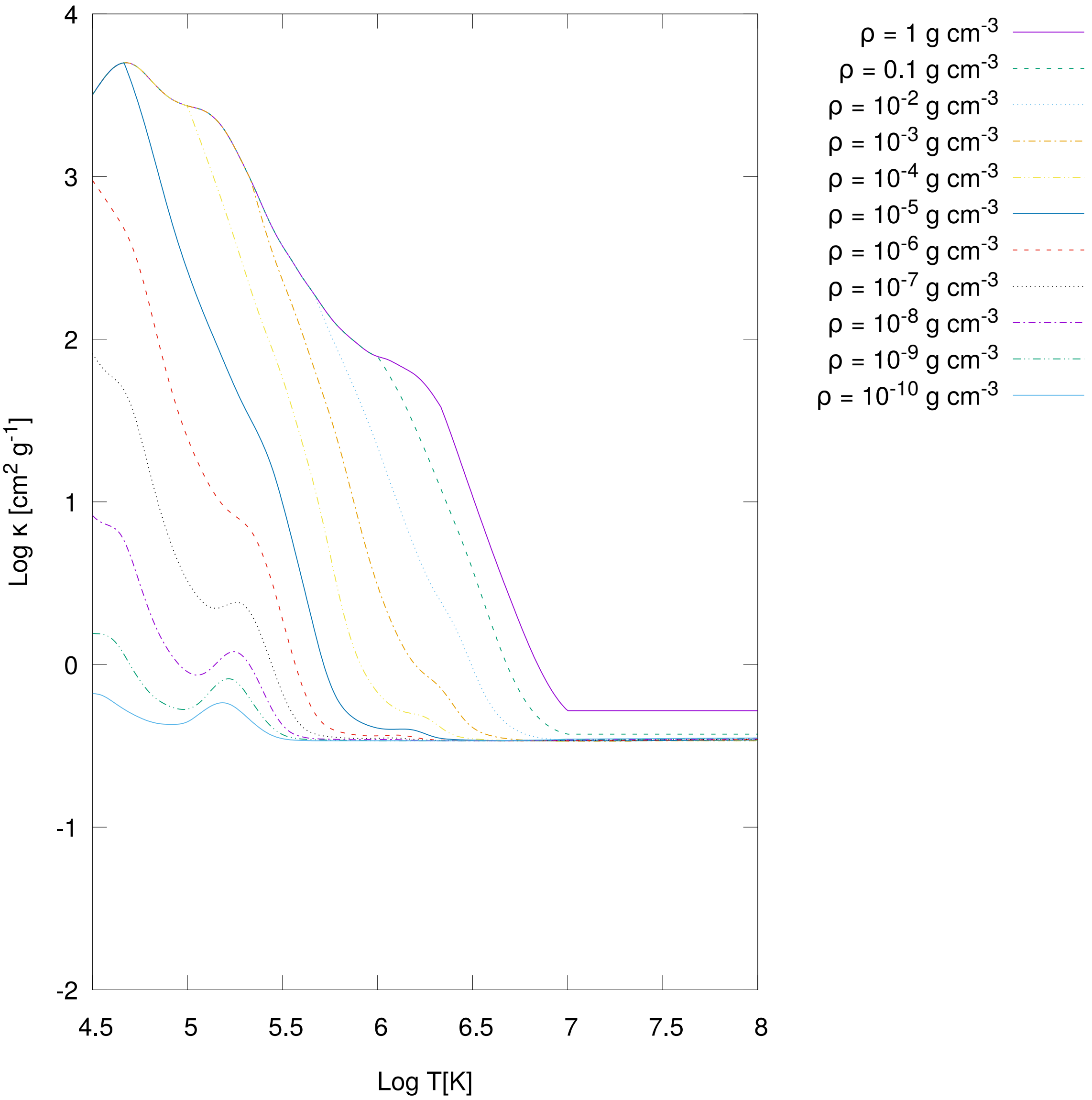

Figure 6.1: The opacity κ functions including atomic components. The data are taken from (Alexander et al., 1983; Seaton et al., 1994; Rozanska et al., 1999).

$$\kappa_{pl} = 4.6 \times 10^{23} \rho T^{-3.5}, \tag{6.8}$$

$$\kappa_{\rm bump} = 39.8 \rho^{0.2} (0.8 \exp -(\frac{T - 1.75 \times 10^5 \rm K}{8.2 \times 10^4 \rm K})^2 + 6.3 \exp -(\frac{T - 4 \times 10^4 \rm K}{3 \times 10^4 \rm K})^2).$$

The negative stabilizing slope of the Iron Opacity Bump is visible in the Figure 6.1. In Fig. (6.2) in the upper panel we show the opacities directly from the tables (Alexander et al., 1983; Seaton et al., 1994; Rozanska et al., 1999), and in the lower panel we present the analytical approximation of opacity function from Eq. (6.8). The detailed results of the dynamical model are presented below.

6.4. Global model

6.4.1. Values of ρ and T

In Fig. (6.3) we present typical values of ρ and T for a wide range of accretion disks, computed via the GLADIS code. For the values of ρ and T in the upper left corner, the power law term of κ dominates, but matter with this parameter is too dense and too cold for central areas of sub-Eddington accretion disks. The oblique belt below presents typical values of ρ and T for the accretion disks with different masses. This area, for $5.1 < \log T < 5.4$, is covered by the Iron Opacity Bump, with stabilizing negative slope (See Sect. 6.2). According to these results, the stabilizing effect of the negative slope of the Iron Opacity Bump can be visible only for the Active Galactic Nuclei accretion disks with $M \approx 10^8 - 10^9 M_\odot$.

6.4.2. Results for the full model with bump

The simulations of the global disk behaviour are performed using the time-dependent global code GLADIS (see Chapter 3 for more details). For the purpose of this Chapter we adopted the version with stress tensor input presented in Chapter 4 in Eq. (4.5). To reproduce the conditions from Jiang et al. (2016), we adopted the following parameters:

- $M = 5 \times 10^8 M_\odot$
- $\dot{m} = 0.03$
- $\alpha = 0.02$
- $\mu = 0.56$

The major change in the numerical model in comparison to Chapter 5 is replacing constant Thomson κ with Eq. (6.8). Similarly to Jiang et al. (2016), it has been assumed that the source accretes at the = 0.03 of the Eddington rate. The results of the time-dependent model are presented in Fig. (6.4). The local shearing-box simulation resulted in significant stabilization of the disk (Jiang et al., 2016). However, the global model does not confirm these results. The stabilization of the disk, which appears according to local prediction, is not found in global models considering a large range of radii. Fig. (6.4) presents the profile of the stability parameter s defined in Eq. (6.6). For the inner area of the disk, Thomson component of opacity dominates and temperature is too large to expect any form of stabilization. Outer area of the disk are characterized

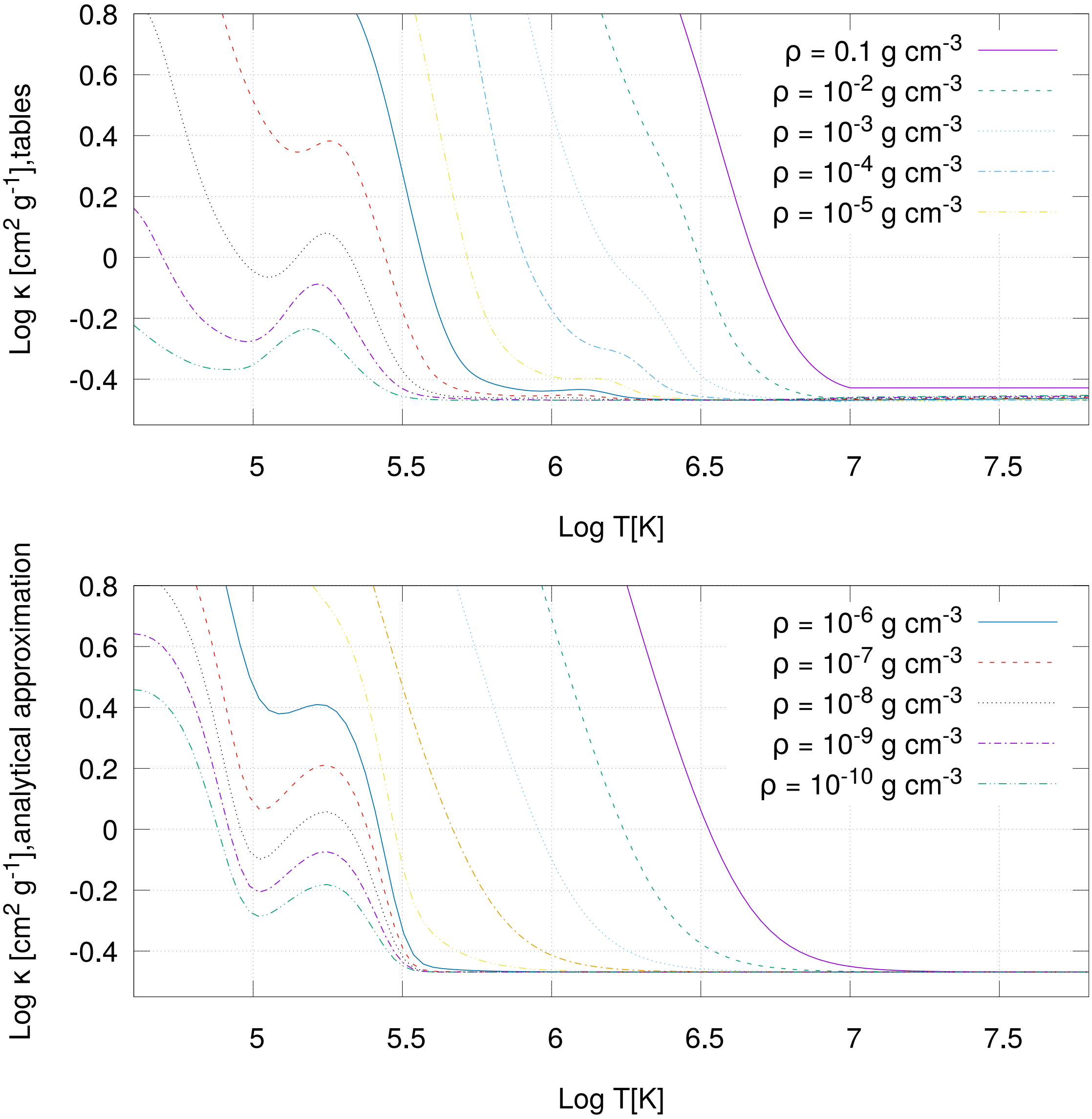

Figure 6.2: Top panel shows results from the tables (Alexander et al., 1983; Seaton et al., 1994; Rozanska et al., 1999), and bottom panel shows the analytical approximation (Eq. 6.8).

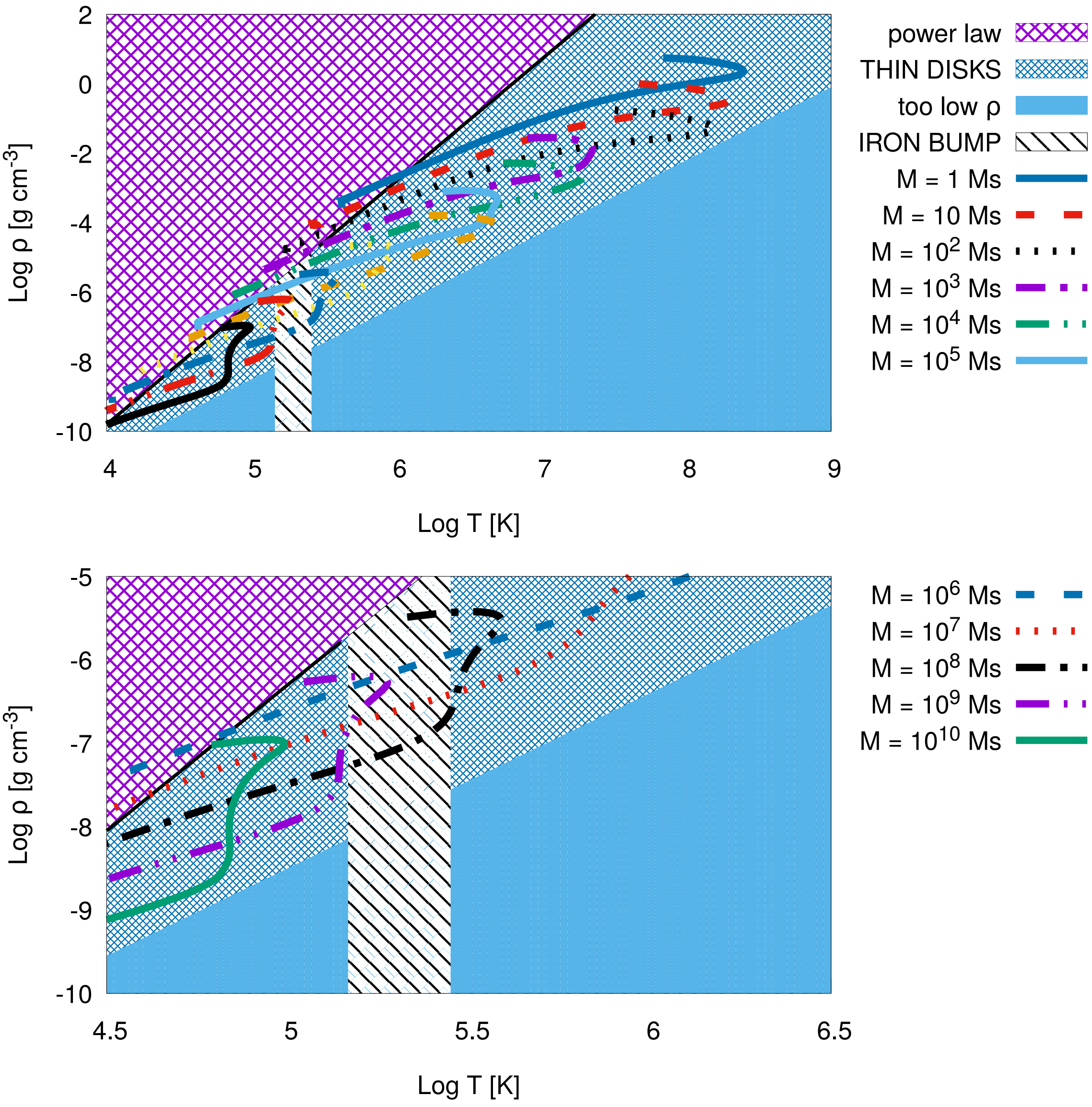

Figure 6.3: Typical values of the ρ and T for Eddingtonian thin disks for central object mass between 1 and $10^{10} M_\odot$. We set $\dot{m} = 0.03$.

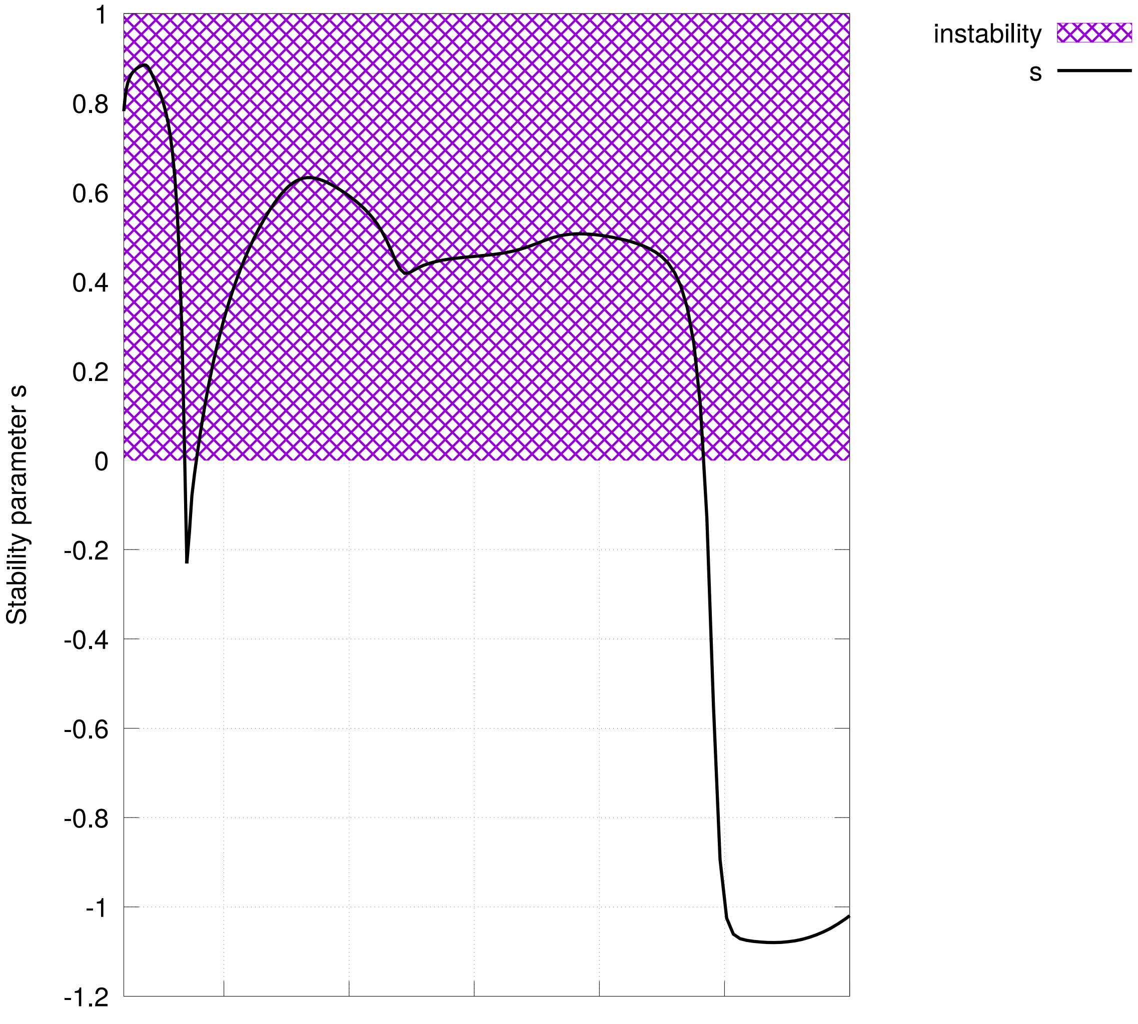

Figure 6.4: The stability parameter, defined in Eq.(6.6) during the outburst for $M = 5 \times 10^8 M_\odot$, $\dot{m} = 0.03$ (same as in Jiang et al. (2016)).

model	amplitude A	period P [yrs]	width Δ
κ with bump	16.1	12635	0.0023
Thomson κ	156	70197	0.0044

Table 6.1: The table describing the flare parameters for the model from Fig. (6.5) with κ described by formula (6.8) (second row) and only Thomson κ (third row).

by the larger value of total opacity temperature about $1.5 - 2 \times 10^5 K$ and negative values of s (the *bump* temperatures). The significant gradient of s is correlated with the gradient of temperature and gradient of κ in the opposite direction. The stability parameter, presented in Fig. (6.4) can reach values between -3 and $-3 + 7\mu$ (0.92 for our choice of μ). In Fig. (6.4) the typical profile of the s parameter is presented. As the bump is approximately Gaussian function, centered at 1.75×10^5 K, with standard deviation $\sigma = 0.82 \times 10^5$ K, it is expected that the strongest effect of the stabilizing slope would be visible for such temperatures. The combined outcome of the stabilizing influence of the negative slope of the bump and destabilizing influence of the positive slope of the bump for the dynamical model is presented in Fig. (6.5). In contrast to the results of Jiang et al. (2016), the Iron bump does not stabilize the disk.

However, it complicates the lightcurve pattern (many small short flares preceding main outbursts instead of one simple flare), due to the complexity of the photon absorption process, but the inner regions of the disk remains hot enough to perform the limit-cycle oscillations. In effect, the bump partially stabilizes the disk - the amplitude $L_{\max}/L_{\min}$ decreases from 156 for model with constant κ (bottom panel Fig. 6.5) to 16.1 for model with bump (upper panel of Fig. 6.5). The detailed analysis of the lightcurve shape is presented in Table 6.1.

Since the timescales presented in Fig. (6.5) are much longer than the duration of observation (lasting up to several decades), it is impossible to find such a lightcurve using the direct method. For such a black hole mass, during the phase of fastest growth of the luminosity, the luminosity change can reach 1 per cent per year. The shape of the lightcurve can be reflected in the Eddington rate statistics - similar objects, being in the different phase of the limit-cycle presented in Fig. (6.4) can emit the radiation with different luminosity and spectra. However, in case of much smaller black hole masses new timescales are perhaps accessible to observations. For example, digitalization of Harvard plates (Grindlay et al., 2012) [1] will bring lightcurves on the order of a hundred years and perhaps the outbursts of AGN disks can be discovered.

6.5. Conclusions

In Chapter 4 the large grids of models were described, confirming the universality of radiation pressure instability across the BH mass-scale. In this Chapter we the opacity prescription has been changed to examine the heavy atoms influence on the accretion disk instability. Comparison between two models presented in Table 6.1 leads to the conclusion that heavy atoms stabilize the disk partially, but do not imply that the variability vanishes. This stabilizing effect manifests itself rather in a significant period and amplitude decrease, without a relative broadening of the outbursts with respect to their

---

[1] http://dasch.rc.fas.harvard.edu/

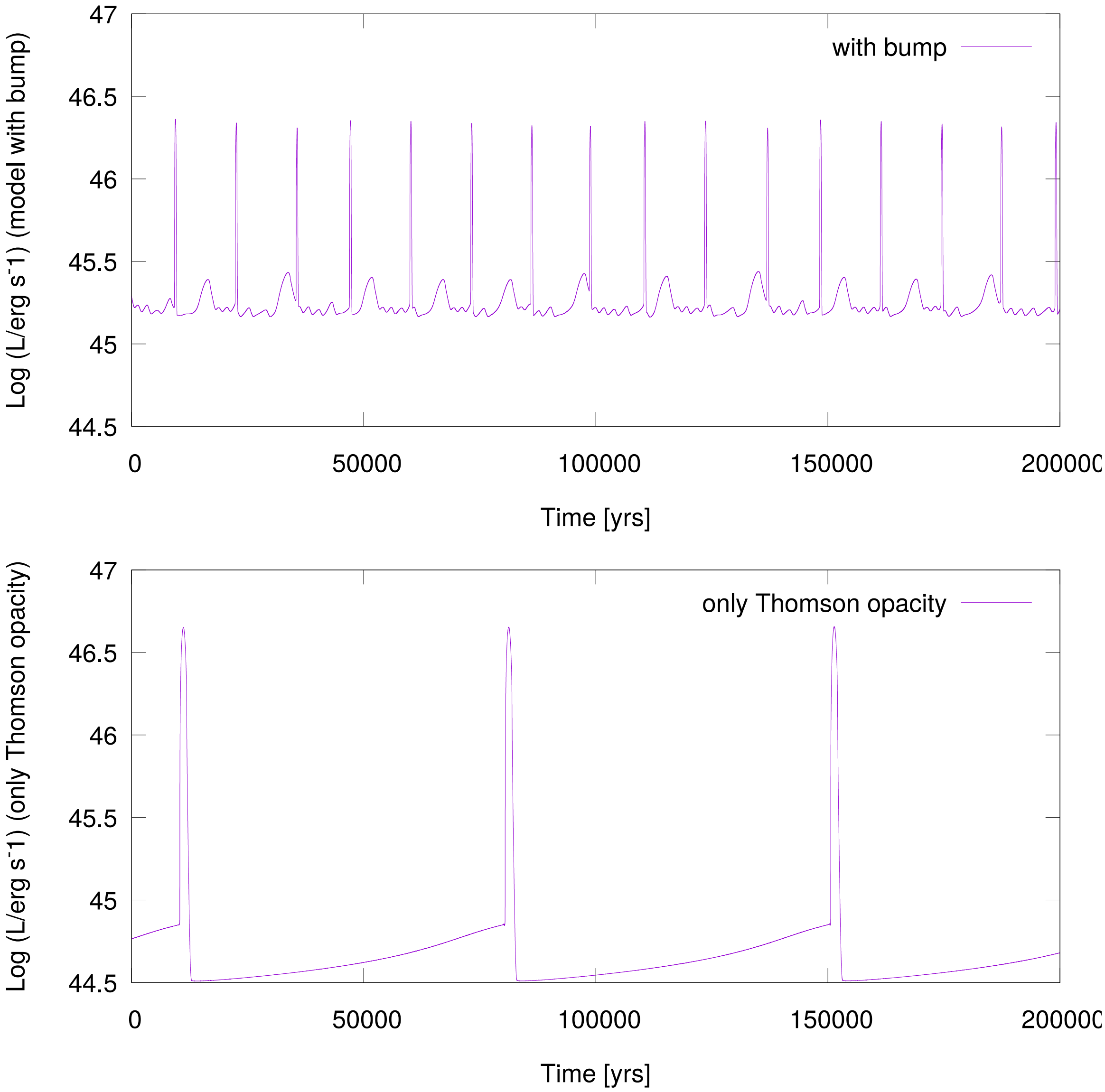

Figure 6.5: Results of the time-dependent model for $M = 5 \times 10^8 M_\odot$, $\dot{m} = 0.03$ (same as in Jiang et al. (2016)).

separation. Additionally, some mild *precursors*, being an outcome of a non-monotonic profile of the s parameter distribution, are also visible. That partial stabilization, being an important effect for the Active Galactic Nuclei, has only weak influence on the radiation pressure among all BH mass-scale in accretion disk under the assumption of Solar metallicity. In case of sources with different metallicity, this effect can change its extent. Finally, there is a conclusion that the radiation pressure driven limit cycle oscillations, suffering some disturbances from the *Iron Opacity Bump* in case of the AGN disks are also expected.

Chapter 7

Summary

Development of X-ray satellites allowed for detection of hot matter in direct black hole vicinity, forming the accretion disks in close binary systems, contributing to a proof of existence of such extremely compact objects. Improvement of the timing resolution allowed for the observations of the lightcurves of X-ray binary systems, with a good accuracy time coverage. Among all the detected variability patterns, the most regular ρ and ν states as defined for the classical prototype of high$-\dot{m}$ microquasar GRS $1915+105$ are consistent with the hypothesis of the internal, disk origin – radiation pressure instability. Advection of heat prevents the disk from breaking into rings, and along with the viscous processes regulate the thermal instability and lead to observed, regular limit-cycle oscillations. The nonlinearity of the process results in broad diversity of the variability patterns. However, the most fundamental outburst properties, like relative amplitudes and outburst shapes can be connected to the basic physical source parameters, such as Eddington ratio $\dot{m}$. This is one of the important aspects of my Thesis.

In this thesis I performed a broad study of the accretion disks radiation pressure driven oscillations. I have studied the range of effective models. Under the assumption, that origin of the viscous dissipation in the accretion disk is turbulent, and the viscosity can only depend on the total and gas pressure, the formula $\tau_{r\phi} = \alpha P^{\mu} P_{\rm rad}^{1-\mu}$ covers all the physical cases of the gas and radiation pressure dominated disks.

From the physical point of view, the accretion disk plasma is driven by the joint Maxwell and hydrodynamic equations and the most probable mechanism suppressing the thermal instability can be global, strong magnetic field. Another possible stabilizing mechanism for the accretion disk is wind outflow, possible to be confirmed by the spectral analysis, which has been shown in Chapter 3. The wind can also be driven by magnetic fields.

The numerical computations in this thesis were based on the $1.5-$ dimensional global accretion disk GLADIS code (Global Accretion Disk Instability Simulation). Although the code is based on simplified assumptions and does not account for the short-timescale dynamical phenomena like shocks or vertical/radial oscillations, it supplies sufficient possibility to study the global accretion disk behaviour in the long thermal and viscous timescales, being commonly observed by the X-ray satellites.

In this thesis (Chapter 4) I have studied the dependence between the input parameters and flare characteristics for the broad range of numerical models. For some of the observables like period and relative amplitude, the significant correlations between the input parameters like central object mass and α viscosity were found. Also the dependence between the μ stabilizing parameter and the lightcurve has been tested. Those two empirical formulae, along with the broader set of our results, allowed for the construction of the new, spectrum-independent method of the mass and accretion rate determination, based only on the lightcurve shape. The universal character of the Eddington luminosity, along with some previous studies on the possible range of the value of the α parameter, allowed for strict determination of the mass for the newly discovered source HLX-1. This object belongs to Ultraluminous X-ray sources, being the Intermediate Mass Black Hole candidate.

Applying this method, the mass of HLX-1 has been determined on the level of $1.9 \times 10^5 M_\odot$ (Chapter 5). The future development of the X-ray observing devices, like the ATHENA project will enable the broader studies of the nature of the limit-cycle oscillation of the microquasars.

Along with Chapter 3 (dedicated to example of one microquasar), and Chapter 5 (dedicated to Intermediate Mass Black Hole), Chapter 6 is dedicated to the Active Galactic Nuclei. The special effect occurring in cooler matter ($T \approx 10^5$K) is not present in the hotter microquasar accretion disks ($T \approx 10^7$K) and humble in the IMBH disks ($T \approx 10^6$K). This effect, named Iron Opacity Bump has an influence on the local thermal stability of the disk, but the global stability is governed by the interplay of the local instability and global diffusion. In effect, in contradiction to local shearing-box simulation results (Jiang et al., 2016), this effect change only the flares shape and timescales and stabilizes the disk only partially.

Acknowledgments

Special thanks to all the collaborators: **Bożena Czerny** for help with work about the atomic opacities data, **Fiamma Capitanio** and **Stefano Bianchi** from INAF, Rome, Italy, for work with the *Chandra* data, and **Qingwen Wu** with his group from Huazhong University, People Republic of China, for data about Active Galactic Nuclei and HLX-1 Intermediate-Mass Black Hole.

Bibliography

Textbooxs:

Frank, J., King,S., Raine D. *Accretion Power in Astrophysics*

Jackson, J.D., *Classical Electrodynamics*, Wiley & Sons inc., 1999

Longair, M., *High Energy Astrophysics*, Cambridge University Press, 2011

Journal papers:

LIGO Scientific Collaboration and Virgo Collaboration, Fermi Gamma-ray Burst Monitor, and INTEGRAL 2017, ApJ Letters, 848, 13

Abbott, B. P. et al.(LIGO Scientific Collaboration & Virgo Collaboration) Phys. Rev. Lett. 116, 061102 - Published 11 February 2016

Abdo, A. A. & Ackermann, M. & Arimoto, M. & Asano & et al. 2009, Science, 323, 1688

Abramowicz, M. A., Czerny, B., Lasota, J. P., Szuszkiewicz, E. et al. 1988, ApJ, 332, 646

Abramowicz, M. A., Becker, J. K., Biermann, P. L., Garzilli, A. et al. 2009, ApJ, 756, 659

Alexander, D. R., Rypma, R. L., Johnson, H. R. 1983, ApJ, 272, 773

Altamirano, D., Belloni, T., Linares, M., et al. 2011a, ApJL, 742, L17

Altamirano, D., Linares, M., van der Klis, M., et al. 2011b, The Astronomer's Telegram, 3225, 1

Altamirano, D.,& Belloni, T. 2012, ApJ, 747, L4

Bachetti, M., Harrision, F.A., Walton, D.J. Grefenstette, B.W. 2014, Nature, 514,202

Belloni, T., Klein-Wolt, M., Méndez, M., van der Klis, M., & van Paradijs, J. 2000, , 355, 271

Balbus, S.A., Hawley, J. F. 1991, ApJ, 376,214

Belloni, T., Klein-Wolt, M., Méndez, M., van der Klis, M., & van Paradijs, J. 2000, , 355, 271

Bjoernsson, G. , Abramowicz, Marek A., Chen, X., Lasota, J.-P.

Blaes, O. 2014, , 183, 221

Brandt, W. N., Mathur, S., & Elvis, M. 1997, , 285, L25

Blandford, R. D., Payne, D. G.,1982, MNRAS, 199, 893

Bondi H., 1952, MNRAS, 112, 195B

Brandt, W. N. & Mathur, S. & Elvis, M. 1997, MNRAS, 285, 25

Burm, H. 1985, A & A, 143, 389

Capitanio, F., Del Santo, M., Bozzo, E., Ferrigno, C., De Cesare, G., Paizis, A., 2012, MNRAS, 422, 3130

Capitanio F., Giroletti M., Molina M., Bazzano, A., Tarana A., Kennea J., Dean A. J., Hill A. B., Tavani M., Ubertini P., 2009, ApJ, 690, 1621

Capitanio, F., Ubertini, P., Bazzano, A., et al.2005, ApJ, 622, 503

Carr, B.J., Hawking, S.W. 1971, MNRAS, 168, 399

Corbel, S., Rodriguez, J., Tzioumis, T., Tomsick, J., 2011, Atel, 3167

Czerny, B., Nikołajuk, M., Różańska, A., et al. 2003, , 412, 317

Czerny, B., Siemiginowska, A., Janiuk, A., Nikiel-Wroczyński, B., & Stawarz, Ł. 2009, , 698, 840

Davis, S. W. & Narayan, R. & Zhu et al. 2011, ApJ, 734, 111

Del Santo, M. & Nucita, A. A. & Lodato et al. 2014, MNRAS, 444,93

Done, C. & Davis, S. W. 2008, ApJ, 683, 389

Dong, S. & Shappee, B. J. & Prieto, J. L. & Jha et al. 2016, Science, 351,257

Davis, S. W., Narayan, R., Zhu, Y., et al. 2011, , 734, 111

Del Santo, M., Nucita, A. A., Lodato, G., et al. 2014, , 444, 93

Done, C. & Davis, S. W. 2008, , 683, 389

Eichler, D. & Livio, M. & Piran, T. & Schramm, D. N. 1989, 340, 126

Elvis, M. 2000, ApJ, 545, 63

Evans, C. R. & Kochanek, C. S. 1989, , 346, L13

Everett J. E., 2005, ApJ, 631, 689

Farrell, S. A., Webb, N. A., Barret, D., Godet, O., & Rodrigues, J. M. 2009, , 460, 73

Filippenko, A. V. & Ho, L. C. 2003, , 588, L13

Foschini, L., Berton, M., Caccianiga, A., et al. 2015, , 575, A13

Gierliński, M.; Zdziarski, A. A.; Poutanen, J.; Coppi, P. S.; Ebisawa, K.; Johnson, W.W. 1994, MNRAS, 309, 496

Godet, O., Plazolles, B., Kawaguchi, T., et al. 2012, , 752, 34

Grebenev, S.A., Molkov, S.V., Sunyaev, R.A., 2005, Atel, 444

Greiner, J., Cuby, J. G., & McCaughrean, M. J. 2001, , 414, 522

Gregory, P. C., Taylor A. R. et al. 1979, The Astronomical Journal,84,7

Grindlay, J., Tang, S., Los, E. & Servillat, M. 2012, New Horizons in Time Domain Astronomy, Proceedings of the International Astronomical Union, 285, 29

Hawley, John F.; Gammie, Charles F.; Balbus, Steven A., 1995, ApJ, 440, 742G

Hawking,S. 1971, MNRAS, 152, 75

Hirose, S., Krolik, J. H., & Stone, J. M. 2006, , 640, 901

Honma, F., Kato, S., & Matsumoto, R. 1991, , 43, 147 in 't Zand, J. J. M., Heise, J., Lowes, P., & Ubertini, P. 2003, ATel, 160

Iyer, N., Nandi, A., & Mandal, S. 2015, , 807, 108

Janiuk, A. & Czerny, B. 2005, , 356, 205

Janiuk, A. & Czerny, B. 2011, , 414, 2186

Janiuk, A., Grzędzielski, M., Capitanio, F., & Bianchi, S. 2015, , 574, A92

Janiuk, A. & Misra, R. 2012, , 540, A114

Janiuk, A., Czerny, B., Siemiginowska, A. 2002, , 576, 908

Jiang, Y.-F., Stone, J. M., & Davis, S. W. 2013, , 778, 65

Jiang, Y.-F., Davis, S. W., Stone, J. M. 2016, ApJ, 827, 10

Kelly, B. C., Bechtold, J., & Siemiginowska, A. 2009, , 698, 895

King, A. R., Pringle, J. E., West, R. G., Livio, M. 2004, MNRAS, 348, 111

King A. L. et al., 2012, ApJ, 746, 20

King, A., Lasota, J.-P. 2014, MNRAS, 444, 30

King, A., Lasota, J.-P. 2014, MNRAS, 458, 10

Kilitzan, B., Baumgardt, H., Loeb, A. 2017, *Nature* 542,203

Kozłowski, S. 2016, , 826, 118

Krauss, M.I., Kilgard, R.E, Garcia, M.R., Roberts, T.P., A. H. Prestwich, A. H., 2005, , 630, 1

Kunert-Bajraszewska, M., Janiuk, A., Gawroński, M. P., Siemiginowska, A. 2010, ApJ, 718, 1345

Kunert-Bajraszewska, M. & Janiuk, A. 2011, , 736, 125

Kuulkers, E., Lutovinov, A., Parmar, A., et al. 2003, The Astronomer's Telegram, 149, 1

Lasota, J.-P., Abramowicz, M. A., Chen, X., et al. 1996, , 462, 142

Lasota, J.-P., Alexander, T., Dubus, G., et al. 2011, , 735, 89

Lesur G., Ferreira J., Ogilvie G.I., A & A, 550, A61

Lightman, A. P. & Eardley, D. M. 1974, , 187, L1

Lutovinov, A., Revnivtsev, M., Molkov, S., & Sunyaev, R. 2005, A&A, 430, 997

Lutovinov, A. A., & Revnivtsev, M. G. 2003, Astron. Lett., 29, 719

Lyubarskii, Y. E. 1997, MNRAS, 292, 679

Maccarone, T. J., Gallo, E., & Fender, R. 2003, , 345, L19

McHardy, I. M., Koerding, E., Knigge, C., Uttley, P., & Fender, R. P. 2006, , 444, 730

Merloni, A. & Nayakshin, S. 2006, , 372, 728

Meyer, F. & Meyer-Hofmeister, E. 1981, A & A, 104, 10

Meyer, F. & Meyer-Hofmeister, E. 1982, A & A, 106, 34

Miller, J.M, Raymond, J., Fabian, A., Reynolds, C., Steeghs, D., Homan, J., van der Klis, M., Wijnands, R. 2006, American Astronomical Society, HEAD meeting # 9, id.8.02; Bulletin of the American Astronomical Society, Vol. 38, p.361

Merloni, A. & Nayakshin, S. 2006, MNRAS, 372, 728M

Mishra, B. & Fragile, P. C. & Johnson, L. C. et al. 2016,ArXiv e-prints, 1603.04082

Miller J.M M., Raymond J., Fabian A., Steeghs, D., Homan J., Reynolds C., van der Klis, M., Wijnands, R. 2006, Nature, Volume 441, Issue 7096, pp. 953-955

Mishra, B., Fragile, P. C., Johnson, L. C., & Kluźniak, W. 2016, ArXiv e-prints

Muchotrzeb.,B. , Paczynski, B. 1982, Acta Astronomica, vol. 32, no. 1-2, p. 1-11.

Nayakshin, S., Rappaport, S., & Melia, F. 2000, , 535, 798

Neilsen, J., Remillard, R. A., & Lee, J. C. 2011, , 737, 69

Netzer, H. 2006, ApJ, 652,117

Paczyński, B. 1971, ARAA, 9, 183

Paczyński, B. 1998, ApJ, 494, 45

Paczyński, B.; Wiita, P. J. 1980, , A & A, 88, 23

Paczynski, B.; Bisnovatyi-Kogan, G. 1981, Acta Astronomica, 31,283

Page, D.N. 1976, Phys. Rev. D, 13, 198

Pandey, M., Rao, A. P., Manchanda, R., Durouchoux, P., Ishwara-Chandra, C. H., 2006, A&A, 446, 471

Pahari M., Yadav J. S., Bhattacharyya S., 2014, ApJ, 783, 141

Peterson, B. M., McHardy, I. M., Wilkes, B. J., et al. 2000, , 542, 161

Pringle, J. E., Rees, M. J., Pacholczyk, A. G. 1973, , 29, 179

Proga D., 200, ASP, 373,267

Różańska, A., Czerny, B., Życki, P. T., Pojmański, G. 1999, , 305, 491

Rebusco, P. & Moskalik, P. et al. 2012, A & A, 540, 4

Ricci, C. & Bauer, F. E. & Arevalo et al. 2016, ApJ, 820, 5

Rao, A. & Vadawale, S. V. 2012, ApJl, 757, 12

Ross, J., Latter, H., Tehranchi, M. 2017, arXiV e-prints, 1703.00211

Revnivtsev, M. & Gilfanov, M. & Churazov, E. et al. 2003, The Astronomer's Telegram, 150, 1

Ricci, C., Bauer, F. E., Arevalo, P., et al. 2016, , 820, 5

Rodriguez, J,Corbel, S., Caballero, I., Tomsick, J. A., Tzioumis,T., Paizis, A., Cadolle Bel, M., Kuulkers, E., 2011, A&A, 533, L4

Rodriguez,J., Corbel, S., Tomsick, J.A., Paizis, A., Kuulkers, E. Astron. Telegram, 3168

Ross, J., Latter, H., Tehranchi, M. 2017, arXiV e-prints, 1703.00211

Różańska, A., Czerny, B., Życki et al. 1999, MNRAS, 305, 491

Rupen M. P., Mioduszewski A. J., Dhawan V., 2003, Atel 150.

Sakimoto, P. J. & Coroniti, F. V. 1981, , 247, 19

Sakimoto, P. J. & Coroniti, F. V. 1989, , 342, 49

Sams, B. J., Eckart, A., Sunyaev, R. et al. 1996, Nature, vol. 382, issue 6586, pp.47-49

Sądowski, A. 2016, MNRAS, 459, 4397

Seaton, M. J., Yan, Y., Mihalas, D. et al. 1994, MNRAS, 266, 805

Servillat, M., Farrell, S. A., Lin et al. 2011, ApJ, 743, 6

Servillat, M., Farrell, S. A., Lin, D., et al. 2011, , 743, 6

Shakura, N. I. & Sunyaev, R. A. 1973, , 24, 337

Shakura, N. I., Sunyaev, R. A 1976, , 175, 613

Shaposhnikov, N., 2001, ATel, 3179

Siemiginowska, A. & Czerny, B. 1989, in NATO Advanced Science Institutes (ASI) Series C, Vol. 290, NATO Advanced Science Institutes (ASI) Series C, ed. F. Meyer, 29

Soria, R., Hau, G. K. T., & Pakull, M. W. 2013, , 768, L22

Starling, R. L. C., Siemiginowska, A., Uttley, P., & Soria, R. 2004, , 347, 67

Steeghs, D., McClintock, J. E., Parsons, S. G., et al. 2013, , 768, 185

Straub, O., Godet, O., Webb, N., Servillat, M., & Barret, D. 2014, , 569, A116

Suková, P., Grzędzielski, M., & Janiuk, A. 2016, , 586, A143

Sukova, P. & Janiuk, A. 2015, MNRAS, 474,1565

Sutton, A. D. & Roberts, T. P. & Walton et al. 2012, MNRAS,423, 1154

Sutton, A. D. & Swartz, D. A. & Roberts 2017, ApJ, 836, 48

Svensson, R. & Zdziarski, A. A. 1994, , 436, 599

Szuszkiewicz, E. 1990, , 244, 377

Taam, R. E., Chen, X., & Swank, J. H. 1997, , 485, L83

Taam, R. E. & Lin, D. N. C. 1984, , 287, 761

Torres, M.A.P., Jonker, P.G., Steeghs, D., Mulchaey, J. S., 2011, Atel, 3150

Yu, W. & Yan, Z. 2009, ApJ, 701, 1940

van der Helm, E., Portegies Z., S., Pols, O. 2016, MNRAS, 455, 462

Watarai, K.-y. & Mineshige, S. 2003, , 596, 421

Wiersema, K., Farrell, S. A., Webb, N. A., et al. 2010, , 721, L102

Wijnands, R.; Yang, Y. J.; Altamirano, D., 2012, MNRAS, 422,91

Wu, Q. 2009, , 398, 1905

Wu, Q., Czerny, B., Grzędzielski, M., et al. 2016, , 833, 79

Xie, Z. H., Ma, L., Zhang, X., et al. 2009, , 707, 866

Yan, Z., Zhang, W., Soria, R., Altamirano, D., 2015, ApJ, 811, 23

Zdziarski, A. A. & Mikołajewska, J. & Belczyński, K. 2013, MNRAS, 429, 104

Svensson, R. & Zdziarski, A. A. 1994, ApJ, 436, 599